Synthesis and Application of Lignin-Based Carbon Materials with Tunable Structure from the Mesoscale to Nanoscale

A Dissertation Presented for the

Doctor of Philosophy

Degree

The University of Tennessee, Knoxville

Lu Yu

May 2022

To my beloved parents, for their endless love and support.

ACKNOWLEDGEMENTS

I would like to express my sincere thanks to my advisor, Dr. David Harper and my coadvisor, Dr. David Keffer, for their continuous support, help and encouragement. Without their patient guidance, this dissertation would not be possible. The attitude toward research, which I learned from them, has been of great value to me up to now and in the future. Dr. Harper, thank you for teaching me experimental techniques and facilitating my growth as a researcher. I appreciate that you always support and encourage me to follow my research interests. You made me realize the importance of enthusiasm and curiosity in research. Dr. Keffer, thank you for teaching me coding and giving me guidance for conducting simulations. I appreciate that you are always extremely helpful and have given me valuable suggestions through-out my research.

I would like to extend my thanks to my collaborators, Dr. Chien-Te Hsieh and Dr. Ilia Ivanov, for training me to conduct experiments and answering my many questions. Their patient guidance and help greatly facilitated the progress of my research projects. I would also like to express my appreciation to my committee members, Dr. Haixuan Xu and Dr. Orlando Rios, for their valuable suggestions.

I would also like to thank my group members, Kendhl Seabright, Dayton Kizzire and Valerie García-Negrón for their support and for the great times we spent together. I also would like to extend my thanks to Jakob Scroggins, for his great assistance.

I am grateful to all my collaborators and professors for their instruction and support.

I would like to express my deepest gratefulness to my parents and my family. Their selfless and endless love and understanding support me to complete this dissertation. I want to thank my best friends, Su Qin, Luna Liang, Yutong Xiang, Xiaoyi Li for the enduring encouragement and heartwarming comfort whenever I felt frustrated.

My special thanks go out to the United States Department of Energy, USDA National Institute of Food and Agriculture, and Center for Materials Processing, at Tennessee Higher Education Commission (THEC) which supported this work.

ABSTRACT

As the most abundant aromatic polymer in nature, lignin has great potential to be developed for high-value products due to its high carbon content and unique aromatic structure. This work elucidates the process-structure-property-performance relationships between lignin and the resulting high-value carbon materials and explores their potential to be used for energy storage and environmental applications. Physical activation was conducted for developing activated carbons (ACs) from various lignin precursors and applied as electrodes for supercapacitors. The results showed that softwood lignin-derived ACs achieved high surface area and excellent electrochemical performance. To further improve the electrochemical performance of developed ACs, carbon quantum dots (CQDs) were introduced and decorated on the surface of ACs. Benefiting from the hydrophilicity and ultrafine size of CQDs, the addition of CQDs leads to the enhanced effective surface area and decreased ionic diffusion path, thus significantly improved the affinity of the electrodes toward aqueous electrolytes. To further increase the surface area and optimize the porous structure of ACs, traditional two-step and updated one-step chemical activation were conducted. This work investigated the effect of one- and two-step KOH activation on the surface properties of lignin-based ACs. One-step activation produced ACs achieved ultrahigh surface area and high mesopore ratio, leading to the ultrahigh capacitance and energy density of the fabricated supercapacitors (SCs). In comparison, two-step activation produced ACs with limited surface area but high oxygen contents, leading to a hydrophilic surface. The hydrophilicity of ACs greatly decreases the internal resistance and benefits the capacitance even at high current density, thus achieving high power density of the fabricated SCs. Additionally, lignin-derived ACs also exhibit excellent adsorption performance for water purification, with the maximum adsorption capacity of 1,250 mg g^{-1} of methylene blue (MB) adsorption. To improve the regeneration efficiency, magnetic ACs were synthesized via an efficient co-carbonization and activation method. The magnetite nanoparticles on the ACs surface significantly improve its recycling ability. In addition to ACs, the optimized synthesis method was proposed to produce lignin-derived

carbon quantum dots (CQDs) with multicolor emissions from deep blue to red with narrow fluorescence spectra.

TABLE OF CONTENTS

LIST OF TABLES

LIST OF FIGURES

Chapter 1 Introduction

Background of biomass lignin

Lignin is a class of polyaromatic compounds that comprises approximately 25% of lignocellulosic biomass plant cell wall. It is the second most abundant natural polymer in the world and currently about millions of tons are produced as a coproduct of pulp and paper production annually.[1-3] As a highly branched heterogeneous polymer built up with phenylpropane units, lignin has high carbon content (> 60 wt.%), which makes it an excellent fuel for pulp production.[1, 3, 4] However, not all of the lignin co-product of the pulping process is used and regarded as a waste product with relatively low value. Due to its complex and irregular structure and contamination from sugars and processing chemicals, lignin is hard to be effectively isolated and converted into commercial use. [1] Approximately 98% of the available lignin is burned for power generation, which has monetary value, and the remaining (< 2%) is used for developing specialty products for various market segments.[2, 5] Numerous attempts have been made to valorize lignin.[1] The aromatic structure has been applied to high value products, including carbonaceous materials, surfactants, foams, and adhesives, have been synthesized with little market penetration.[4, 6]

Lignin is recognized as a random combination of three basic monomer types: p-coumaryl alcohol (H), coniferyl alcohol (G), and sinapyl alcohol (S) (shown in Figure 1.1). The aliphatic side chain is usually attached at C-1 with the carbons on side chain.[1] The phenol oxygen is usually located at C-4 and sometimes there is methoxyl group located at C-3. The carbon groups at C-5 is usually referred to as “condensed” structures in both native, referring to lignin in plant cell wall prior to pulping, and C-5 linkages formed during lignin extraction.[1] All these constituents together form a three dimensional network structure composed of phenylpropane units connected with ether and C–C bonds. The composition of lignin highly depends on its raw material sources and isolation process.[7] These can be classified into three broad classes, softwood, hardwood, and herbaceous (grass) lignin,

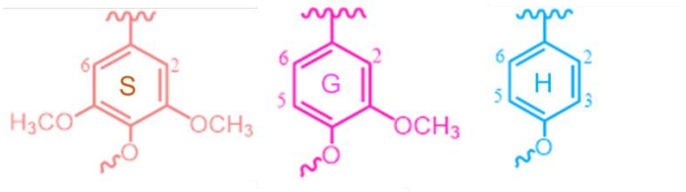

Figure 1.1 Lignin monomeric units.

based on their composition in structural units.[8, 9] Softwood has higher lignin content (~28%) compared with hardwood (~20%) and grass(~15%).[1, 3] The principle monomer for softwood lignin is G, and lignin subtracted from hardwood usually have more S and G monomers, while H monomer is more prominent in grasses.[1] Nowadays the most prevalent and commercial-scale used chemical pulping process is the kraft process, which uses sodium hydroxide as the main reagent combined with sodium sulfide as a nucleophile catalyst for lignin degradation and separation from cellulose.[1] Kraft process has many advantages including low energy requirements, favorable economics, excellent chemical recyclability, coproduct generation, can pulp virtually any lignocellulosic feedstocks, high pulp strength, but low pulp yields (~45-55%) compared to some other methods. In this work, we also adopt lignin isolated by a biomass-derived renewable γ-valerolactone (GVL) solvent for comparison. The key feature for this process is the high-efficiency, high-yield fractionation of biomass into different components, and ability to pulp a wide range of biomass feedstocks. The lignin-derived by GVL method has high purity with minimal ash and sugar content, which makes it an excellent candidate for high-quality carbon materials.[10]

Activated carbons for energy storage

Synthesis of activated carbons

Activated carbons (ACs) are high-porosity materials, which could also be regarded as assemblies of defective graphene layers that come from organic parent materials after carbonization and physical/chemical activation process.[11] A solid-phase carbonization always proceeds within solid state with the removal of atoms and replacement within a solid lattice, without bulk materials movement.[11] To this degree, the structure of parent materials tightly related to the structure of the carbonized char. Usually the carbonization is carried out in an inert atmosphere (700 – 1000℃), and the structures of the produced char can be considered as the combination of nano-graphene sheets with different size, direction, the existence of heteroatoms, linear carbons, holes, and dangling bonds in virtually infinite physicochemical possibilities.[12] The random bonding together of these

short-range non-planar units creates imperfect packing(space), called porosity. Disorder of the parent substances is the central to produce porosity, upon which the properties of activated carbons rely.[11] Different parent materials decompose in their own ways and lead to the their distinctive pore characteristics.[12] However, as the carbonization temperature increases, the pore space extends to a maximum. When heat treating temperature (HTT) increases to above 800℃, carbon cross-link reactions reduce the space between atoms and reduces porosity.[12] Thus, we observed a decrease in surface area as the carbonization temperature increases from 700 to 1000℃ for our kraft lignin (KSW) (Figure 1.2). As we observed, high surface area ACs are not produced in during pyrolysis, and generally either physical or chemical activation is needed for creating pore structure.[13, 14]

Activated carbons for supercapacitors

Activated carbons (ACs) are widely applied to a variety of industry applications, including the catalyst support, water purification, separation, and energy storage devices.[15] Of particular interest, the applications of ACs as electrodes for supercapacitors have attracted enormous attentions due to its high surface area, stability, and low cost. Typically, supercapacitors are classified as electric double layer (EDL) capacitors and pseudo capacitors. For ACs, EDL capacitor is the main way to create capacity, as the excessive surface area of ACs enabled the double-layer formation and subsequent high power density.[16] The performance of supercapacitors using activated carbon as electrode materials strongly depends on pore structure, pore size distribution, surface area, and surface functional groups,[17, 18] thus requiring an in-depth investigation. An efficient activation method is needed for preparing activated carbons with enhanced surface properties from lignin precursors.

Synthesis and applications of carbon quantum dots

Carbon quantum dots (CQDs), also known as carbon quantum dots (CQDs) are a subset of nanoparticles with the characteristic size of <10 nm and have a carbon core surface-passivated with various functional groups.[19-21] CQDs have attracted abundant attention during the past decade due to their unique properties, such as tunable luminescence, easy

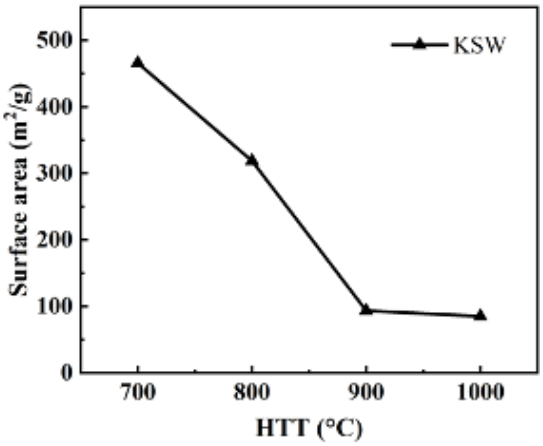

Figure 1.2 The variation of surface area with HTT for carbonization of KSW lignin.

fabrication, low cost and low toxicity.[22-25] As a result, they haves been applied in various fields, including bioimaging, LED devices, biosensors, waste absorption, biomedicine and so on.[26-28] Usually the property of the CQDs is highly dependent on the material sources, synthesis approaches and conditions. The diversity of CQDs results from the variety of carbon precursors and synthetic methods, and generally, they are mainly classified into graphene quantum dots (GQDs), carbon nanodots (CNDs), and polymer dots (PDs).[21, 29] GQDs are mainly constituted by one-layer graphene debris or graphitic nanocrystal structure as carbon core. CNDs mainly possess the sp^2-hybridized nanocrystalline embedded into amorphous carbon. PDs are aggregated polymer nano-particles derived from polymer or monomers.[21, 30] The synthesis approaches have been divided into top-down and bottom-up two main categories. Top-down synthesis involves breaking the larger structures into smaller nano-carbon particles under harsh conditions, and electrochemical etching, chemical oxidation and laser ablation are commonly used methods. On the contrary, bottom-up synthesis adopts a hydrothermal method, microwave assistance, or ultrasonic treatment to build CQDs from small molecules or polymer precursors.[19, 21] So far, although many have explored the potentials of CQDs, it is still challenging to elucidating the key factors controlling their varied physicochemical properties.[19] Normally, controlling size and, crystallinity, along with surface modification and heteroatom doping, are widely used methods to tune luminescence of CQDs.[21]

Research objectives

The overall objective of my research is to maximize the value of lignin and explore the potential of lignin as a feedstock for high-value carbon materials. With the goal of developing a reproducible and efficient approach to produce carbon quantum dots and renewable carbons with targeted structure and properties, which can be used as electrodes in high performance devices, such as supercapacitors and batteries, we investigate the processing-structure-property-performance relationship for lignin-based carbon products. This proposal research mainly conducted in three: Optimization and tailored porous

carbons for high performance supercapacitors, magnetic activated carbons for cationic dyes adsorption, and lignin-derived carbon quantum dots with multiple color emissions.

In chapter 2, I focus on comparing ACs produced by GVL lignin with different precursors (yellow pine and switchgrass) and applied as electrodes in supercapacitors. The objective of this work is to explore and optimize the performance of GVL lignin-derived ACs in supercapacitors. With the composition difference of the precursors, the softwood lignin produced ACs achieved higher surface areas and led to higher capacitance of fabricated SCs.

In chapter 3, I adopted the commercial scaled kraft softwood (KSW) lignin as precursor for producing ACs. To further improve the electrochemical performance, CQDs were introduced and decorated on the surface of ACs as electrodes for high performance supercapacitors. The objective of this work is to optimize the performance of KSW lignin-derived ACs as the electrodes in supercapacitors. Benefiting from the hydrophilicity and ultrafine size of CQDs, the effective surface area is greatly enhanced and leading to the decreased ionic diffusion path.

In chapter 4, I conducted chemical activation to further increase the surface areas and optimize the porous structures of ACs. The effects of one- and two- step activation method on the surface properties of ACs were investigated. With the updated one-step method, ACs with ultrahigh surface area and high mesopore ratio are produced. In comparison, two-step produced ACs achieved limited surface area but with abundant oxygen surface functionalities.

In chapter 5, I applied lignin-derived ACs for MB adsorption. To improve the regeneration efficiency, I developed a simple route to synthesize magnetic ACs with magnetic iron oxides nanoparticles uniformly distributed on the surface. These magnetite nanoparticles

on ACs enhanced the adsorption capacity and significantly improved the regeneration efficiency.

In chapter 6, I describe the efforts to synthesize carbon quantum dots with multiple color emissions from lignin feedstocks by hydrothermal method. With the target to synthesize multicolor CQDs, several steps are identified to explore the effectiveness of the chemicals to depolymerize and functionalize lignin, and thus control the size of CQDs as well as surface state.

Chapter 2 Performance and Economic Analysis of Organosolv Softwood and Herbaceous Lignins to Activated Carbons as Electrode Materials in Supercapacitors

A version of this chapter was originally published by Yu, Lu; Seabright, Kendhl; Bajaj, Ishan; Keffer, David J; Alonso, David M; Hsieh, Chien-Te; Li, Mi; Chen, Hao; Dai, Sheng; Gandomi, Yasser Ashraf; Maravelias, Christos T; Harper, David P.:

Yu, Lu; Seabright, Kendhl; Bajaj, Ishan; Keffer, David J; Alonso, David M; Hsieh, Chien-Te; Li, Mi; Chen, Hao; Dai, Sheng; Gandomi, Yasser Ashraf; Maravelias, Christos T; Harper, David P., 2022. Performance and Economic Analysis of Organosolv Softwood and Herbaceous Lignins to Activated Carbons as Electrode Materials in Supercapacitors. Frontiers in energy research, 10.

Credit authorship contribution statement:
Conceptualization, LY, C-TH, DA, IB, DH; methodology, LY, KS, IB, C-TH, ML, SD, YG, CM, DH; validation, LY, KS, IB, ML, HC.; formal analysis, LY, IB, C-TH, ML; resources, DK, SD, CM, DH; data curation, KS, DH.; writing—original draft preparation, LY, IB; writing—review and editing, KS, DK, DA, C-TH, ML, HC, SD, YG, DH; visualization, LY, IB; supervision, DH, DK, SD, CM; project administration, DH; funding acquisition, DH, DA, CM, SD.

Abstract

In this work, yellow pine (YP, softwood) and switchgrass (SG, grass) lignins were extracted as a coproduct of an organosolv γ-valerolactone (GVL) biorefinery that also produces biofuels and furfural. The extracted lignins were converted to carbon precursors for synthesizing porous activated carbon electrodes for high energy-density supercapacitors. This research details the impact of lignin composition on the derived porous structures and electrochemical properties of activated carbons. Lignin precursors with various syringyl (S) to guaiacyl (G) contents were characterized using ^{31}P nuclear magnetic resonance (NMR) and two-dimensional $^{1}H–^{13}C$ NMR. A two-step activation process, using steam and carbon dioxide as the activating agents, enabled the formation of porous carbons structures with high surface area. The capacitive behavior of

supercapacitors was systematically characterized by cyclic voltammetry, charge-discharge cycling, and electrochemical impedance spectroscopy. The specific capacitance of YP and SG capacitors reached 367 and 221 F g^{-1}, respectively. Both types of capacitors demonstrated remarkably stable capacitance (capacitance retention >90%) along with excellent Coulombic efficiency (>99%) over 10,000 cycles. Compared to SG electrode, the better electrochemical performance achieved with YP electrodes was mainly due to shorter diffusion path, improved ionic mobility, and increased active surface area. The inexpensive lignin-based porous electrodes synthesized in this work can be used for various electrochemical devices for improved performance, decreased cost, and enhanced durability. This work also demonstrates that the selection of feedstock and appropriate processing conditions can tailor the structure of carbon composites for targeted applications. Techno-economic analysis indicates that YP and SG activated carbons can be produced at a minimum selling price of $8,493 and $6,670 per ton, respectively, which is competitive with the commercially available supercapacitor-grade activated carbons.

Introduction

Lignin is a natural aromatic polymer composed of phenylpropane units with various interunit linkages, such as ether and C–C bonds.[4, 31, 32] As one of the major components of terrestrial plants, about 70 million tons of lignin are produced as the by-product from pulp/paper industry annually.[5, 33] However, *ca.* 95% of the available lignin is combusted to generate a low-grade heat source and the remaining amount is used for preparing specialty products for various markets.[5, 33] Considering lignin's high carbon content and unique aromatic structure, it is desirable to use lignin for synthesizing high value-added products, such as carbon fiber, carbon black, dyes, and paints.[3] Manufacturing porous carbon structures from lignin precursors is another promising application given the important role of porous carbon electrodes for different electrochemical devices. Activated carbons (ACs) can be prepared using a variety of raw materials including peanut shell, sugarcane bagasse and corn syrup (see Table 2.1).[13, 34] Lignin can be considered a potential precursor in preparing highly porous ACs due to its high carbon content, low cost, and large-scale

Table 2.1 Supercapacitor performance of activated carbons produced by various biomass materials.

Precursors	Activation method	Surface area ($m^2 g^{-1}$)	Electrolyte	Specific capacitance	References
Coffee endocarp	CO_2	709	1 M H_2SO_4	176 F g^{-1} at 10 mA	[35]
Corn husk	KOH	771	0.5 M H_2SO_4	314.83 F g^{-1} at 1 mV s^{-1}	[36]
Corn syrup	Physical self-activation	1473	6 M KOH	168 F g^{-1} at 0.2 A g^{-1}	[37]
Peanut shell	$ZnCl_2$	1565	6 M KOH	245 F g^{-1} at 0.05 A g^{-1}	[38]
Kraft lignin	KOH	1148	6 M KOH	91.7 F g^{-1} at 2 mV s^{-1}	[39]
Kraft lignin	steam & CO_2	591.7	2 M H_2SO_4	125.8 F g^{-1} at 0.15A g^{-1}	[40]
Sugarcane bagasse	K_2CO_3	725	2 M KOH	265 F g^{-1} at 0.2 A g^{-1}	[41]
GVL Lignin	steam & CO_2	1070	1 M H_2SO_4	367 at 0.1 mA cm^{-2}	This work

availability as a major byproduct of paper and biofuel production.[42]

Selecting an appropriate lignin precursor is challenging due to lignin's highly complex structure that varies as a function of the biomass source and isolation methods adopted.[7] The basic constituent of lignin is phenylpropane (C6−C3), which tends to form a three-dimensional complex structure through ether or C−C bonds.[6] Lignin is composed of varying ratios of three aromatic monomers depending mainly on botanical origin, including *p*-coumaryl alcohol, coniferyl alcohol, and sinapyl alcohol.[43, 44]According to the composition of the structural units, lignin can be classified into three broad classes: softwood, hardwood, and grass lignin.[8, 9] Normally, softwood lignin predominantly contains coniferyl alcohols (~90%) with a minor amount of *p*-coumaryl alcohols.[4] Hardwood lignin possess similar amounts of coniferyl and sinapyl alcohol units, while grass lignin is composed of all three major units with high ratio of coniferyl and sinapyl alcohols.[45] Softwood lignin has a more crosslinked network structure due to the availability of the C_5 position of the coniferyl alcohol units for coupling. Hardwood and grass lignin have a more linear structure as a result of the sinapyl alcohol units that contain extra methoxy groups on the aromatic rings, which limit the formation of coupling and cross-linking branches.[33, 45]

For industrial-scale manufacturing of ACs, a consistent feedstock supply is essential to ensure relatively uniform product quality. High surface area ACs are commonly used for catalysis, purification, decolorization, deodorization, separation, and energy storage.[15, 46] The application of activated porous carbon electrodes within electric double-layer capacitors (so-called "supercapacitors") has received a surge in attention as high surface areas (i.e., electrolyte/electrode interface) enabled through activated porous electrodes for double-layer formation and subsequent energy storage.[47, 48] Many physical and chemical approaches have been reported for preparing activated carbon structures, which vary in electrode performance based upon pore size distribution, surface functional groups, and surface heterogeneity.[17, 18] However, there is limited understanding of the chemical and

physical process to convert lignin from different precursors into ACs. Herein, we establish processing-structure-property-performance relationships (PSPP) through an efficient activation method for preparing activated carbons from different lignin precursors with enhanced electrochemical properties (e.g., surface accessibility).

In this work, a novel activation technique was developed for preparing activated carbons from two types of lignin, yellow pine (YP, softwood lignin) and switchgrass (SG, grass lignin). The influence of lignin molecular structure on both surface texture and pore size distribution of the activated carbons was systematically examined. The electrochemical performance of supercapacitors assembled with carbon electrodes was also explored using cyclic voltammetry (CV), charge-discharge cycling, and electrochemical impedance spectroscopy (EIS) in aqueous electrolytes. Techno-economic analysis was performed to assess the economic viability of the process and demonstrate the efficacy of using lignin with different chemical constituents as precursors for preparing highly porous activated carbons used as electrode material in supercapacitors.

Experimental section

Preparation of activated carbons from lignin

Two kinds of YP and SG lignin were carbonized in a ceramic boat inserted in an alumina tube furnace with nitrogen gas flowing (3 L min^{-1}) at 1000 °C for 1 h. After naturally cooling down with N_2 flow, the carbonized samples were pulverized by ball-milling (PM100 RETSCH model), using 2- and 10-mm stainless steel balls in a stainless-steel container at 350 rpm for 30 min. The grounded carbon powders were separated from the grinding balls using sieves and then placed into the tube furnace for steam activation at 800 °C for 1 h with a ramping rate of 10 °C min^{-1}. After steam activation, the carbon sample was placed in the furnace under CO_2 atmosphere for physical activation at 800 °C for 1 h to yield the final samples. Figure 2.1 illustrates the schematic diagram for the experimental design for the supercapacitor using two kinds of electrode materials (i.e., YP and SG), where activated carbons (YP-AC and SG-AC) were derived from different raw materials

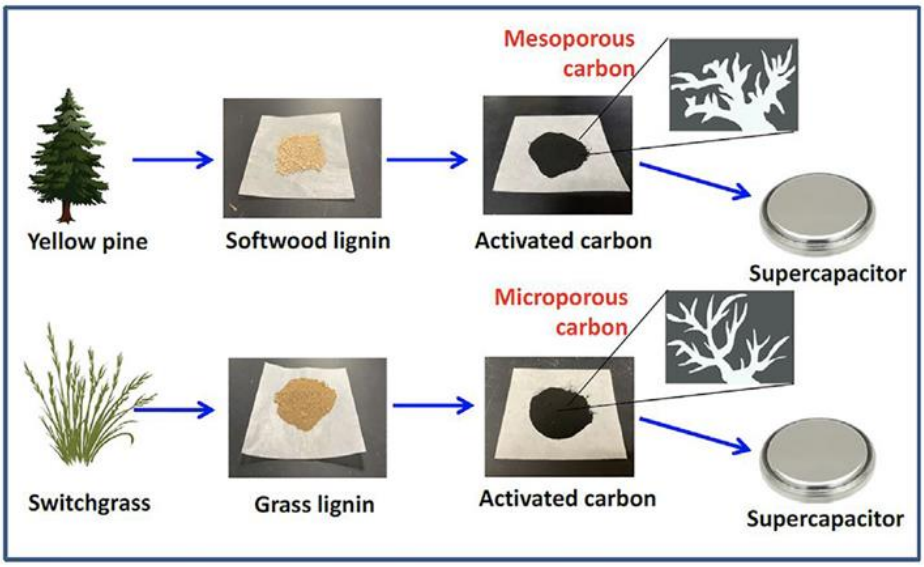

Figure 2.1 Schematic diagram for illustrating the flowchart of supercapacitor using two kinds of electrode materials, where activated carbons were derived from different raw materials and lignin precursors.

and lignin precursors.

Materials characterization

Thermogravimetric analyzer (TGA, Perkin Elmer Pyris 1) and differential scanning calorimetry (DSC, Perkin Elmer Diamond DSC) were adopted to measure thermal stability of lignin precursors in an inert nitrogen environment. The TGA analysis was conducted by heating lignin samples from 100 to 800 °C at a heating rate of 10 °C min^{-1}. The DSC procedure involved three heating and cooling cycles performed at a rate of 100 °C min^{-1}. The lignin samples were initially heated for two cycles from 25 to 160 °C, and then heated to 230 °C.

The structural morphology images of the carbon samples were collected by using scanning electron microscope (SEM, Phenom ProX). Surface characteristics of the carbon samples were analyzed by an automated adsorption apparatus (Micromeritics Instrument Co., TriStar 3000) using N_2 physisorption at -196°C. Total and mesopore surface areas of the carbon samples were calculated by using Brunauer-Emmett-Teller (BET) and Barrett-Joyner-Halenda (BJH) equations. Pore-size distributions were analyzed from the N_2-adsorption branch using density functional theory (DFT) method.

Surface functional groups on the activated carbon samples were characterized by attenuated total reflectance Fourier transform infrared (FTIR) spectroscopy (Perkin Elmer, Spectrum II). FTIR spectra were collected from 4000 – 600 cm^{-1} using 16 scans with a resolution of 4 cm^{-1}. Additional surface chemical composition was collected by X-ray photoelectron spectroscopy (XPS, Fison VG ESCA210). Elemental (i.e., CHN) analysis of lignin samples was performed by combustion analysis (Perkin Elmer) to determine amounts of carbon, hydrogen, and nitrogen. To quantify the amount of oxygen, a differential technique was adopted where the samples were assumed to be composed of solely C, H, N, and O elements. Gel permeation chromatography (GPC) was used to determine the number average molecular weight (Mn), weight average molecular weight

(Mw), and molar-mass dispersity ($Đ_M$) index of the lignin samples. GPC analysis was conducted by dissolving lignin in tetrahydrofuran (THF) at 1 mg mL^{-1} and injecting into an EcoSec GPC Instrument (Tosoh), with two columns (TSKgel SuperMultipore HZ-M, 4.6 x 150 mm, 4 µm) and a guard column held at 40 °C. Acetobromination of the lignin was required prior to dissolution in THF for GPC analysis.[49]

^{31}P-NMR measurements were carried out using a Varian 400-MR spectrometer. Lignin samples, approximately 60 mg, were dissolved in 0.4 mL NMR solvent (deuterated chloroform and pyridine (1:1.6 v/v)). Then, 0.1 mL internal standard solution (21.5 mg endo-N-hydroxy-5-norbornene-2,3-dicarboximide in 1 mL NMR solvent) and 0.05 mL relaxation reagent (11.4 mg chromium (III) acetylacetonate in 1 mL NMR solvent) were added. Immediately before NMR analysis, 0.1 mL phosphorylating reagent, 2-chloro-4,4,5,5-tetramethyl-1,3,2- dioxaphospholane (Santa Cruz Biotechnology) was added to the sample. Acquisition parameters were set to collect 512 scans, with 1 s acquisition time and 5 s relaxation delay. Spectral data were analyzed using MestReNova software.

Two-dimensional (2D) ^{1}H –^{13}C NMR spectra were conducted on a Bruker Avance III 500-Hz NMR spectrometer, and spectral processing was carried out using a Bruker Topspin 3.5 software. The lignin samples (30 mg) were dissolved in 0.4 mL DMSO-d_6 in an NMR tube independently. Heteronuclear single quantum coherence (HSQC) experiments were perfomed with a Bruker pulse sequence (hsqcetgpspsi 2.2) on an N_2 cryoprobe (BBO ^{1}H&^{19}F-5mm) with the following acquisition parameters: spectra width 12 ppm in F2 (^{1}H) dimension with 1024 data points (acquisition time 85.2 ms), 200 ppm in F1 (^{13}C) dimension with 256 increments (acquisition time 5.1 ms), a 1.0-s delay, a $^{1}J_{C–H}$ of 145 Hz, and 128 scans. The central DMSO-d_6 solvent peak (δ_C/δ_H at 39.5/2.49) was used to calibrate the chemical shift position. Assignment and the relative abundance of lignin compositional subunits and inter-unit linkage were estimated using volume integration of contours in HSQC spectra according to published literature.[50] The abundances of aromatic units and

side-chain linkages were presented as percentage of total SGH units and total side-chain linkages, respectively.

Electrochemical performance

Prior to working electrode preparation, the electrode slurries were first prepared by mixing 94.0 wt% activated carbon powder, 5.0 wt% polyvinylidene fluoride (Kynar) and 1.0 wt% black carbon (Super C65) in N-methyl-2-pyrrolidone (NMP) solvent. Subsequently, the stainless-steel substrate was coated with the electrode slurry to obtain a flexible electrode with an area of 2×1 cm^2.

Electrochemical measurements were conducted in a three-electrode system with a Pt wire as the counter electrode and an Ag/AgCl electrode as the reference electrode. Sulfuric acid (H_2SO_4, 1 M) was used as the electrolyte solution. The CV measurements were conducted at different scan rates (10, 30, 50, and 100 mV s^{-1}) within the potential range of 0–1 V. The capacitance was measured by charging and discharging from 1 to 0 V at different current densities. The impedance spectra were recorded with the AC frequency ranging from 100 kHz to 1 mHz. The resulting Nyquist plots were analyzed using the *Z*-view software package.

Results and discussion

Physicochemical properties of lignin

The compositional and elemental analysis of various lignin precursors are provided in the Table 2.2. Table 2.2 includes the purity analysis, average molecular weight and elemental analysis. Table 2.2 details that there is less than 4 and 6% of contaminants for YP and SG, respectively. Additionally, the ash contents are low, 0.02% and 0.03% for YP and SG, respectively, indicating that YP lignin has higher purity than SG lignin. GPC analysis details that YP lignin possesses similar molar-mass dispersity ($Đ_M$) index (M_w/M_n: 3.00 (YP) and 2.96 (SG)) with SG lignin, which reveals the dispersion of the distribution of molar masses in YP and SG lignin.[45, 51] The quantitative CHN of these two lignin sources

Table 2.2 Composition and elemental analysis of YP and SG lignin.

Lignin		**YP**	**SG**
Purity analysis (%)	ASL[a]+AIL[b]	96.60	94.04
	Ash	0.02	0.03
Molecular weight	M_n	2583	2238
	M_w	7747	6625
Molar-mass dispersity ($Đ_M$)	M_w/M_n	3.00	2.96
Ultimate analysis (at.%)	C	64.8	62.1
	H	6.3	6.1
	N	0.2	0.5
	O	28.7	31.3

[a] Acid-soluble lignin.

[b]Acid-insoluble lignin.

are summarized in the elemental analysis, showing that YP lignin possesses a higher carbon content than SG, whereas SG lignin has higher oxygen and nitrogen content.

Hydroxyl units are a key factor that affect the product's thermal and physical properties, which was quantified using ^{31}P NMR.[52, 53] As shown in Figure 2.2 and Table 2.3, YP and SG have similar amount of aliphatic hydroxyl groups, while SG possess a higher amount of phenolic hydroxy groups and carboxylic acid groups. The higher level of carboxylic acid in SG lignin is likely due to the higher concentration of phenolic acids (*p*CA and FA) that are present in grasses.[53] Since YP lignin predominantly contains guaiacol (G) units, the amount of p-hydroxyphenyl OH groups in SG lignin are higher than YP. To further confirm above results, 2D NMR analysis was conducted to investigate the aromatic and aliphatic region in both lignin types, as illustrated in Figure 2.3. Table 2.4 includes the relative abundance of lignin linkages assessed using ^{13}C-^{1}H NMR analysis. The results agree with ^{31}P NMR results confirming higher degree of lignin condensation in YP relative to SG due to the presence of the C_5 position of G units, which provide coupling and cross-linking sites. The linkages of methoxyl (OMe), γ-hydroxylated (A_γ), β-5' phenylcoumaran (B_γ and B_β) groups and β-O-4' (A_α/A_α') can be observed for both lignins. However, SG lignin contains resinol (C_β and C_γ) substructures, which YP lignin does not possess.

Normally, the chemical composition of lignin highly depends on its parent substances. Lignin from grasses (e.g., SG) usually possesses all three units (H-, G-, and S-type), whereas softwood lignin (e.g., YP) are primarily composed of G-type units.[54] As shown in Figure 2.3, the S- and G-units are clearly observed in the aromatic region of the SG sample, with a small amount of H-type units. The S-type units of SG lignin show strong signals for C_2/H_2 and C_6/H_6 in correlation with δC/δH 103.9/6.65 ($S_{2/6}$), and the G-type units display strong correlations at δC/δH: 110.9/7.00 (G_2), 115.1/6.72&6.98 (G_5), and 118.7/6.77 (G_6).

Aromaticity, an indicator of a product's quality as well as its thermal stability, was evaluated for the precursors using TGA, as shown in Figure 2.4(a). The pyrolysis of both

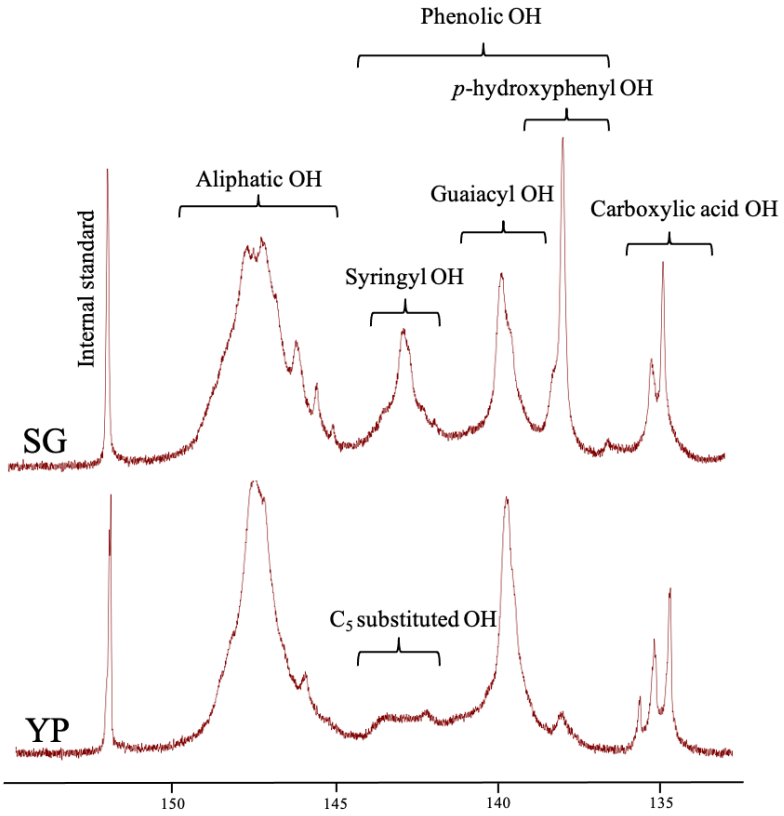

Figure 2.2 Quantitative ^{31}P NMR spectra of SG and YP lignin samples.

Table 2.3 Hydroxyl group contents of YP and SG lignin samples obtained by ^{31}P NMR.

Lignin functional group	Chemical shift (ppm)	YP	SG
Internal standard	152.50 –151.50	0.20	0.20
Aliphatic OH	150.00 –145.00	2.79	2.76
Syringyl OH	145.00 –141.00	0.73*	1.07
Guaiacyl OH	141.00 –138.50	1.28	0.99
p-hydroxyphenyl OH	138.50 – 136.50	0.19	0.70
Total phenolic OH	145.00 – 136.50	2.20	2.76
Carboxylic acid	136.00 – 133.50	0.48	0.57

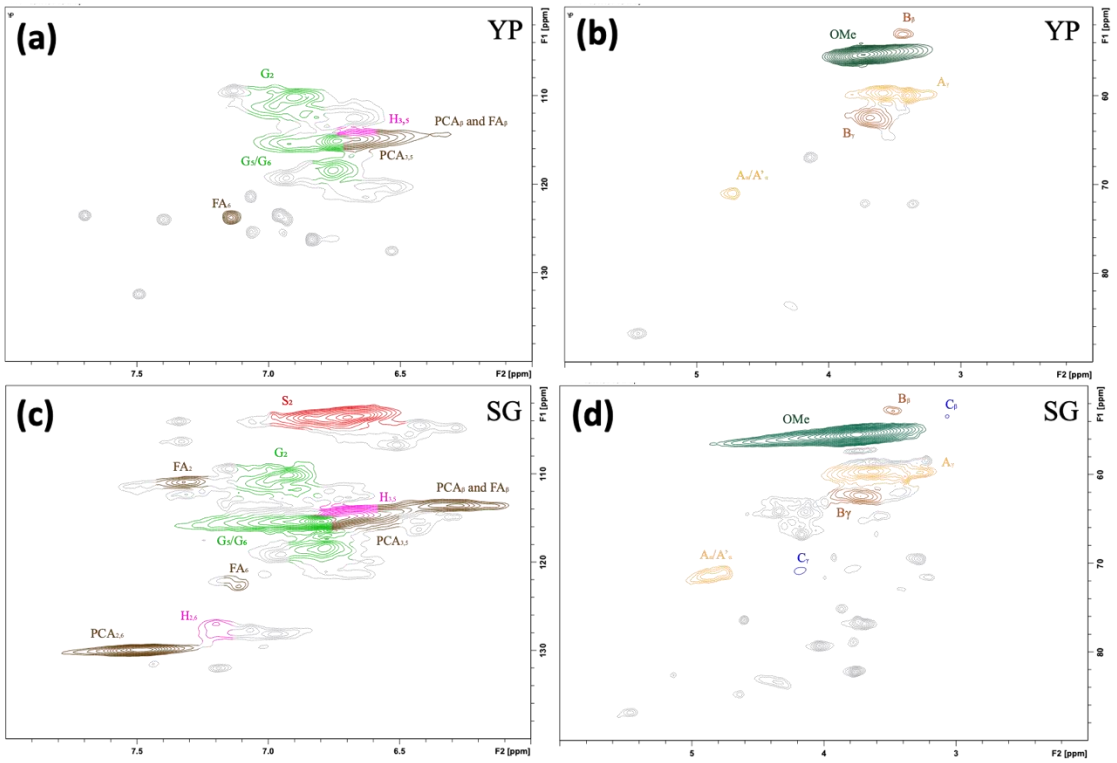

Figure 2.3 2D ^{13}C-^{1}H NMR spectra for different lignin precursors: (a,b) YP and (c,d) SG.

Table 2.4 Relative abundance of lignin linkages using ^{13}C-^{1}H NMR analysis.

	δC/δH (ppm)	**Label**	**Assignment**	**integral**	
				SG	**YP**
Lignin aromatic	2.49/39.5	DMSO	Solvent	1.00	1.00
	103.9/6.65	$S_{2/6}$	C_2/H_2 and C_6/H_6 in etherified syringyl units (S)	0.849	--
	110.9/7.00	G_2	C_2/H_2 in guaiacyl units (G)	0.370	1.046
	115.1/6.72&6.98 and118.7/6.77	G_5/G_6	C_5/H_5 and C_6/H_6 in guaiacyl units (G)	1.832	2.741
	114.8/6.73	$H_{3,5}$	$C_{3,5}/H_{3,5}$ in *p*-hydroxyphenyl units (H)	0.130	0.089
	127.8/7.20	$H_{2,6}$	$C_{2,6}/H_{2,6}$ in *p*-hydroxyphenyl units (H)	0.109	--
	115.5/6.72	$PCA_{3,5}$	C_3/H_3 and C_5/H_5 in p-coumarate (PCA)	1.030	0.259
	130.0/7.48	$PCA_{2,6}$	C_2/H_2 and C_6/H_6 in p-coumarate (PCA)	0.637	--
	113.5/6.27	PCA_β and FA_β	C_β/H_β in p-coumarate (PCA) and ferulate (FA)	0.273	0.033
	111.0/7.32	FA_2	C_2/H_2 in ferulic acid units (FA)	0.123	--
	123.0/7.10	FA_6	C_6/H_6 in ferulic acid units (FA)	0.040	0.134
Lignin aliphatic	53.2/3.47	B_β	C_β/H_β in *β*-5' phenylcoumaran substructures (B)	0.045	0.145
	53.6/3.07	C_β	C_β/H_β in *β*-*β* ' resinol substructures (C)	0.011	--
	55.5/3.75	OMe	C/H in methoxyls	8.233	8.202
	59.8/3.36 & 3.72	A_γ	C_γ/H_γ in normal (γ-hydroxylated) *β*-O-4' substructures (A)	1.142	0.862
	62.5/3.75	B_γ	C_γ/H_γ in β-5' phenylcoumaran substructures (B)	0.251	0.782
	71.2/3.80 & 4.17	C_γ	C_γ/H_γ in β-β' resinol substructures (C)	0.028	--
	71.5/4.75 &71.9/4.89	A_α/A'_α	C_α/H_α in *β*-O-4' substructures (A, A′) –G & -S	0.257	0.156

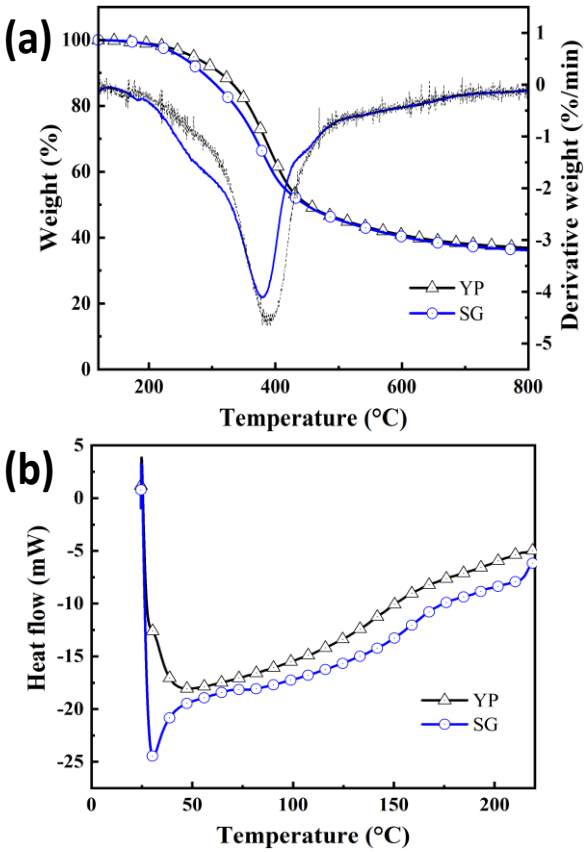

Figure 2.4 (a) TGA and (b) DSC curves of YP and SG lignin precursors.

lignin types presents a similar trend of weight loss starting at 200 °C, which corresponds to the breaking of the weaker bonds such as hydrogen bonds and C-OH binding.[33] Decomposition is observed in the range of 200-300 °C, which proceeded faster for SG due to its higher number of linkages. The maximal loss occurs at 380–390 °C, where the cleavage of stronger bonds, such as β-O-4 linkages begins to degrade.[33] It is important to note that the maximal decomposition temperature of YP is higher than that of SG, at 395 and 385 °C respectively. This implies that YP lignin is more thermally stable compared to SG lignin due to a more robust molecular structure. Eventually the residue takes place at 700 °C with the produced biochar (~40 wt.% fixed carbon). Figure 2.4(b) presents typical DSC curves of both lignin structures, which is used to determine the glass transition behaviors of the lignins. The glass transition temperature (T_g) of SG lignin (155 °C) is higher than that of YP lignin (142 °C) due to more hydroxyl groups in SG samples. Hydroxyl groups play an important role in affecting the thermal properties of lignin, especially the T_g. The existence of hydroxyl groups leads to the formation of hydrogen bonds that subsequently limits molecular movement.[45, 52]

Surface characteristics of activated carbons

Figures 2.5(a) and 2.5(b) demonstrate SEM images of pyrolyzed lignin from YP and SG lignin (i.e., YP-py and SG-py) obtained upon thermal pyrolysis at 1000°C. As illustrated in Figures 2.5, the pyrolyzed lignin exhibits contiguous morphology where the YP-py appears as flat sheets containing numerous cavities, while the SG-py is formed as curved structure. This observation reflects that lignin carbonization occurs during the pyrolysis process, inducing decomposition along with char formation. This dynamic interaction results in releasing gaseous compounds, including oxygen and hydrogen in the form of CO, CO_2, H_2, CH_4, *etc*. This promotes the formation of condensable volatiles due to free radicals generated after the cleavage of inner bonds, usually the C–O bond in the *β*-O-4' substructures.[55] It is important to note that the S-type lignin includes a higher amount of C–O bonds compared to the H- and G-type lignin. The quantitative CHN comparison between these two lignin structures also confirms this trend (i.e., the SG lignin contains

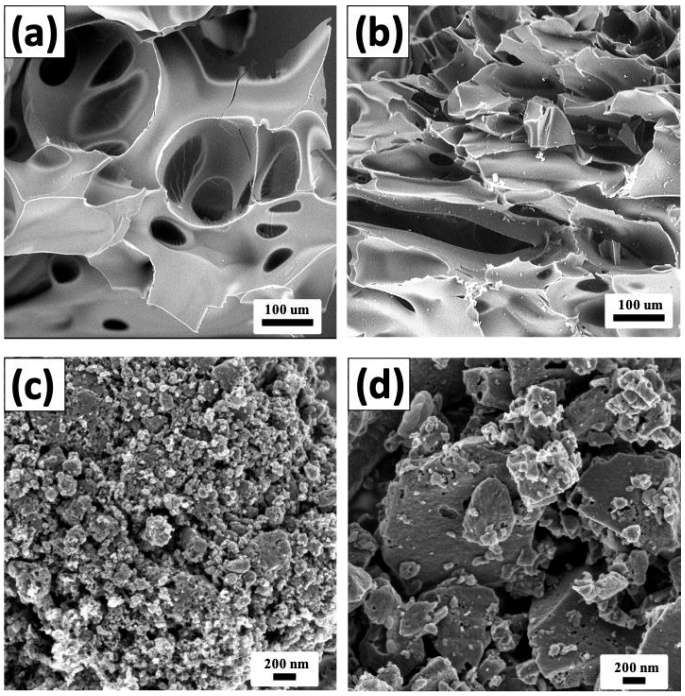

Figure 2.5 SEM images of different lignin precursors: (a) YP-py and (b) SG-py and SEM images of different ball-milled AC samples: (c) YP-AC and (d) SG-AC.

higher O/C ratio (~50.4%) than YP (~44.3%), as summarized in Table 2.2). This correlation implies the SG lignin is more easily decomposed compared to the YP lignin upon thermal pyrolysis. After pyrolysis, the lignin is converted into char with high carbon content and abundant surface functional groups, but limited surface area.[33] As shown in Figure 2.6, XPS survey-scan spectra confirms the presence of carbon (C 1s) and oxygen (O 1s) in both pyrolyzed lignin samples. In addition, it is notable that there is a small amount of inorganic impurity, which is sodium (Na 1s) peak located at ~1072 eV, in YP-py sample. Elemental analysis shows the O/C ratio of SG-py (~8.1%) is lower than YP-py (~15.2%), and there is ~3.6% Na in YP-py. The surface area obtained by BET measurements of YP-py and SG-py samples are all negligible. It is well documented that both surface area and pore volume increase as a result of the activation process.[34] The increase in porosity of YP-AC and SG-AC can be attributed to the opening of closed pores and/or enlarging of the micropores due to gasification of the carbon during the activation process.[56]

SEM images of activated carbons prepared from YP and SG lignin are illustrated in Figures 2.5(c) and 2.5(d), respectively. According to Figure 2.5, it is obvious that the smaller carbonaceous aggregate size, and greater porosity is present with YP-AC compared with SG-AC. Table 2.5 includes characteristics of different porous carbons determined from analysis of the N_2 adsorption isotherms at -196 °C. Based on BET measurements, the YP-AC sample possesses a specific surface area of ~1070 m^2 g^{-1}, which is approximately two times higher than that of SG-AC (~507 m^2 g^{-1}). The YP-AC sample contains a higher percentage of mesopore (~44%), whereas the SG-AC is mainly microporous due to the presence of 89% micropore volume. The DFT method was employed to analyze the full-range pore size distribution of both carbon samples, as shown in Figure 2.7. The DFT analysis reveals different pore size distributions within the structure, where the YG-AC sample possesses a sharp peak at the pore size of *ca*. 1–2 nm, and a smaller but broad distribution ranging up to 50 nm, while the SG-AC sample exhibits one major lump at *ca*. 1–2 nm. Since both carbon samples were thermally treated through a similar pyrolysis and

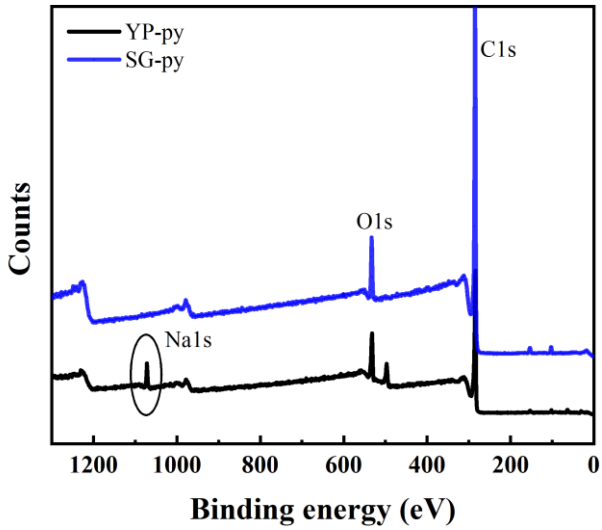

Figure 2.6 Survey-scan XPS spectra of YP-py and SG-py samples.

Table 2.5 Pore structures of activated carbons prepared from YP and SG lignin precursors.

Carbon type	Specific surface area		Pore volume		
	S_{BET} ($m^2\ g^{-1}$)	S_{BJH} ($m^2\ g^{-1}$)	V_t ($cm^3\ g^{-1}$)	V_{micro} (%)	V_{meso} (%)
YP-AC	1070	467	1.27	56	44
SG-AC	507	56	0.29	89	11

S_{BET}: Specific surface area computed using BET equation.

S_{BJH}: Specific surface area computed using BJH equation.

V_t: Total pore volume estimated at a relative pressure of 0.98.

V_{micro}: Micropore volume determined from *t*-plot method.

V_{meso}: Mesopore volume determined from the subtraction of micropore volume from total pore volume.

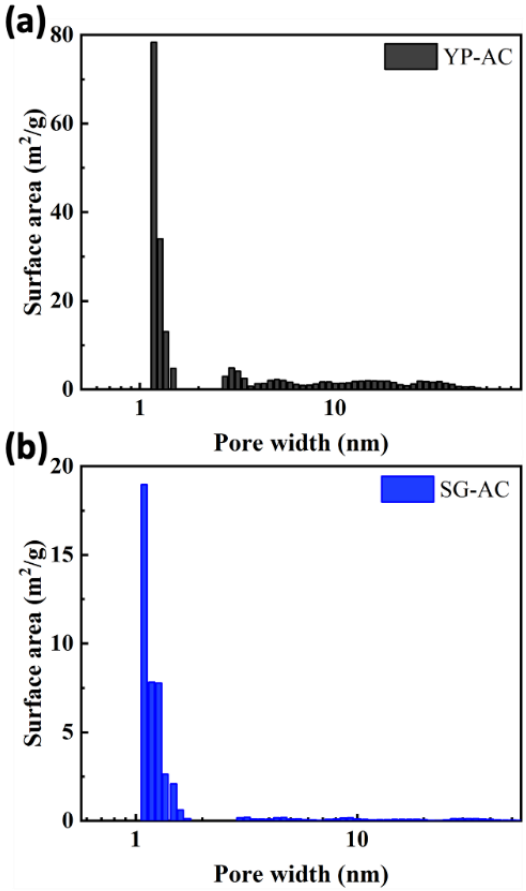

Figure 2.7 Pore size distributions of activated carbons prepared from (a) YP and (b) SG lignin precursors.

two-step activation method, this variation in the morphology of the activated porous electrodes implies that surface area, porosity, and pore size distribution is strongly dependent on the lignin nature.

Physical activation usually involves three mechanisms, including surface burn-off, pore deepening, and pore widening during the carbon gasification (i.e., activation process). For the YP carbon with high O/C ratio, it is more prone to surface burn off and the oxidation reaction induced by the oxygen functional groups that facilitate the pore widening by destroying the microporous structures.[34] On the other hand, the extent of carbon agglomeration in YP-py is less than that in SG-py, indicating more surface area of YP-py is accessible to CO_2/H_2O upon activation. More pores could be evenly widened and the closed micropores are allowed to be opened during gasification.[8] In addition, it has been demonstrated that the presence of Na shas a significant catalytic effect during the activation,[33, 57] which contributes to the high surface area of YP-AC. As for the SG carbon, with relatively low O/C ratio, the accessibility of the activation agents, H_2O and CO_2, increases with the extent of the burn-off and subsequently results in a parallel reaction step with pore deepening and pore widening. The difference between the YP and SG chars results in different porosities as well as pore size distributions. Therefore, the O/C ratio, char structure, and inorganic impurities are key factors that lead to highly porous ACs.

Elemental analysis shows that the YP-AC and SG-AC contain high O/C atomic ratios of 7.3 and 10.5 %, respectively. This observation reveals that both produced ACs possess high oxidation levels (i.e., many oxygen functionalities attached to porous carbon). XPS spectra (see Figures 2.8(a) and 2.8(b)) were obtained to confirm the presence of surface functional groups on the carbons. The full spectra are presented in Figure 2.8(a) with the typical C 1s and O 1s peaks located at ~285 eV and ~531 eV, respectively. The C 1s peak (shown in Figure 2.8(b)) was split into three peaks located at 284.6 ± 0.1 eV (C=C or C–C), 286.5 ± 0.1 eV (C-O) and 288.9 ± 0.1 eV (C=O or O-C=O). This result is further confirmed by FTIR spectra, which are displayed in Figures 2.8(c) and 2.8(d). The peak occurring at ca.

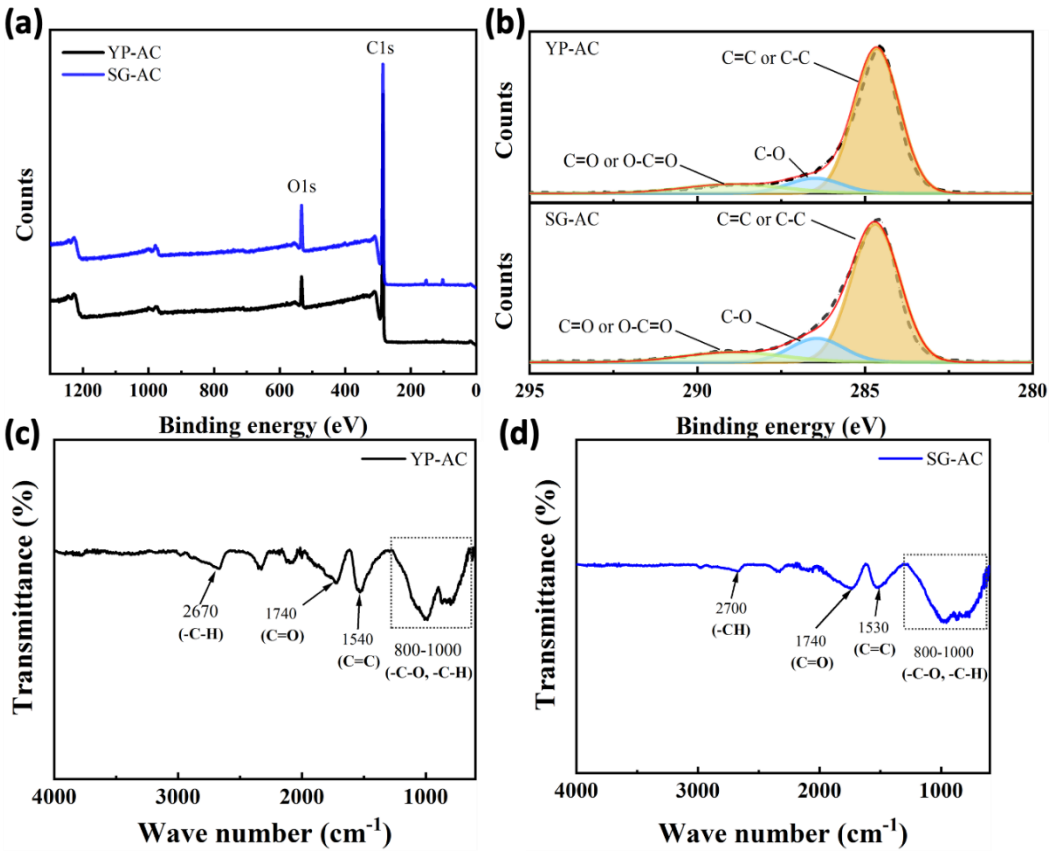

Figure 2.8 (a) Survey-scan XPS spectra of YP-AC and SF-AC samples, (b) C 1s peak of YP-AC and SG-AC samples. FTIR spectra of activated carbons (c) YP-AC and (d) SG-AC.

1540 cm^{-1} is assigned to the presence of C=C stretching.[58] The strong peaks in the range of 800–1300 cm^{-1} are due to stretching of the C–O and –COOH bonds.[59-61] The transmittance peak appears at around 1740 cm^{-1}, mainly originating from the C=O stretch in various functional groups (i.e. ketones, carbonyls, esters, carboxylic acid groups, etc.).[62, 63] Based on the FTIR spectra, oxygen functional groups exist on both activated carbons samples, attached to edge or basal plane of carbons.

Electrochemical performance of supercapacitors

Typical CV curves of capacitors assembled with YP and SG carbons were recorded within the potential range of 0 to 1 V at various sweep rates as illustrated in Figures 2.9(a) and 2.9(b). As shown in Figure 2.9, the voltammograms of the carbon electrodes display an obvious pair of redox peaks at 0.3–0.5 V. The CV profiles demonstrate a pseudo capacitance behavior where the induced current increases with increasing sweep rate. Additionally, a rectangular voltammogram, in which the current quickly reaches and maintains a relatively constant magnitude (Figure 2.9) upon reversal of the potential sweep can be maintained, although it shows current leakage at such high sweep rates (e.g., 100 mV s^{-1}) for both capacitors. The current density of the supercapacitors assembled with the YP carbon electrode was higher compared to that of SG electrodes due to larger available surface area of the YP carbon structure, enabling (i) the formation of electric double-layer and (ii) the redox reaction in the presence of oxygen functionalities.

The formation of carbon electric double layer with acidic electrolyte and subsequent charge/discharge processes can be formulated using equation (R1):[64, 65]

$$C^* + H^+ \leftrightarrow C^*//H^+ \qquad (R1)$$

Here, C* is the active carbon sites, H^+ represents the protons, and the double layer where the charges accumulated separately on two sides of the interface is shown as //. It formulates a physical adsorption process induced by electrostatic forces between the carbon substrate and the protons. The pseudocapacitance, originated from the oxygen functional groups with electron-accepting properties, such as carbonyl and quinone groups,

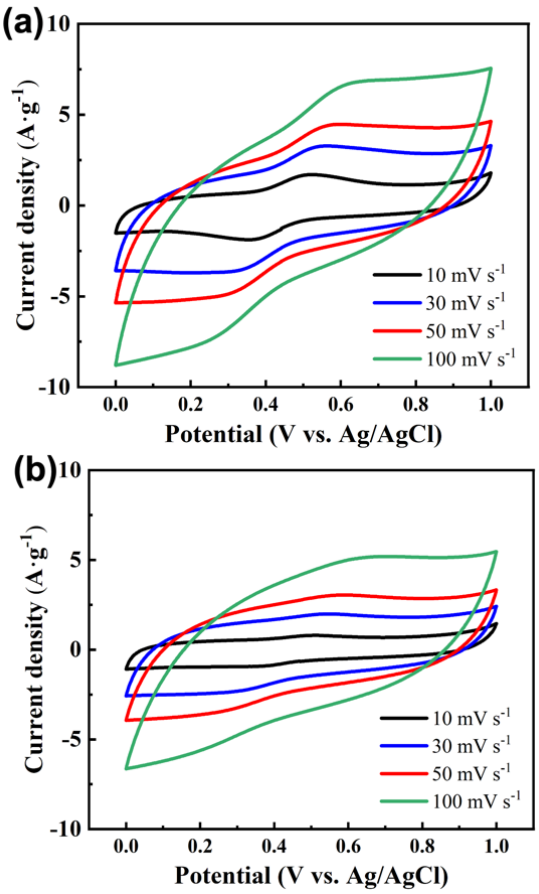

Figure 2.9 Cyclic voltammetry profiles of (a) YP-AC and (b) SG-AC electrodes in 1 M H_2SO_4 at different scan rates.

also induces redox reactions during the electron transfer process:[65, 66]

$C_xO^* + H^+ + e^- \leftrightarrow C_xOH$ (R2)

where C_xO^* represents carbonyl and quinone groups. Since YP carbon has higher porosity with an increased oxidation level, it provides more hydrophilic sites accessible for the double-layer formation and redox reaction, promoting the progress of (R1) and (R2) reactions.

Figures 2.10(a) and 2.10(b) show typical charge-discharge profiles of YP and SG capacitors at 0.5 and 2.5 mA cm^{-2}, respectively. The YP capacitor exhibits higher capacitance for both charge and discharge cycles and demonstrates reduced 'IR drop' at the beginning of discharge. Such a small "IR drop" is mostly due to higher ionic conductivity and lower diffusion resistance of the electrolyte within the porous carbon structure.[66] Also, as shown in Figure 2.9, one charge-discharge plateau at 0.4–0.5 V, attributed to the pseudocapacitance from the redox reaction step (R2). The variation of specific capacitance with discharge current density, from 0.1 to 2.5 mA cm^{-2}, is depicted in Figure 2.10(c). At 0.1 mA cm^{-2}, the specific capacitances of YP and SG were ~367 and 221 F g^{-1}, respectively. The specific capacitance was found to decrease with increasing discharge current, which displays a trend confirmed by other research.[67]

To assess the stability of as-prepared porous electrodes, extended charge-discharge cycling was performed at 10 mA cm^{-2}. The capacitors equipped with YP and SG electrodes were charged and discharged between 0 and 1 V repeatedly, as shown in Figure 2.10(d). Analyzing the variation of discharge capacitance with cycle number revealed that the YP capacitor has superior and stable capacitance (capacitance retention > 90%) and exhibits excellent coulombic efficiency (> 99%) over long-term cycling (> 10000 cycles).

The EIS technique was employed to analyze the electrochemical behavior of the capacitors assembled with various lignin-based electrodes. The impedance spectra of different capacitors are shown as Nyquist plots in Figure 2.11(a). As illustrated in Figure 2.11, the

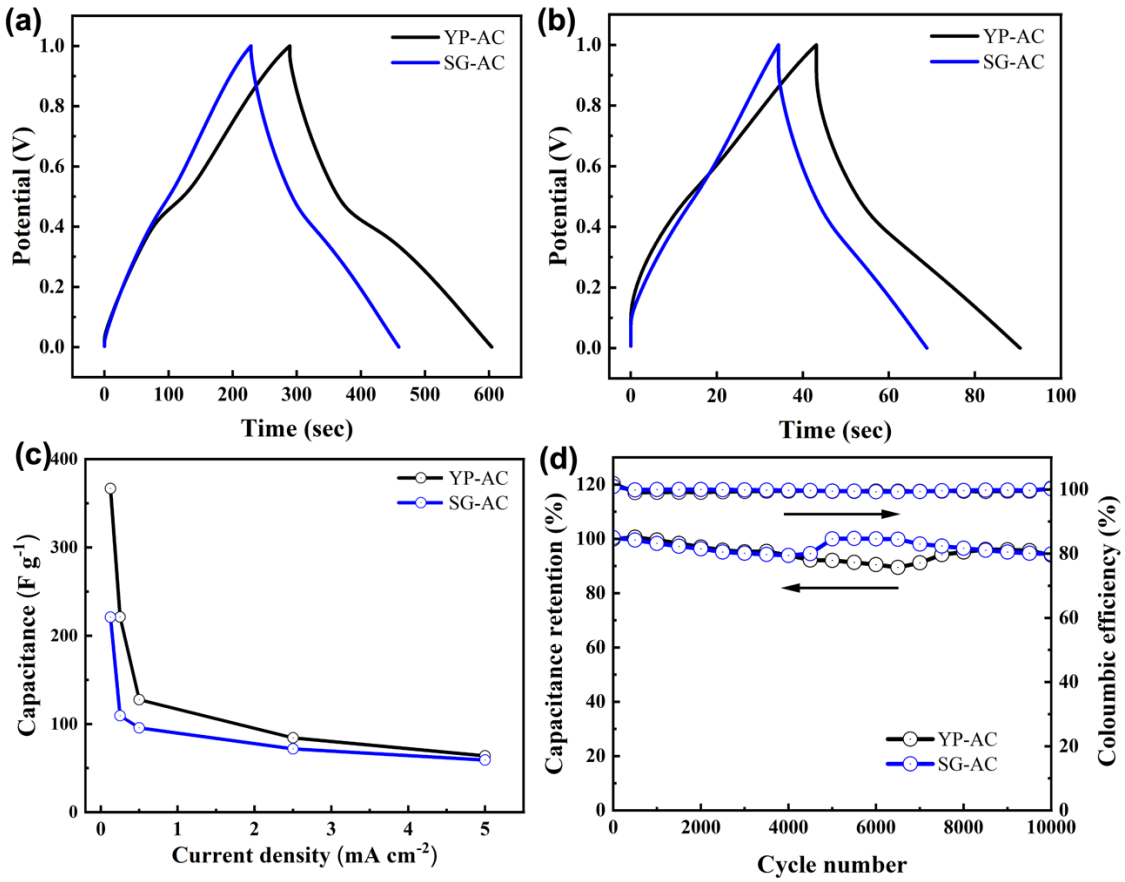

Figure 2.10 Charge-discharge curves of different capacitors at (a) 0.5 and (b) 2.5 mA cm^{-2}, (c) variation of specific capacitance with current density, and (d) cyclic performance of different capacitors at 10 mA cm^{-2}.

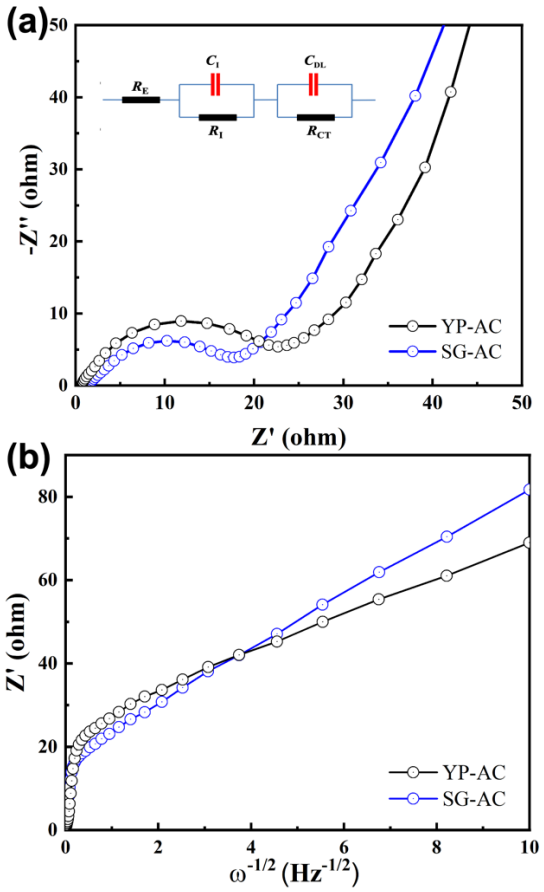

Figure 2.11 Nyquist plots of different capacitors at OCV, where an equivalent circuit was proposed for describing the impedance behavior within the frequency range between 100 kHz and 1 Hz. (b) Randles plots of different capacitors at open circuit voltage.

high-frequency intersection with the real axis represents the electrolyte resistance (R_E), followed by a single quasi-semicircle in the high-frequency region (100 kHz - 1 Hz). The semicircle in the high-frequency region is due to combined effect of interfacial resistances (between activated carbon composites and current collector (R_I//C_I)), as well as the charge transfer impedance (R_{CT}//C_{DL}, a double-layer capacitance in parallel with a resistance).[56] The EIS spectra also include a slant line in the low frequency region corresponding to the capacitive response of the porous carbons.[68] The equivalent circuit model used for simulating the impedance behavior of the capacitors is shown in the inset of Figure 2.11(a). The *Z*-view software package was adopted for fitting the EIS spectra with the equivalent circuit model. The overall resistance, so-called "equivalent series resistance", R_{ES} (= R_E + R_I + R_{CT}), was composed of the electrolyte resistance, interfacial impedance, and charge transfer resistance. The R_{ES} values were 28.7 and 24.8 Ω for YP and SG capacitors, respectively. The slightly higher R_{ES} value of YP electrode is attributed to higher surface area and more complex porous structure, resulting in the high resistance for charge transfer within the pore structure.

As shown in Figure 2.11(a), the Nyquist plot displays an inclined line at low frequencies (< 1 Hz), resulting from the solid-state diffusion process of protons within the porous electrodes. Meanwhile, Warburg impedance (Z_D) in the electrodes can be formulated as $Z_D = k_W \omega^{-1/2} (1 - j)$, based on semi-infinite diffusion model. Here, k_W represents the Warburg coefficient and ω (= $2\pi f$) is the angular frequency (f). Figure 2.11(b) presents the "Randles plot", Re Z' versus $\omega^{-1/2}$, for both capacitors. The diffusion coefficients (D) determined from the k_W value were 4.77×10^{-10} and 2.16×10^{-10} cm^2 s^{-1} for the YP and SG capacitors, respectively, detailing the D value of YP capacitor was 2.21 times higher than that of SG. This finding reveals that the ionic diffusion resistance is significantly alleviated for the YP electrodes, leading to fast redox reaction (i.e., R2) and rapid formation of electric double-layer (i.e., R1) in the mesoporous carbon. Accordingly, the unique pore texture of the YP structure significantly facilitates the electrochemical reactions. Shorter diffusion path,

along with increased mesopores and surface area available for energy storage with the YP carbon structure, were the major contributing factors for the improved performance.

Techno-economic analysis

To demonstrate the economic feasibility of the approach, the minimum selling price (MSP) of activated carbons produced by using YP and SG as feedstocks is estimated. Four steps are taken to perform techno-economic analysis.

Process Synthesis

First, a process is designed to convert biomass to activated carbons. The process consists of eight areas as shown in Figure 2.12, resulting in the production of cellulose, furfural, and activated carbons. All processes were performed at the 100's g scale. The purpose of the biomass fractionation area (A100) is to isolate the solid cellulose fraction from the dissolved hemicellulose and lignin fractions. The liquid fraction from A100, containing C_5 sugars and lignin is sent to lignin recovery area (A200). While GVL solubilizes lignin, by adding water lignin is precipitated, while the C_5 sugars remain soluble. The liquid stream containing C_5 sugars from A200 is concentrated and sent to furfural production area (A300) for converting it to furfural. The effluent stream from the furfural production reactor contains water, GVL, and furfural. To obtain pure furfural as an additional co-product, it needs to be separated from GVL and water. Furfural and water are readily separated from the high-boiling point GVL (208 °C), facilitated by the low boiling point of the furfural/water azeotrope. Separation of furfural and water is similar to the distillation step currently used in the commercial production of furfural.[69] More details regarding the areas A100, A200, and A300 were previously reported by Alonso et al.[70]

Lignin recovered from A200 is sent to the lignin activation area (A400), where it is reduced to activated carbons. Lignin is carbonized in a nitrogen atmosphere at 1000 °C and 1 bar. We assumed that an air separation unit is installed onsite for supplying the required N_2. The required mass ratio of N_2/lignin is 11 for both YP and SG lignin. The reactor effluent

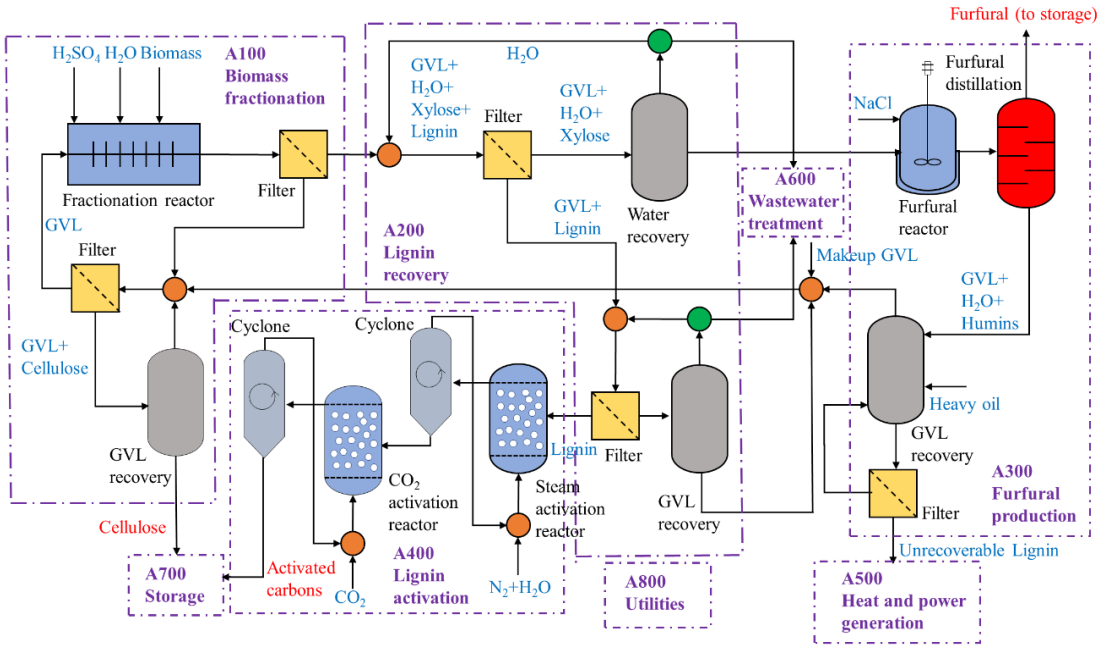

Figure 2.12 Simplified process flow diagram to produce activated carbons, furfural, and cellulose from biomass.

contains components in solid and gas phases, which are separated by a cyclone. The activation takes place in a mixed atmosphere of steam and nitrogen in a reactor operating at 800 °C and 1 bar. The required mass ratio of gas to inlet solid is 13 for SG and 14.4 for YP lignin. The solids from the second activation reactor are further reduced in the presence of CO_2 in the third reactor operating at 800 °C and 1 bar. We assume that the required amount of CO_2 is available for purchase. The mass ratio of solid to gas required for SG and YP lignin are 2.9 and 2.2, respectively. According to the process described, 1 MT of YP is converted to 521 kg of cellulose (70% pure), 40 kg of activated carbons, and 50 kg of furfural (99% pure) and 1 MT of SG is converted to 410 kg of cellulose (83% pure), 55 kg of activated carbons, and 149 kg of furfural (99% pure).

Ancillary areas including heat and power generation (A500), wastewater treatment (A600), storage (A700), and utilities (A800) are included in the design. Unrecoverable lignin and natural gas required to meet the process heating and electricity requirements are combusted in A500. Most of the heating demand is met from the evaporators used to recover GVL and distillation columns and the electricity demand is met from the compressors and the air separation unit. The process wastewater streams are treated by anerobic and aerobic digestion in A600. Area A700 is used to store bulk chemicals. Area A800 includes a cooling water system, chilled-water system, process water manifold, and power systems.

Process Modeling

Second, based on experimental results, Aspen Plus process models are developed to estimate material and energy flows. The base design considers annual production rate of 5.5 kton of activated carbons. This production rate is chosen to mitigate the risks associated with initial investment scale and ensure that only a fraction of the current market volume of supercapacitor-grade carbon is produced. The material flow information for the main streams is given in Table 2.6.

Next, the total energy requirements of the process are estimated after heat integration is

Table 2.6 Material flow rate of the main streams based on the process flow diagram shown in Figure 2.12.

Streams	Flow rate (kg/h)	
	YP biorefinery	SG biorefinery
Biomass	17,507.0	12,742.1
GVL	419.1	305.0
H_2SO_4	307.9	224.1
NaCl	120.7	87.9
Heavy oil	89.7	65.3
N_2	3,661.7	2,767.5
CO_2	35.3	26.6
Cellulose	9,103.6	5,224.3
Furfural	875.4	1892.2

performed. The heating, cooling, and power requirements of the process with YP as the feedstock are 10.8 MW, 17.1 MW, and 3.5 MW, respectively. When SG is used as the feedstock, the heating, cooling, and power requirements are 8 MW, 12.4 MW, and 2.5 MW, respectively. A part of the heating and electricity requirements are satisfied by combusting biomass residues and the remaining are satisfied by natural gas.

Estimating Capital and Operating Costs

Third, the capital costs as well as the variable and fixed operating costs are estimated. All equipment costs are adjusted to a common year (2019) using appropriate cost indices. The installed costs of all the areas except A400 are estimated based on the article by Alonso et al,[70] using appropriate scaling factors. Detailed installed equipment costs of A400 are given in Table 2.7 and a summary of the capital costs of different areas are provided in Table 2.8. The total capital investment (TCI) of YP and SG biorefineries are estimated to be $229 million and $189 million, respectively. The main reason for the higher TCI of the YP-based biorefinery is the lower yield of activated carbons. The annual fixed operating costs accounting for salaries, maintenance, and insurance are estimated to be $9.3 million and $8.5 million for YP and SG biorefineries, respectively. Based on the raw material prices listed in Table 2.9, the annual variable operating costs of YP and SG biorefineries are estimated to be $15.2 million and $12.1 million, respectively.

Process Economics

Fourth, a discounted cash flow analysis is used to determine the minimum selling price of activated carbons, under the financial assumptions given in Table 2.10. The internal rate of return has been set at 30% instead of the typical 10% to reflect the higher risk of investing in a new technology. We assume that cellulose and furfural can be sold as coproducts. In recent years, cellulose price has varied between $700 - $900 per ton.[71] Because of the initial technical risk, a lower selling price of $700/ton is used for the SG-based cellulose. Since cellulose produced using YP is 70% pure, a selling price of $600/ton is assigned. Furfural price has ranged between $1000 -1800 per ton in the recent years.[72] In our analysis, the

Table 2.7 Detailed capital costs of the equipment in A400.

Equipment	Quantity	Equipment installed costs (Million $)		Source
		YP biorefinery	SG biorefinery	
Air separation unit	1	2.2	28.2	[73]
Fluidized bed reactor	3	2.9	30.1	[74]
Cyclone	3	0.1	5.5	Aspen Plus
Ball Mill	1	0.07	4.6	Aspen Plus
Compressor	3	0.6	20.6	[75]

Table 2.8 A summary of capital costs of different process areas.

Area	Capital costs (Million $)	
	YP biorefinery	SG biorefinery
A100	34.2	28.2
A200	36.4	30.1
A300	6.7	5.5
A400	5.9	4.6
A500	24.9	20.6
A600	8.0	6.6
A700	2.7	2.3
A800	1.9	1.5

Table 2.9 Raw material prices and sources.

Component	Price ($/ton)	Source
YP	70	[76]
SG	80	[76]
H_2SO_4	86	[77]
GVL	1000	[78]
NaCl	182	USGS
Heavy oil	330	Baytex energy
Lime	237	[76]
CO_2	70	[79]
Boiler chemicals	5950	[76]
Cooling tower chemicals	3565	[76]
WWT nutrients	5251	[76]

Table 2.10 Financial assumptions.

Plant life	30 years
Capacity factor	90% (7884 hr/year)
Internal rate of return	30%
Plant depreciation	7 years
Loan terms	10-year loan at 8% APR
Construction time	3 years
Financing	40% equity
Federal tax rate	21%
First 12 months' expenditure	8%
Second 12 months' expenditure	60%
Last 12 months' expenditure	32%
Start-up time	6 months
Working capital	5% of fixed capital investment
Revenue during start-up	50%
Variable operating costs during start-up	75%
Fixed operating costs during start-up	100%

price of furfural is fixed to $1000 per ton, which is competitive in the current market. All coproducts (cellulose and furfural) are treated using a market value allocation approach in a consistent manner with the NREL's studies.[80]

The results of the analysis are shown in Figure 2.13. The process areas for biomass fractionation, lignin recovery, and heat and power generation are the major cost contributors. The revenues from the production of cellulose and furfural significantly reduce the MSP of activated carbons. The activated carbons from YP and SG can be produced at an MSP of $8493 and $6670 per ton, respectively. Notably, the current selling price of supercapacitor-grade activated carbon is $13600/ton.[81] The activated carbons produced, especially from YP lignin, demonstrated remarkable electrochemical performance.[49] This illustrates that the proposed strategy of utilizing a lignin stream to produce activated carbons is promising and provides an opportunity for successful translation to an economically viable commercial process. The impact of the prices of cellulose and furfural on the MSP of activated carbons (shown in Figure 2.14) was also studied. If the price of cellulose is varied between $500-$1000/ton and the furfural price varies in the range of $1000-$1500/ton, the MSP of YP and SG activated carbons range from $2666-9793/ton and $3080-8162/ton, respectively. It can be observed that due to higher yield of furfural from SG, the furfural price impacts the MSP of SG activated carbons to a higher degree than YP-ACs.

Conclusions

This research employed two types of lignin (YP and SG) as the precursors for synthesizing porous activated carbon electrodes for supercapacitors. The pyrolysis and activation of lignin feedstocks results in porous activated carbons, with surface area and pore size distributions that can be tailored by feedstock choice and processing conditions. The structure of the ACs dictates adsorptive capacity and the diffusion rates of penetrating ions, which are reflected in the electrochemical performance of these materials as supercapacitors. 2D ^{1}H–^{13}C NMR were used to characterize the S/G/H alcohol units of

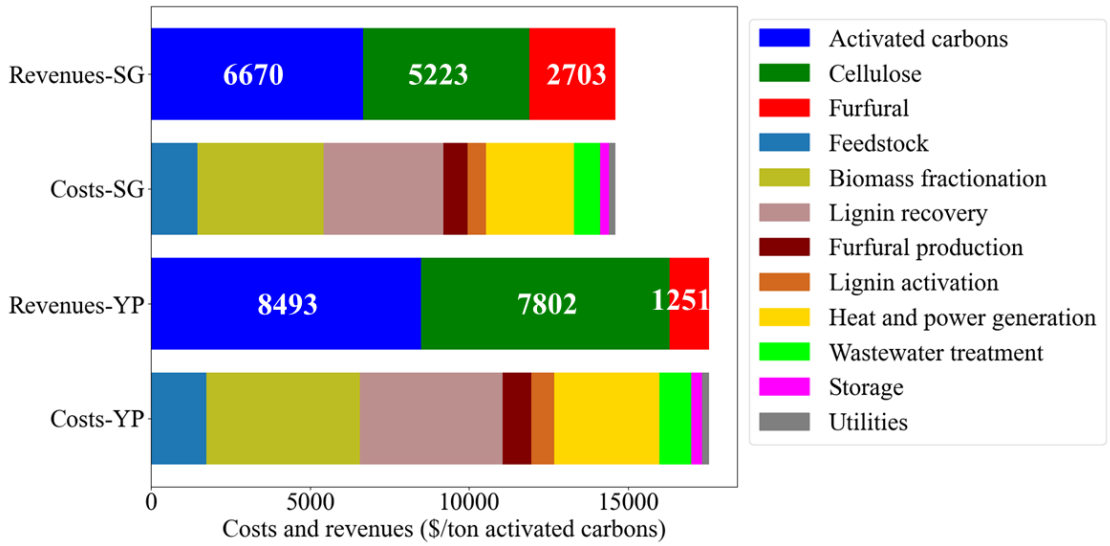

Figure 2.13 Cost breakdown by process area for SG and YP-based biorefineries.

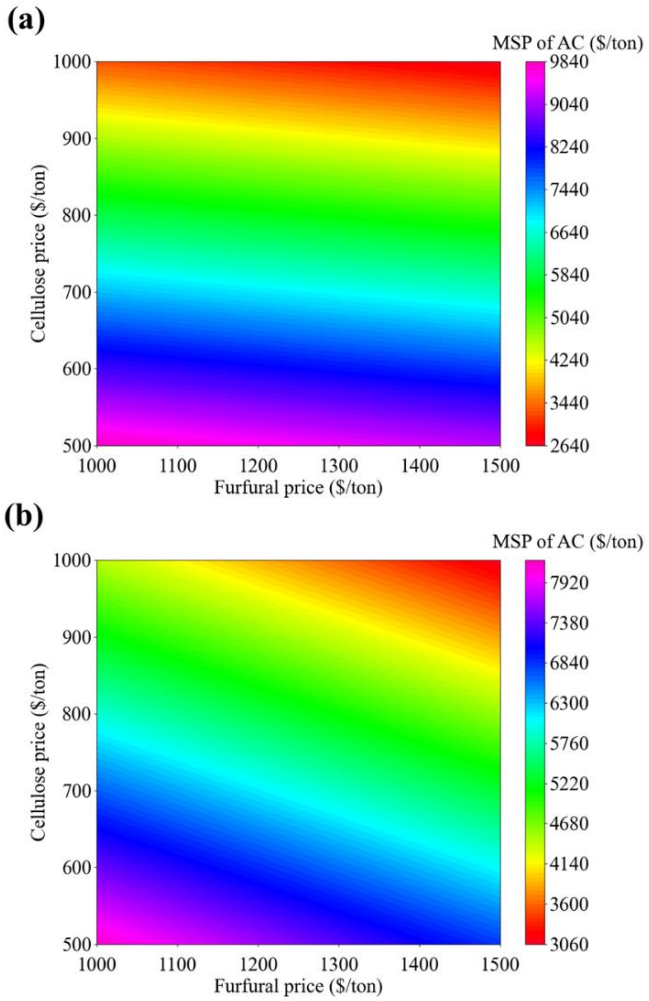

Figure 2.14 Impact of furfural and cellulose price on the MSP of activated carbons produced in (a) YP and (b) SG-based biorefineries.

lignin-based electrodes, which are important indices in evaluating biochar structures and pore characteristics of the activated carbons. The different O/C ratios, carbon aggregations, and inorganic impurities between the YP and SG chars were determined to be critical factors inducing differing porosities and pore size distributions through a two-step activation process. Higher O/C ratios, less extent of carbon aggregations, and presence of inorganic impurities were easier to achieve for highly porous activated carbon structures. Based on the electrochemical performance of as-prepared electrodes, the specific capacitances of YP and SG capacitors reached 367 and 221 F g^{-1}, respectively. The YP capacitor displayed stable capacitance (the capacitance retention: > 90%) and excellent Coulombic efficiency (>99%) over 10,000 cycles. Analyzing the Randles plots, the apparent D values, was determined to be 4.77×10^{-10} and 2.16×10^{-10} cm^2 s^{-1} for the YP and SG capacitors, respectively. This remarkable performance improvement of the YP carbon electrodes was likely the result of a shorter diffusion path and higher available active surface area for energy storage. Techno-economic analysis indicates that YP and SG capacitors can be produced at a minimum selling price of $8,493 and $6,670 per ton, respectively, which is competitive with the price of commercially produced supercapacitors. The novel lignin based activated porous carbon electrodes developed in this work paves the way for engineering inexpensive and high-performance electrode materials for various electrochemical energy devices.

Chapter 3 Hierarchical Lignin-Based Carbon Matrix and Carbon Dot Composite Electrodes for High-Performance Supercapacitors

A version of this chapter was originally published by Yu, L., Hsieh, C.-T., Keffer, D.J., Chen, H., Goenaga, G.A., Dai, S., Zawodzinski, T.A., Harper, D.P.:

Yu, L., Hsieh, C.-T., Keffer, D.J., Chen, H., Goenaga, G.A., Dai, S., Zawodzinski, T.A., Harper, D.P., 2021. Hierarchical Lignin-Based Carbon Matrix and Carbon Dot Composite Electrodes for High-Performance Supercapacitors. ACS Omega 6, 7851–7861.

Credit authorship contribution statement:
Conceptualization, LY, C-TH, DH; methodology, LY, C-TH, DK, SD, TZ, DH; validation, LY, HC, GG; formal analysis, LY, C-TH; resources, DK, SD, TZ, DH; writing—original draft preparation, LY; writing—review and editing, C-TH, DK, HC, SD, GG, TZ, DH; visualization, LY; supervision, DH, DK, SD, TZ; project administration, DH; funding acquisition, DH, SD, TZ.

Abstract

This work adopts an efficient chemical-wet method to build a three-dimensional (3D) carbon composite as electrode materials for high-performance supercapacitors. Carbon quantum dots (CQDs), prepared by thermal pyrolysis of citric acid and urea under microwave at 280°C, are homogeneously coated onto lignin-based activated carbons (ACs), thus forming the 3D composites possessing an interior surface decorated with CD binding sites. Benefiting from the hydrophilicity and ultrafine size of CQDs, the affinity of the electrode surface towards aqueous electrolyte are significantly improved with the addition of CQDs, leading to the enhanced effective surface area (i.e., abundant electroactive sites) and decreased ionic diffusion path. The capacitance of the supercapacitors is improved from 125. 8 F g^{-1} to 301.7 F g^{-1} with CD addition. The supercapacitor with CD addition possesses improved cycle stability with coulombic efficiency around 100% after 3000 cycles. After cycling, the ions diffusion coefficient of CD@AC-11 electrode is enhanced by 25.5 times as compared to that of pristine AC one. This unique and robust carbon

framework can be utilized for engineering desired pore structure and micropore/mesopore fraction within the AC electrodes. This strategy of CD@AC electrodes demonstrates a promising route for using renewable porous carbon materials in advanced energy-storage devices.

Introduction

With the increasing need for energy storage and environmental substantiality, supercapacitors (SCs) promise to be important energy storage devices possessing high power density, long cycle life, excellent cycling stability, and low cost.[82-84] Based on different work mechanisms, SCs are generally classified into faradaic pseudo-capacitors and electric double-layer capacitors (EDLCs).[85, 86] Theoretically, pseudo-capacitance originates from the faradaic process between the electrodes and electrolytes via charge transfer across the interface. Transition metal oxides and conductive polymers, which possess redox sites and intrinsic high electrical conductivity, are typical pseudo-capacitive materials.[87, 88] EDLCs are based on the Helmholtz model that the charges are separated at the polarization interface between electrode and electrolyte. There is no charge transfer involved in favor of reversible adsorption and desorption. This energy storage mechanism enables quick charge/discharge rate as well as superior cyclability.[89-91] Versatile activated carbon (AC) materials have been extensively studied as electrodes for EDLCs as they possess the high specific surface areas (SSAs) needed for high capacity.[92, 93] However, it is generally recognized that not all pores are electrochemically accessible; imperfect connectivity of the porous network leaves some pore volume inaccessible to ions.[94] In addition, tortuous microporosity leads to long diffusion distances, thus resulting in relatively high ionic diffusion resistance.[95] Pioneering work has been devoted to maximizing the accessible SSAs of ACs, such as heteroatom doping into porous carbon framework to increase the wettability,[96-98] modifying pore distribution by using different precursors[99], and matching electrolytes.[100-102]

Lignin is an organic polymer with condensed carbon backbone structure and complex

aromatic functional linkages.[103] After pyrolysis and activation, there are still a small amount of impurities, such as N and O, which provide extra electroactive sites.[104, 105] However, the porous structure of lignin-based ACs consists predominantly of narrow micropores,[105-107] a significant fraction of which remains inaccessible to ions. This drawback greatly limits effective surface areas, porous accessibility, and wettability of lignin-based carbon electrodes.

Carbon quantum dots (CQDs), also called "carbon quantum dots", are highly crystallized zero-dimensional materials which have been used in various energy applications due to their excellent electrochemical properties and ultrafine particle size.[21, 108-110] CQDs usually have very small particle size, ranged from 2 to 30 nm. Abundant functional groups, such as carboxylic, carbonyl, and amino groups, tend to bond with the carbon core or on the CD surface. The presence of surface functionalities leads to high hydrophilicity of CQDs and homogeneous dispersion in polar solvents.[110, 111] The high functionality suggests the use of CD as active sites, decorating the interior pore space of ACs, where they can interact with ions or hydrating species during the charge/discharge process. Researchers have tried to integrated CQDs into the porous carbon frameworks by one-step calcination-activation method and employed them as the EDLC materials. With the CQDs fused into the carbon skeleton, the surface roughness was increased and thus achieving high surface area, which led to the higher capacity.[112, 113] CQDs were also applied as the electrodes for batteries and achieved better cycle ability and higher capacity due to the special carbon frame structure with larger interlayer space and large surface area.[114]

In this work, we applied N-doped CQDs and mixed with lignin-based ACs under an optimized ratio, making the CQDs fully and uniformly distributed on the surface of highly porous AC matrix to form a 3D carbon composite with an interior surface decorated with CQDs. Instead of optimizing the inner porous structure, countless hydrophilic binding sites are created by CQDs on the stable AC matrix to provide abundant electroactive sites with excellent cyclability. In the novel design of carbon composites, superhydrophilic CD sites

are more attractive to ionic species and solvated electrolyte ions in aqueous medium, compared with the undecorated deep and branched micropores. Meanwhile, with CQDs evenly attached to the surface of ACs, more aqueous electrolytes can migrate and diffuse into the porous network, thus increasing contact with the electrodes. Accordingly, the CQDs significantly shorten ionic diffusion path, which leads to an efficient ionic diffusion and decreased mass transfer resistance. This research proposes a simple design to achieve high-performance SCs with a facile fabrication method. With the verification of characteristic measurements, we proved the effectiveness of this method and the feasibility of 3D carbon composite, which could also be applied in a variety of energy storage devices, such as carbon electrodes for EDLCs and ion-storage batteries and catalyst electrodes for fuel cell and photovoltaic cells.

Experimental section

Preparation of ACs and CQDs

The AC sample was made from commercial Kraft lignin. It was carbonized in a ceramic boat inserted in the alumina tube furnace with nitrogen flow at 700°C for one hour. After naturally cooling down with N_2 flow, the samples were pulverized by hand, grinding into small pieces, followed by ball-milling (PM100 RETSCH model), where the mill contained 2 and 10 mm stainless steel balls in a stainless steel container at 350 revolutions per minute for 45 min. After that, the ground carbon powders were separated by sieves from grinding balls and placed into the tube furnace for steam activation at 800°C for 0.5 h with a ramping rate of 10 °C min^{-1}. After steam activation, the sample was exposed to a CO_2 atmosphere for continuous physical activation at 800°C for 1 h to produce the final AC samples (shown in Figure 3.1). The CQDs are prepared by a solid-phase microwave-assisted method, heating the mixture of citric acid and urea at 280°C for five min according to our previous study.[109]

Materials characterization

The morphology and microstructure were observed by high-resolution transmission

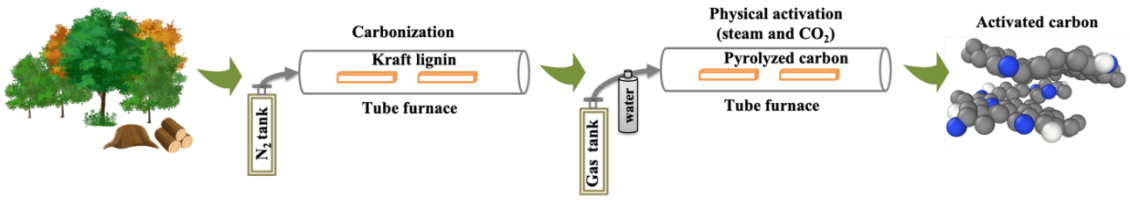

Figure 3.1 Preparation routine of ACs via carbonization of kraft lignin and two-step physical activation using steam and carbon dioxide as activation agents.

electron microscope (HR-TEM) (ZEISS, LIBRA 200) and scanning electron microscopy (SEM) Phenom ProX). The crystal structure of ACs and CQDs samples were characterized by X-ray diffraction (XRD) (Empyrean, Panalytical). The surface functional groups on the carbon composites were inspected and collected with a Fourier transform infrared (FTIR) spectrometer (Perkin Elmer, Llantrisant). The chemical compositions of samples were characterized on an X-ray photoelectron spectroscopy (XPS, Fison VG ESCA210). The contact angle was measured using Krüss FM40 shape analysis system (Hamburg, Germany). 2 μl water droplet was deposited on the substrate and the static time was 5 seconds. N_2 adsorption and desorption isotherms were obtained by TriStar 3000 volumetric adsorption analyzer (Micromeritics Instrument Corp.). SSAs and mesopore volume were determined from Brunauer-Emmett-Teller (BET) and Barrett-Joyner-Halenda (BJH) equations, respectively. The pore size distribution of the carbon samples was derived from density function theory (DFT) calculation.

Electrochemical performance evaluation

Electrochemical measurements of the ACs and CQDs electrodes were taken using a three-electrode configuration system with 2 M H_2SO_4 as the electrolyte solution. Pt wire served as the counter electrode and Ag/AgCl served as the reference electrode. The ACs and CQDs are uniformly mixed with Nafion and deionized (DI) water, and then dropped and coated on carbon paper with an area of 2 × 1 cm^2. The stainless steel foil was applied as the current collector. The cyclic voltammetry (CV) measurements of the electrodes were performed within the potential range between 0 and 1.0 V vs Ag/AgCl and the scan rates were set at 10, 30, 50, and 100 mV s^{-1}. The capacitances were measured by galvanostatic charge discharge (GCD) measurements within the voltage region of 0–1.0 V. The impedance spectra were carried out with frequency ranged from 100 kHz to 10 mHz. *Z*-view software simulated the impedance behavior based on Nyquist plot data.

Results and discussion

For clarification, the electrodes fabricated with mixed CQDs and ACs at a mass ratio of

1:1 and 1:2 are designated as CD@AC-11 and CD@AC-12, respectively. The HR-TEM micrograph of the prepared ACs is shown in Figure 3.2(a), which exhibits amorphous morphology with disordered carbon layers. The obtained CQDs with a uniform size distribution of 2–5 nm are shown in Figure 3.2(b). Clearly, the crystal lattice of a CD can be observed in the inset of Figure 3.2(b). After the CQDs are deposited on the surface of the ACs, CD domains with crystalline structure evenly distribute on the AC matrix in Figure 3.2(c). Selected-area electron diffraction (SAED) pattern, as shown in the inset of Figure 3.2(c), indicates the presence of bright diffraction rings and spots suggests that the CQDs consisted of nanocrystallites.

The SEM images of as-prepared electrodes with AC and CD@AC-11 on carbon paper are shown in Figure 3.3. We observe that the carbon paper is composed of a number of microscaled fibers with a random orientation. ACs fully covered the surface of the fibers, indicating that Nafion is an effective adhesion agent. As for CD@AC-11 electrode, it is obvious that CQDs are uniformly attached to the ACs, resulting in a high coverage of CQDs on the fibers.

The XRD pattern of AC, as illustrated in Figure 3.4(a), shows a broad lump located at ~24°, corresponding to the characteristic (002) diffraction peak of carbons. The dispersive and broad peak indicates the amorphous structure of carbon with large interlayer spacing distance ($d_{(002)}$= 0.370 nm). The (002) peak of CD located at ~27° shows much sharper, implying the presence of well-crystallized structure. The intensity of the peak in CD@AC-11 sample is higher than that of AC, which indicates a higher crystallinity than amorphous AC. Interestingly, the small twin-peak could be observed in the enlarged image, commonly ascribed to the interlayer stacking reflections.[109, 115] The peak location shifts right, compared to the AC peak, indicating the interlayer spacing distance decreases from 0.370 to 0.330 nm due to the coverage of CQDs on the surface of ACs. The small sharp peak (2 theta: ~30°) in AC and CD@AC-11 sample originates from the presence of iron oxide coming from the ball-milling of the carbonized lignin.[116, 117]

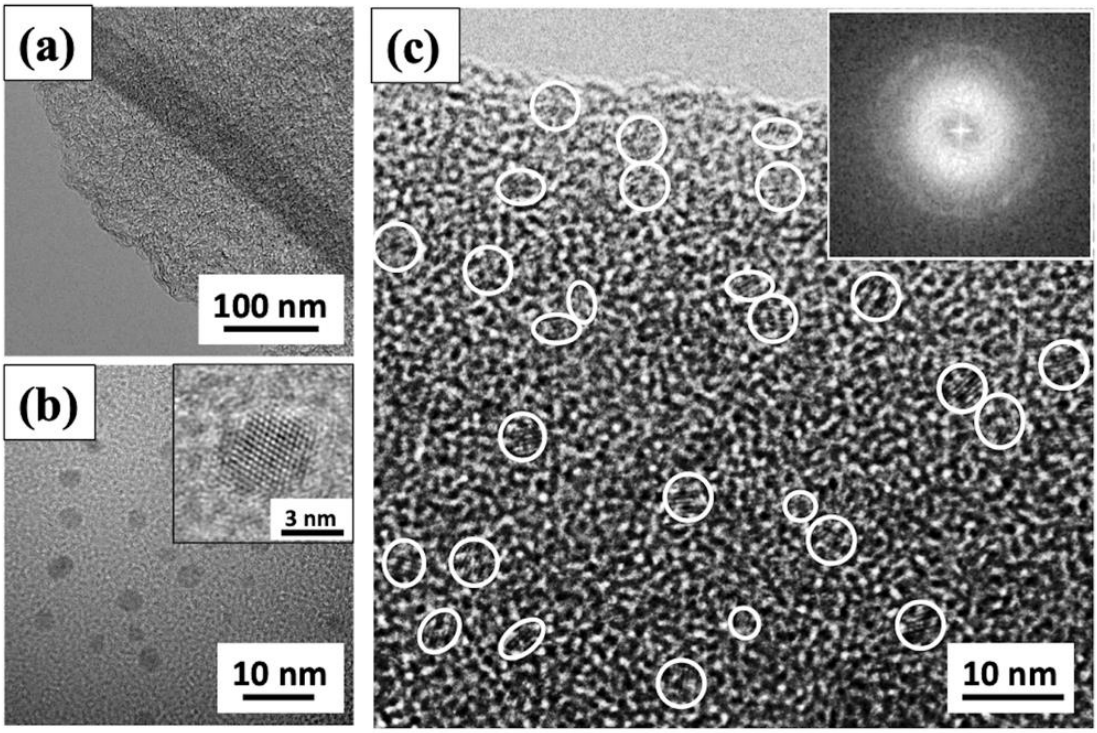

Figure 3.2 HR-TEM micrographs of (a) ACs, (b) CQDs, and (c) CD@AC-11 samples. The insets of Figures 3.2(b) and 3.2(c) show well-ordered lattice fringes of a diffraction pattern of an individual CD within the selected-area, respectively.

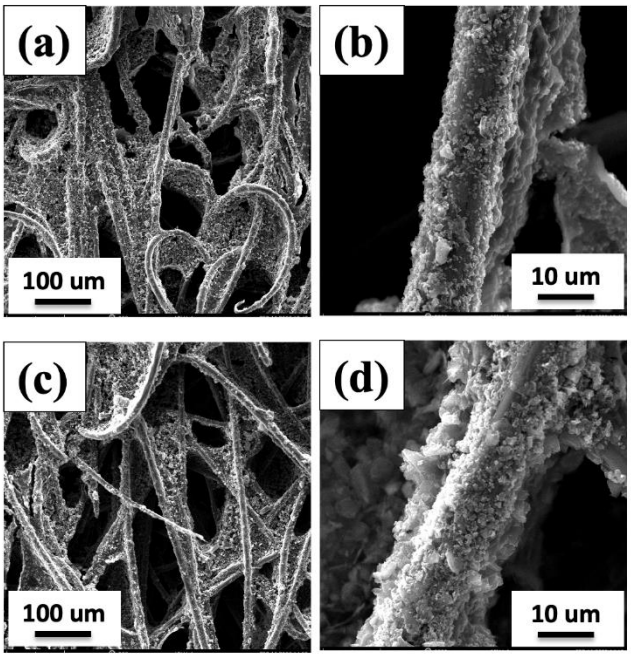

Figure 3.3 SEM images of (a, b) AC and (c, d) CD@AC-11 carbon paper electrodes with low and high magnification.

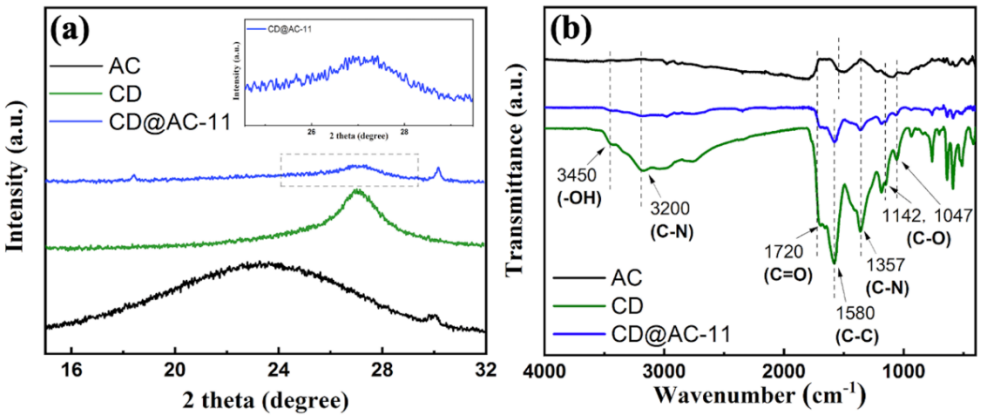

Figure 3.4 (a) XRD patterns and (b) FTIR spectra of AC, CD and CD@AC-11 samples.

Figure 3.4(b) illustrates the FTIR spectra of AC, CD, and CD@AC-11. In the CD spectrum, the valley at 1580 cm^{-1} corresponds to the C–C stretching in the transmission spectrum, whereas C–O groups appear at 1142 and 1047 cm^{-1}. The bands at 3450 cm^{-1} and 1720 cm^{-1} correspond to hydroxyl (-OH) and carbonyl (C=O) groups, respectively. Strong bands at 1357 and 3200 cm^{-1} provide evidence of C-N groups, confirming N-functionalized CQDs.[104, 118-120] It is worth noting that CD@AC-11 shows a similar spectrum with CD, indicating that functional CQDs are uniformly covered on the AC surface. Besides the enhanced absorption from C=O and C–O groups, it is apparent that abundant C–N groups are introduced since the CQDs possesses a high amidation level due to N-dopants and N-functionalities. This is further confirmed by XPS measurement, which is shown in Figure 3.5(a). The presence of N 1s peak in CD@AC-11 sample proves the introduction of CQDs leads to more C-N functional groups. The high-resolution XPS spectra of N 1s peak of CD@AC-11 is shown in Figure 3.5(b). The N 1s peak was deconvoluted into three peaks centered at 399.7 eV (pyrrolic/pyridinic N), 400.4 eV (graphitic N) and 401.7 eV (O=C-N), respectively.[109, 121] Usually the first component represents the aromatic C=N-C, the graphitic N refers to the N bonded with three sp^2 carbon atoms, and the last one is amino group.[109] In our case, the graphitic and amino N are predominant since they take 31.9% and 56.4% of the total integration area, respectively. The C 1s spectra of AC (Figure 3.5(c)) were decomposed into 4 peaks and represent the C=C or C-C (*ca.* 284.6 eV), C-O (*ca.* 286.5 eV), C=O (*ca.* 288.5 eV) and O-C=O (*ca.* 289.5 eV), respectively.[100] This can be attibuted to the existence of oxide functional groups attached to the edge and surface of ACs as well as the CQDs. While for CD@AC-11, one more peak centered at 285.2 eV refers to the presence of C-N (Figure 3.5(d)).[95, 97] To further verify the result, we also conducted the CHNS-type elemental analysis. The N/C ratio of CD@AC-11 sample is increased up to 16.1%, much higher than that of AC (i.e., 3.8%). This enhanced N/C ratio is attributed to the fact that CQDs contain a high N/C ratio (*ca*. 45.6%). Accordingly, this result agrees with FTIR and XPS analysis, revealing that more N-containing functional groups are introduced onto the surface of porous structure of ACs.

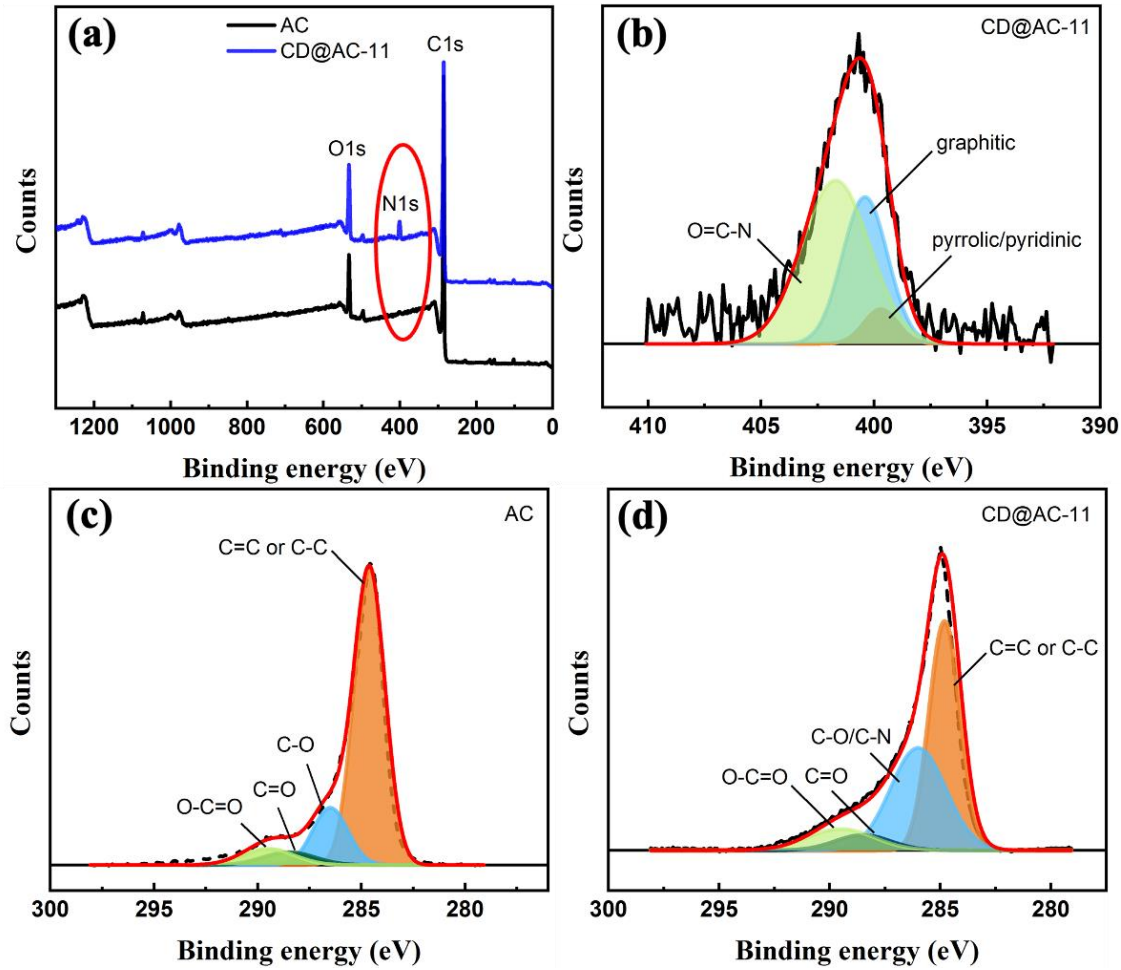

Figure 3.5 (a) Survey-scan XPS spectra of AC and CD@AC-11 samples, (b) N 1s peak of AC@AC-11 sample, C 1s peak deconvoluted by a multiple Gaussian function: (c) AC and (d) CD@AC-11 samples.

The electrochemical measurements were conducted using a three-electrode system in 2 M H_2SO_4 aqueous electrolyte to verify the performance of the as-fabricated electrodes. Figure 3.6 shows typical CV curves of SCs fabricated with AC, CD@AC-11 and CD@AC-12. It is obvious that the CV curves of pristine AC electrode (see Figure 3.6(a)) show a pair of redox peaks, possibly originating from faradaic reactions occurring on the electric double-layer due to heteroatoms (N, H and O) derived from precursors and trace iron oxide in the lignin-based AC.[90, 91] The CV profiles of CD@AC-11, as shown in Figure 3.6(b), exhibit near rectangular shapes that contains multiple redox peaks, indicating the coexistence of two different energy-storage mechanisms, i.e., electric double-layer formation and faradaic redox reaction.[121] The relatively rectangular shape of the curves and increased area stems from the electric double-layer behavior. The introduction of various functional groups leads to the obviously increased amount of hydrophilic polar sites, significantly enhancing the affinity towards aqueous electrolyte and providing more accessible surface area to ions. In the ideal formation of carbon electric double layer with acid electrolyte, the charge and discharge process of carbon electrodes could be expressed as equation (R1):[122, 123]

$$C^* + H^+ \leftrightarrow C^*//H^+ \quad \text{(R1)}$$

where the carbon electrode is presented as C*, the proton of the acidic electrolyte as H^+, and the double layer where charges accumulated separately on the two // sides. It is simply physical adsorption process forced by the electrostatic forces between carbons and protons. In our case, besides porous carbons, abundant surface oxygen and nitrogen functional groups provide more available adsorption and desorption sites. The equilibrium reactions occurred are presented as (R2) and (R3): [87, 92, 122, 124]

$$C_xO^* + H^+ \leftrightarrow C_xO^*//H^+ \quad \text{(R2)}$$

$$C_xN^* + H^+ \leftrightarrow C_xN^*//H^+ \quad \text{(R3)}$$

Where the C_xO^* and C_xN^* represent oxygen-containing (e.g., carbonyl and quinone groups) and nitrogen-containing functional groups (e.g., amino, quaternary and pyrrolic/pyridinic N groups). Herein $C_xO^*//H^+$ and $C_xN^*//H^+$ represent the electric double layer with charges accumulated on the sides due to the ion-dipole attraction, which is different with charges

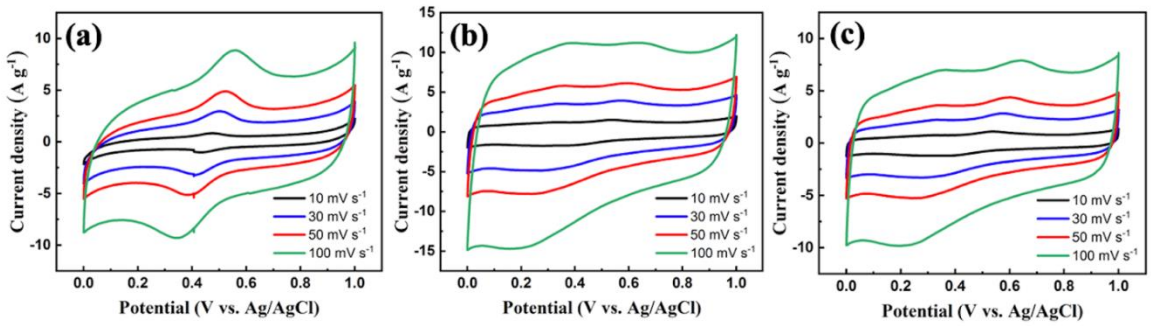

Figure 3.6 CV curves of (a) AC, (b) CD@AC-11, and (c) CD@AC-12 electrodes at different scan rates.

accumulated on the sides due to the ion-dipole attraction, which is different with electrostatic forces between carbons and protons. The increased electric double layer behaviors are partially derived from the enhanced dipole-dipole interactions.

For confirmation, we conducted contact angles measurements to directly examine the hydrophilicity of the electrodes. As shown in Figure 3.7, the results confirm our speculation that the CD electrode shows super hydrophilic behavior with the contact angle of 42°. With the help of CQDs decoration, the contact angle exhibits an obvious decrease from 107° to 75°, which clearly demonstrates that the addition of CQDs greatly improves the hydrophilicity of the electrodes and thus enhances the surface affinity towards aqueous electrolyte. This result further proves the feasibility of (R2) and (R3).

The presence of nitrogen and oxygen functional groups contribute improvement to the electric double layer capacitance and the pseudo capacitance, as evidenced by the redox peaks. We hypothesize that the N functional groups significantly improve the electrochemical reactivity due to their electron-donor properties. Specifically, negatively charged pyridinic/pyrrolic N atoms provide electroactive sites and facilitate the possible redox reactions. The simplified reaction equation is expressed as (R4):[91, 95, 124-126]

$$C_xN^* + H^+ + e^- \leftrightarrow C_xNH^- \quad \text{(R4)}$$

where the C_xN^* represents pyridinic/pyrrolic N groups. In addition, the oxygen functional groups with electron-acceptor properties, such as carbonyl and quinone groups, may also induce the redox reactions during the electron transfer process, which is expressed as (R5):[122]

$$C_xO^* + H^+ + e^- \leftrightarrow C_xOH \quad \text{(R5)}$$

where C_xO^* represents carbonyl and quinone groups, and e^- represents electron.

The CV curves of CD@AC-12 in Figure 3.6(c) further prove the above speculation. When the CQDs were added into ACs with the ratio of 1:2, the encircled rectangular area is a

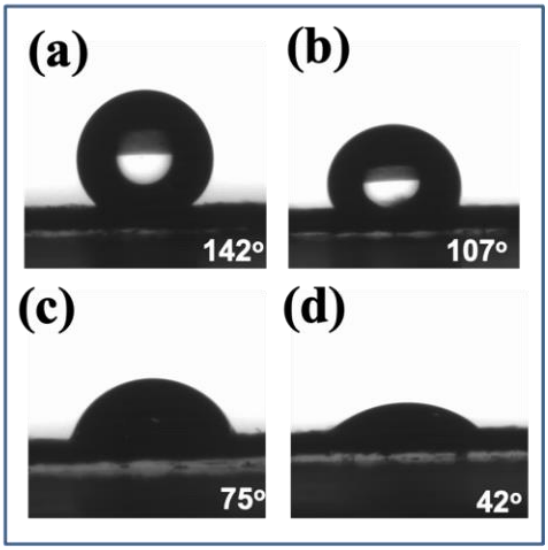

Figure 3.7 Optical images of water droplets on (a) carbon paper, (b) AC electrode, (c) CD@AC-11 electrode, and (d) CD electrode.

decreasing trend with the faradaic peak. It demonstrates that the capacitance, resulting from electric double layer behavior and faradaic reaction, is significantly enhanced by the amount of CQDs addition. As a result, an appropriate amount of CD additive plays a crucial role in enhancing the specific capacitance of SCs.

The GCD measurements were carried out in the potential window of 0–1 V and at a current density of 0.25 A g^{-1}. As shown in Figure 3.8(a), it should be noticed that the charging and discharging times gradually increase with the amount of the CD addition. The specific capacitance calculated based on the GCD results at various current densities are shown in Figure 3.8(b). The capacitance of CD@AC-11 electrode reaches as high as 301.7 F g^{-1} at 0.15 A g^{-1}, which is twofold higher than that of AC one (i.e., 125.8 F g^{-1}). This is consistent with previous CV measurements, revealing the effectiveness of CQDs addition on the enhanced capacitance. As the specific capacitance of CD@AC-12 achieves 191.8 F g^{-1}, there is *ca*. 52% increase achieved through adding half-amount CQDs, confirming that the enhanced capacitance is proportional to the CD content in this range. Although the capacitance decreases with current density for all electrodes, the introduction of CQDs still takes the effect as the doubled capacitance of AC even at high current densities, e.g., 20 A g^{-1}.

The cyclic stability is also a key point to evaluate the performance of SCs. As shown in Figure 3.8(c), the cyclic performance of as-prepared electrodes was conducted at a current density of 15 A g^{-1}. After 3000 continuous cycles, all SC devices exhibit stable capacitance with excellent coulombic efficiency (> 99.5%). All SC enables high capacitance retention with above 85% of the initial capacitance. Finally, the Ragone plots of the SCs with as-prepared electrodes are given in Figure 3.8(d). The energy density and power density were calculated based on the following equations:[127, 128]

$$E = \frac{C(\Delta V)^2}{2} \quad \text{(R6)}$$

$$P = \frac{E}{\Delta t} \quad \text{(R7)}$$

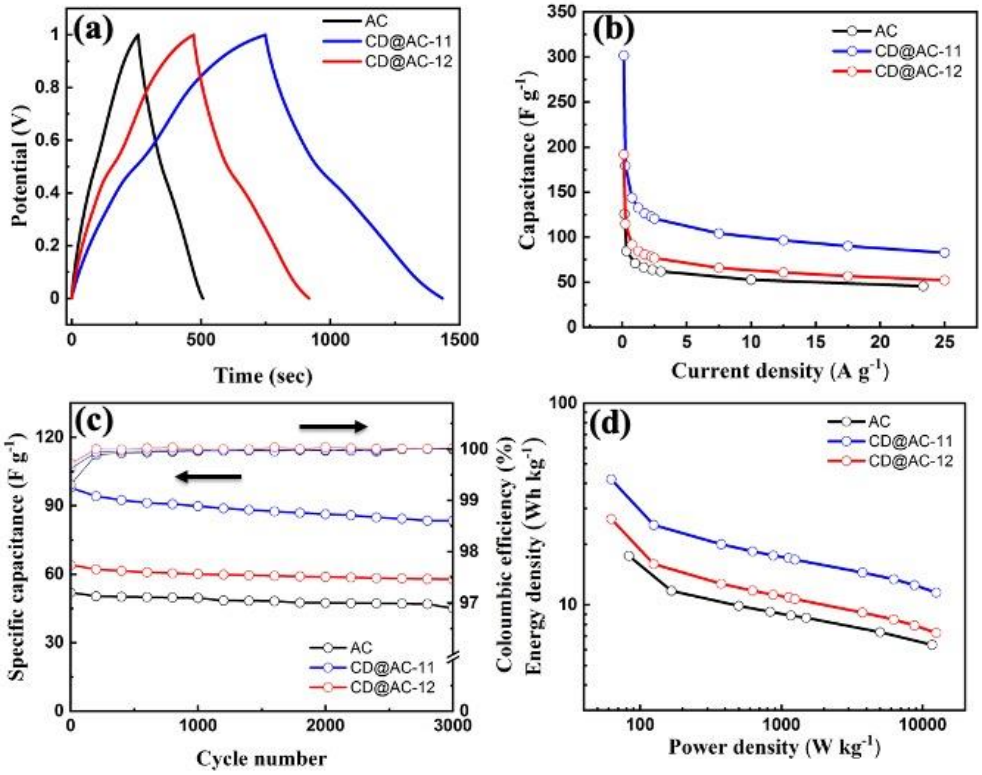

Figure 3.8 (a) GCD curves charged and discharged at 0.25 A g^{-1}, (b) variation of specific capacitance of electrodes with current densities, (c) cyclic performance of as-prepared electrodes at a current density of 15 A g^{-1} for 3000 cycles, and (d) Ragone plot of the SCs with as-prepared electrodes.

Where E is the specific energy density (Wh kg^{-1}), C is the specific capacitance (F g^{-1}), ΔV (V) stands for the potential window, P is the specific power density (W kg^{-1}) and Δt (s) is discharge time. The AC-based SC delivers an energy density of 18 Wh kg^{-1} at power density of 83 W kg^{-1} and the energy density of 6 Wh kg^{-1} can be delivered at 11667 W kg^{-1}. In contrast, the energy density of the CD@AC-11 electrode can reach as high as 42 Wh kg^{-1} at 63 W kg^{-1} and even at high power density of 12500 W kg^{-1}, the energy density of 11 Wh kg^{-1} still can be released. At the same power density, the energy density of CD@AC-11 electrode achieves double that of AC one. Again, the addition of CD benefits the performance of SCs including the enhanced capacitance and superior cyclic stability.

To further check the ionic transportation and electronic conductivity of as-fabricated SCs, we applied the EIS experiments before and after potential cycling (i.e., GCD 3000 cycles). The Nyquist plots of SCs in the frequency range of 100 kHz to 10 mHz are presented in Figure 3.9. Usually, the diameter of the semicircle in the high frequency region can be inferred from the charge transfer resistance. An equivalent circuit is proposed in Figure 3.9(d) to predict the impedance behavior from 100 kHz to 50 Hz. The equivalent circuit mainly contains the following elements: the resistance comes from the electrolyte solution (R_E), the interfacial resistance (R_B) and capacitance (C_B) which results from the impedance between carbon electrodes and current collectors, the double-layer capacitance (C_{dl}), and charge transfer resistance (R_{CT}). The overall resistance, including R_E, R_B, and R_{CT}, represents the equivalent series resistance (R_{ES}).[100] The calculated results, analyzed by *Z*-view software, are shown in Table 3.1. We observe that the R_E only takes a very small contribution to the overall resistance and all R_E values are similar among the electrodes. The R_B values of the CD@AC-11 and CD@AC-12 are slightly higher than that of AC sample indicating that the influence of CD additive on the interfacial resistance is insignificant. However, the R_{CT}, which acts as a major contributor to R_{ES}, is apparently decreased after adding the CD additive into AC electrode. The R_{ES} of the CD@AC-11 is approximately 50% smaller than that of AC, indicating that the introduction of CQDs strongly decreases the overall inner resistance of AC - based electrode. The improved

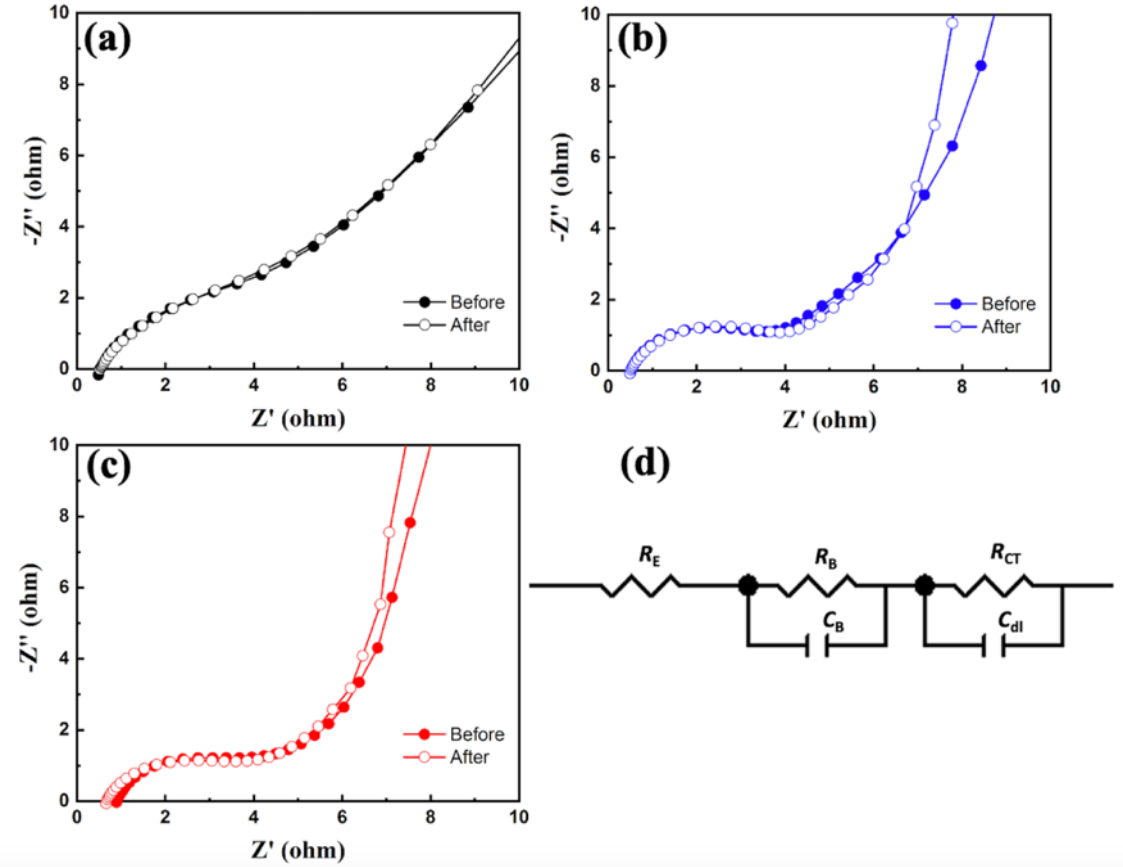

Figure 3.9 Nyquist plots of SCs fabricated with (a) AC, (b) CD@AC-11, and (c) CD@AC-12 electrodes, and (d) the proposed equivalent circuit for describing the impedance behavior.

Table 3.1 Calculated equivalent resistance values in high frequency region and diffusion coefficients of H^+ ions in SCs.

Electrode	R_E (Ω)	R_B (Ω)	R_{CT} (Ω)	R_{ES} (Ω)	D (cm^2 s^{-1})
Before cycling					
AC	0.50	1.11	8.16	9.77	1.34×10^{-12}
CD@AC-11	0.56	1.86	2.18	4.60	1.64×10^{-11}
CD@AC-12	0.52	2.09	2.59	5.66	1.21×10^{-11}
After cycling					
AC	0.51	1.13	8.17	9.81	2.41×10^{-12}
CD@AC-11	0.55	1.19	2.45	4.19	1.05×10^{-10}
CD@AC-12	0.54	1.55	2.28	4.57	6.14×10^{-11}

electrochemical impedance can be attributed to the fact that higher surface coverage provided by the CQDs facilitates a rapid double-layer formation and smooth charge transfer, thus decreasing the overall resistance. After cycling, the R_{ES} of AC electrode keeps an identical value, while the R_{ES} values of CD@AC-11 and CD@AC-12 electrodes display a slightly decrease, proving the presence of robust carbon framework. Since there is no decay after thousands of cycling process, this result confirms satisfactory cyclic stability of the devices.

In the low frequency range, the slope of the linear line suggests that the electrochemical impedance was dominated by ionic diffusion. The larger of the slope, the lower of the resistance is achieved.[129] Accordingly, the ionic diffusion coefficient could be calculated based on the following equation:[100, 130]

$$k_w = \frac{RT}{n^2F^2A\sqrt{2}}\left(\frac{1}{D^{1/2}C^*}\right) \quad \text{(R8)}$$

where k_w can be obtained by the slope of the line, D value reflects that the diffusivity of H^+ ions in electrodes. All other parameters in this equation are known values, where n is the charge-transfer number, A is the electrode surface area, and C^* is the ionic concentration.[100] The calculated D values are also shown in Table 3.1. Before cycling, the ionic diffusion coefficient for the CD@AC-11 shows 12.2 times higher than that of the pristine AC. The enhanced ionic diffusion coefficient is observed because the hydrophilic CQDs make it easier for the ions and hydration molecules to access the interior carbon framework (i.e., shorter diffusion path and higher hydrophilic surface coverage). After cycling, the ionic diffusion coefficient for the CD@AC-11 electrode is enhanced by 25.5 times as compared to that of pristine AC one. This finding mainly originates from a synergistic effect that combines hydrophilic sites (from CQDs) and lateral interaction with dipole moments of hydration molecules, leading to higher wetted surface area by electrolyte wetting, i.e., reaching a complete wetting after an appropriate period. In other words, after thousands of charging and discharging processes, the CD@AC-11 electrode are completely wetted, making high pore accessibility for ionic transportation. Accordingly, the improved D value

of CD@AC-11 confirms that the existence of functionalized binding sites enables the creation of more accessible SSAs and shortens the ionic diffusion path.

On the basis of experimental results, the role of CD additive in enhancing the specific capacitance of highly porous AC electrodes requires an in-depth investigation. First, the existence of the CQDs imparts a surface polarity, which greatly improves the wettability of the internal nanostructures of porous carbon electrodes. As shown in Figure 3.10(a), it is generally recognized that AC possesses a well-developed porous structure, consisting of mesopores (pore size: 2–50 nm) and micropores (pore size: < 2 nm). Thus, the deep and branched micropores restrict the ion movement, resulting in a long ionic diffusion pathway during the charging process.[94] With the well-distributed CQDs on the surface, more ions are favorably accessible to the inner pores, thus enhancing the wettability of the AC electrodes. Second, a large amount of hydrophilic polar sites exist, thus creating more accessible surface area. As shown in Figure 3.10(b), with aid of the robust and stable AC matrix, the nanosized CQDs (average particle size: 2–5 nm) can be evenly deposited on the surface or into the porous structure, generating a large number of CD binding sites.

However, the CD deposits inside the pore channels possibly hinder ionic diffusion at the entrance of micropores, as illustrated in Figure 3.10(b). Table 3.2 shows surface characteristics of pristine and CD@AC-11 composite including BET surface area, total pore volume, and pore size distribution, determined by nitrogen physisorption at -196°C. We observe that pristine AC is mainly microporous, whereas the micropore fraction is decreased by the introduction of CQDs. Figures 3.11(a) and 3.11(b) show the DFT pore size distributions of different carbons, indicating that the pore size distribution could be controlled by the addition of CQDs in the carbon composites. It is of interest that both the specific capacitance and diffusion coefficient are significantly enhanced by an increase in mesopore fraction of the carbon composites. This demonstrates that the above postulation (see Figure 3.10) is successfully established. This result reveals that the entrance of micropore channels is partly occupied by the CQDs. Fortunately, the mesopore channel is

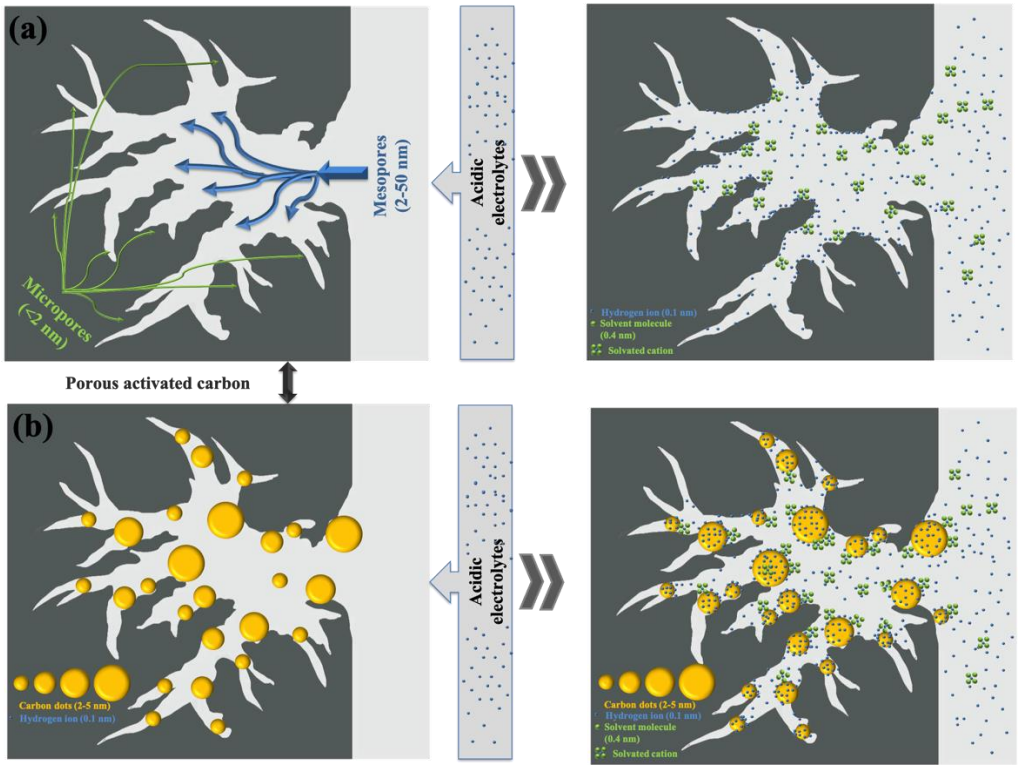

Figure 3.10 Schematic illustrations of charging process in (a) AC and (b) CD@AC-11 electrodes.

Table 3.2 Pore characteristics of AC, CD@AC-11 samples determined from N_2 physisorption at -196°C.

Carbon sample	S_{BET} [1] (m^2g^{-1})	V_T [2] (cm^3g^{-1})	X_{micro} [3] (%)	X_{meso} [4] (%)
AC	591.7	0.34	77.1	22.9
CD@AC-11	299.0	0.11	67.7	32.3

Remark:

[1] S_{BET}: Surface area determined from Brunauer-Emmett-Teller (BET) equation.

[2] V_T: Total pore volume determined from single-point adsorption volume at p/p_0 ~0.98.

[3] X_{meso}: Mesopore fraction determined from the ratio of S_{BET} to Barrett-Joyner-Halenda (BJH) surface area.

[4] X_{micro}: Micropore fraction determined by subtracting BJH surface area from S_{BET}.

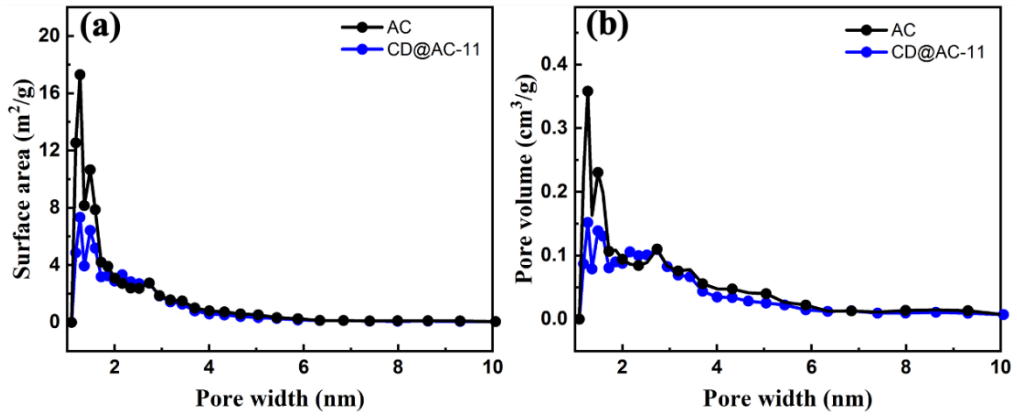

Figure 3.11 (a, b) DFT pore size distributions of AC and CD@AC-11 samples.

still open accessible for ions or hydration molecules during charge/discharge process. Meanwhile, the AC can be considered as a robust matrix that provides a well-developed porous framework bearing well-dispersed CQDs. The CQDs not only improve the ionic diffusion pathway but also offer a large number of hydrophilic sites (i.e., high surface coverage of accessible surface area for electrolyte wetting), enabling the enhanced capacitance. Thus, this structural CD@AC design can be utilized for engineering desired pore structure and micropore/mesopore fraction within the AC electrodes.

Conclusions

In summary, we achieved superior performance of SCs with the well-distributed CQDs decorating the surface of AC matrix. The introduction of hydrophilic CQDs not only improved the wettability of electrodes, but also created electroactive sites. The capacitance was greatly improved from 125.8 F g^{-1} to 301.7 F g^{-1} due to the enlarged effective surface area and enhanced electrochemical activity without sacrificing the high cyclability. With the existence of abundant polar sites, ions are attracted to and accumulate around the CQDs, therefore shortening ionic diffusion paths and decreasing the inner resistance. Our work indicates that the CQDs could be well dispersed on the carbon matrix and the effective surface area could be significantly improved *via* creating numberless functionalized CD sites, resulting in the enhanced electric double layer capacitance as well as pseudo capacitance. The unique carbon composite can be utilized for engineering desired pore structure and micropore/mesopore fraction within the AC electrodes. This design of a decorated carbon framework possesses great potential for developing promising energy storage devices in the near future.

Chapter 4 Tailored Mesoporous Structures of Lignin-Derived Nano-Carbons for Multiple Applications

A version of this chapter is prepared for publication by Yu, L., Liang L., Keffer, D.J., Ivanov, I.N., Chen, H., Dai S., Ragauskas A.J.,Harper, D.P.:

Yu, L., Liang L., Keffer, D.J., Ivanov, I.N., Chen, H., Dai S., Ragauskas A.J., Harper, D.P., Tailored Mesoporous Structures of Lignin-Derived Nano-Carbons for Multiple Applications.

Credit authorship contribution statement:
Conceptualization, LY, DH; methodology, LY, LL, II, DK, SD, RA, DH; validation, LY, LL, HC; formal analysis, LY, LL; resources, DK, SD, RA, DH; writing—original draft preparation, LY, LL; writing—review and editing, II, DK, HC, SD, RA, DH; visualization, LY; supervision, DH, DK, SD, RA; project administration, DH; funding acquisition, DH, SD, RA.

Abstract

This work utilizes a one step KOH activation for lignin precursors to produce ultra-high mesoporous activated carbons (ACs) with surface area of 3,207 m^2 g^{-1} and mesopore ratio of 76%. The produced ACs are applied for supercapacitors (SCs) as well as methylene blue (MB) adsorption. The capacitance of the SCs reaches as high as 812.3 F g^{-1} with the ultra-high energy density of 112.8 Wh kg^{-1}. It also exhibits excellent maximum adsorption capacity of 1,250 mg g^{-1} of MB adsorption. By modifying the process conditions, the mesopore ratio of ACs could be controlled from from 10% to 80%. The influence of one-step and two-step KOH activation on the surface properties of lignin-based activated carbons was also investigated. Compared with one-step activation, traditional two-step method produced porous carbons with a lower surface area of 1,227 m^2 g^{-1} and a high micropore ratio of 73%. Although it has limited surface area, the higher oxygen ratio and surface functionalities greatly improve its performance. The capacitance of SCs reaches 405.2 F g^{-1} and power density of 5,882.4 W kg^{-1}. The maximum MB adsorption capacity of this sample is 476.19 mg g^{-1}.

Introduction

As one of the three main components of lignocellulosic biomass plant cell wall, lignin is the most abundant aromatic polymer in nature. In practice, as a waste stream of paper and pulp industry, millions of tons of lignin are produced annually.[44] The majority of this lignin is burned onsite for power generation, which is low efficiency and leads to environmental pollution. Many researchers are working on converting lignin into high value products due to aromatic structure.[131, 132] The high carbon content of lignin makes it an ideal precursor for a variety of carbon products, including carbon fibers, chemicals, activated carbons, and so on.

The demand for activated carbons (ACs) is rapidly increasing as their diverse applications, ranging from energy storage devices to environmental purification.[133] Benefiting from their high surface, stability, low cost and abundance, ACs are commonly used as electrode materials for supercapacitors. The well-developed porous structure and abundant surface functionalities of ACs also enable enhanced adsorption of organic adsorbates as well as heavy metal ions, thus making it widely applied for water purification.[133, 134] ACs are produced after physical or chemical activation from various carbon rich precursors, including petroleum pitch, coal, and coconut.[134] Traditionally, ACs are produced via two-step (carbonization and activation) process.[135] During carbonization, the precursor is converted to carbonaceous char. Porosity is created during the activation process.[135, 136] Physical activation (CO_2, steam) is widely used for preparing the commercial scale used ACs as this process is safe, low cost and avoids corrosive effects of the production facilities. Limited by the surface area of physical activated carbons, chemical activations are conducted to produce ACs with higher surface areas.[135] Various activation agents, including potassium hydroxide (KOH),[137-139] sodium hydroxide (NaOH),[140] zinc chloride ($ZnCl_2$),[141] phosphoric acid (H_3PO_4),[142] and sodium carbonate (Na_2CO_3)[143] have been widely used for synthesize ACs.[135] Among these, potassium hydroxide (KOH) is reported to be the most powerful agents, while the salt activation agents produced ACs have lower surface area.[135]

As one of the most important applications of ACs, supercapacitors have attracted enormous attention. There is urgent need for development of energy storage devices as the power generated by renewable power plants need to be stored for better use. Due to the high cost of RuO_2 and instabilities of the most transition-metal compounds electrodes, ACs are widely used for commercial scaled SCs. Based on the energy storage mechanism behind SCs, they are typically classified as electric double layer capacitors (EDLCs) and faradaic pseudo capacitors.[144] EDLCs are the main process for ACs to produce capacitance. The simple reversible adsorption and desorption process results in the high power density and stability For EDLCs. However, the relatively low energy density of EDLCs limited their practical applications.

In this work, we adopted KOH as activation agent and conducted updated one-step as well as traditional two-step chemical activation to produce lignin based ACs with ultrahigh surface area and tailored porous structures. The one-step and two-step activation were optimized and investigated to elucidate the effects of activation process on the surface properties of ACs. The produced ACs were applied for supercapacitors with ultrahigh energy density. Methylene blue adsorption was also conducted to assess the performance for environmental applications.

Experimental section

Preparation of lignin-derived activated carbons

In this work, we prepared High surface area Activated Carbons (HACs) via one-step and two-step processes. We use the nomenclature HAC-1 and HAC-2 for an activated carbon produced via the one-step and two-step processes respectively. For two-step produced ACs, Kraft softwood (KSW) lignin were carbonized at N_2 atmosphere (~2.5 L min^{-1}) in a stainless steel tube furnace at 1000 °C for 1 h. The carbonized samples were grinded by ball-milling (PM100 RETSCH model) and separated from the grinding balls with sieves to obtain the carbonized char. The carbonized char was mixed with KOH at mass ratios of 1:3 and 1:4, respectively, and placed into the tube furnace for chemical activation in N_2

environment at 700/800/900 °C for 0.5 hr. As for one-step produced ACs, the KSW lignin was directly mixed with KOH at mass ratio of 1:3 and 1:4, and processed in tube furnace for chemical activation. After activation, the carbon sample were washed with deionized water, and then oven-dried at 105 ℃ for 2 hrs. For both processes, a variety of processing conditions were explored. The material labeled HAC-1 was produced under the optimal processing conditions with a temperature of 800 ℃, a lignin to KOH ratio of 1:4 and a processing time of 2 hrs. For HAC-2, produced from the two-step method, the same optimal processing conditions of 800 ℃, a lignin to KOH ratio of 1:4 and a processing time of 2 hrs were used.

Materials characterization

Gel permeation chromatography (GPC) analysis was used to determine the molecular weight (Mw, Mn) and molar-mass dispersity ($Đ_M$) index of the lignin samples. ^{31}P-NMR measurements were conducted with a Varian 400-MR spectrometer. Two-dimensional (2D) ^{1}H–^{13}C NMR spectra were conducted on a Bruker Avance III 500-Hz NMR spectrometer. The morphology of ACs were characterized by scanning electron microscopy (SEM, Zeiss EVO). The surface functionalities of ACs were analyzed via X-ray photoelectron spectroscopy (XPS, Fison VG ESCA210) measurement. CHN elemental analysis was performed by combustion analysis (Perkin Elmer). The surface characteristics were obtained by TriStar 3000 volumetric adsorption analyzer (Micromeritics Instrument Co.). Detailed procedures were provided in the experimental section of Chapter 2. Raman spectroscopy was conducted with a 785 nm laser (Renishaw, 50% power). The samples were scanned within the range of 300 – 3200 cm^{-1}.

Electrochemical performance tests

Slurries were blended with activated carbons (94.0 wt%), polyvinylidene fluoride (5.0 wt%, Kynar) and black carbon (1.0 wt%, Super C65) in N-methyl-2-pyrrolidone (NMP) solvent. The electrodes were prepared by coating the slurry on stainless-steel substrates (2 × 1 cm^2). Electrochemical performance of prepared electrodes was tested using a three-

electrode system with the H_2SO_4 solution as the electrolyte (1 M). The impedance spectra were with frequency ranged from 100 kHz to 1 mHz.

Adsorption of methylene blue dye

10 mg activated carbons were added into 10 mL MB solution with different MB concentrations (500 – 2000 mg L^{-1}). The mixed solutions were shaken on an incubator at room temperature for 48 h to reach equilibrium. Then the mixtures were centrifuged at 10000 rpm for 5 min. The upper supernatant was collected for adsorption measurements via UV-vis Spectroscopy (Shimadzu Corporation) at 660 nm. MB standard calibration curve was developed from a series of known MB dye solutions. The dye adsorption capacity was calculated using the following equation:

$$q_e = \frac{(C_0 - C_e)V}{m} \quad (1)$$

where C_0 is the initial MB concentration (mg L^{-1}), C_e is the MB concentration at equilibrium (mg L^{-1}), m is the weight of the used activated carbons (g), V is the solution volume.

Results and discussion

The results are organized into four sections: (i) chemical characterization of the lignin feedstock, (ii) structural and chemical characterization of the activated carbons, (iii) electrochemical performance and (iv) methylene blue adsorption performance.

Characteristics of the lignin feedstock

The feedstock used in this study is kraft softwood (KSW) lignin. The composition and elemental analysis are shown in Table 4.1. KSW lignin has high purity (95.96%). The ash content (3.86%) usually refers to the inorganic and mineral contents that come from biomass, which is highly related to the biomass and isolation methods.[145] The polydispersity of the molecular weight is about 2 for KSW lignin, indicating uniformity of molecular weight distribution. The presence of sulfur in KSW is a result of the use of sulfuric acid in the kraft pulping process.

Table 4.1 Composition, GPC and elemental analysis of KSW lignin.

Purity analysis (%)		Molecular weight			Elemental analysis (%)				
ASL[a] + AIL[b]	Ash	Mn	Mw	Molar-mass dispersity	C	H	N	S	O
95.96	3.86	1705	3577	2.098	62.07	5.64	0.44	1.65	30.20

[a] Acid-soluble lignin. [b] Acid-insoluble lignin.

The monomer distribution of lignin is highly related to the plant species and isolation methods. Moreover, the monomer distribution impacts the structure of the resulting carbonized char.[146] To examine the chemical structure and monomer distribution of the KSW lignin used in this work, 2D ^{13}C-^{1}H NMR was conducted. The aromatic region (6.0-8.0 ppm/100-140 ppm) is shown in Figure 4.1(a). For the KSW lignin, it mainly contains guaiacyl (G) unit (~78.2%) and H monomer (~21.8%). In the aliphatic region (2.5-6.0 ppm/50-100 ppm), it can be observed in Figure 4.1 (b) that the linkages of KSW lignin are dominated by methoxyl (OMe) and γ-hydroxylated (A_γ) groups, with a small amount of β-5′ phenylcoumaran (B_γ and B_β) groups.

The presence of functional groups in the lignin also impacts the chemical composition of the resulting carbonized char. FTIR spectra of KSW lignin was obtained and shown in Figure 4.2, the broad peak around 3300 cm^{-1} corresponds to the stretch vibrations of phenolic and aliphatic O-H groups. The peaks around 1600, 1510 and 1440 cm^{-1} are assigned to the -C=C aromatic stretching vibrations.[147] The bands around 1260 and 1210 cm^{-1} are associated with the C-C, C-O and C=O stretching of G units.[148] The peaks around 1130 and 1030 should be attributed to the C-O stretching in ester methoxy groups and β-O-4 links.[148]

Hydroxyl groups are crucial to the thermal properties of lignin and ^{31}P NMR (shown in Figure 4.3) was applied for characterizing the hydroxyl groups and the quantitative results are shown in Table 4.2. The significant peak at a chemical shift of 6.29 corresponds to the guaiacyl OH groups. The ^{31}P NMR results are also consistent with the 2D NMR, which returned a monomer distribution about 78% guaiacyl.

Characterization of lignin produced activated carbons

BET surface areas and porous structures

One- and two-step activation are processed under various conditions and the surface areas and mesopore distributions of the produced samples are shown in Figure 4.4. It can be

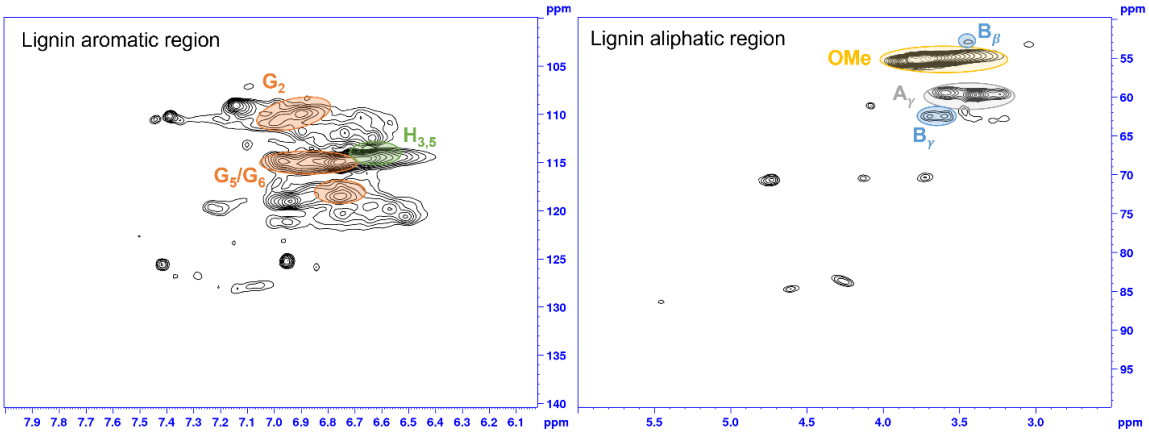

Figure 4.1 2D ^{13}C-^{1}H NMR spectra for KSW lignin.

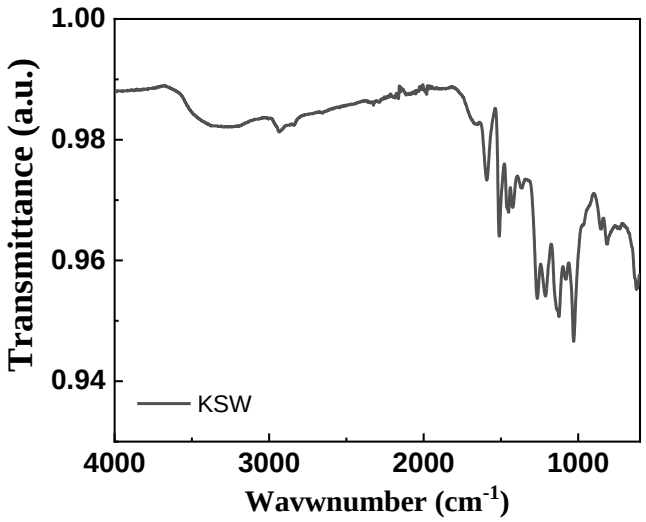

Figure 4.2 FTIR spectra of KSW lignin.

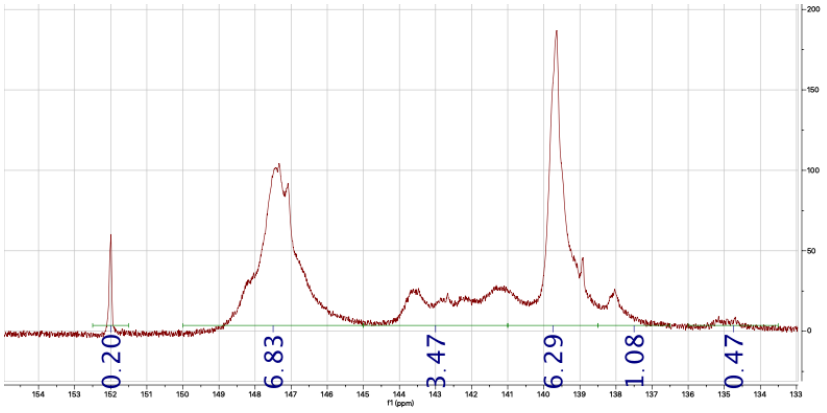

Figure 4.3 ^{31}P NMR spectra of KSW lignin.

Table 4.2 Hydroxyl group contents of KSW lignin obtained by ^{31}P NMR.

Lignin functional group	Chemical shift (ppm)	Content (mmol/g lignin)
Internal standard	152.5-151.5	0.20
Aliphatic OH groups	150-145	6.83
C_5 substituted OH groups	145-141	3.47
Guaiacyl OH groups	141-138.5	6.29
p-OH phenyl OH groups	138.5-136.5	1.08
COOH groups	136-133.5	0.47

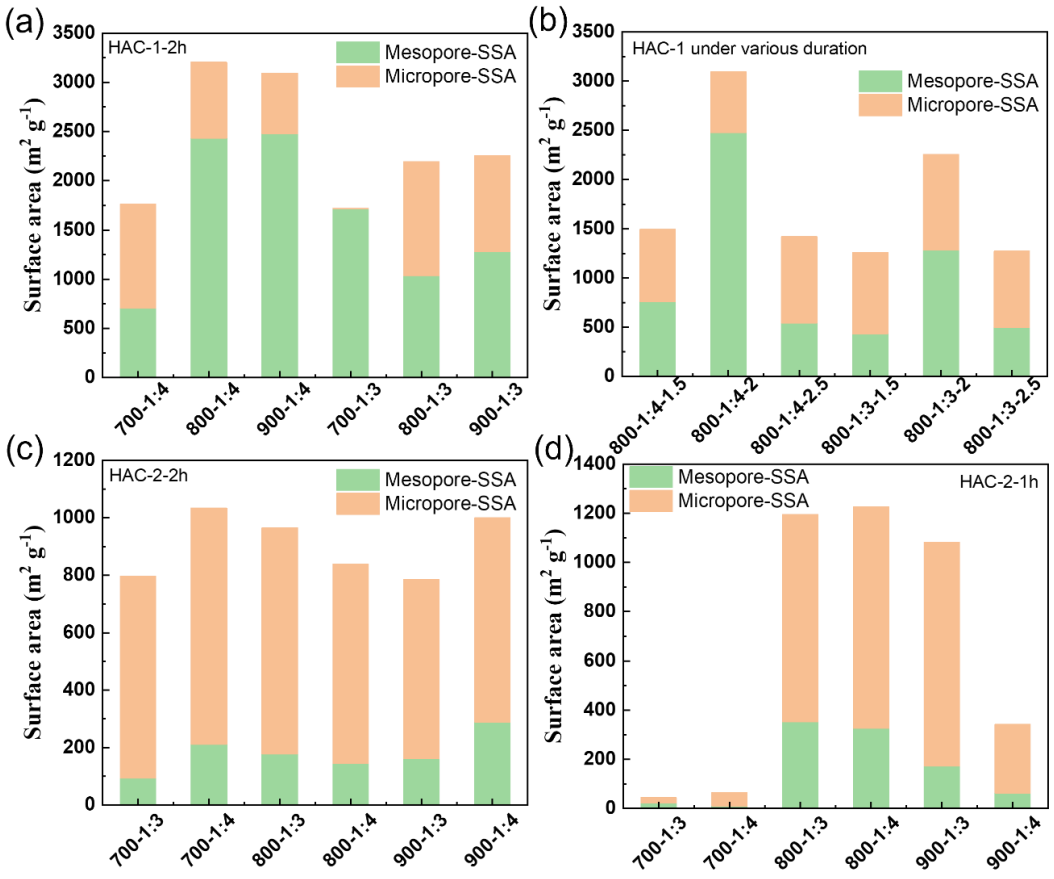

Figure 4.4 Surface area, mesopore and micropore distribution of ACs produced after one- (HAC-1s) and two-step (HAC-2s) activation methods.

observed that one step method produced samples achieve higher surface areas and mesopore ratios compared with two step method developed samples. The highest surface area of ACs after one-step activation is obtained with the ratio of 1:4 under 800 ℃ for 2 hrs, while the optimum condition of the two-step activation is 1:4 under 800℃ for 1 hr. As reactions during the one-step method is more intense and the process is relatively hard to control, the fluctuation of the surface areas of one-step produced samples are relatively larger than that two-step produced samples. The replicated results of HAC-1 are shown in Figure 4.5. As shown in Table 4.3, the BET surface area of HAC-1 arrives as high as 3,206.51 m^2 g^{-1}, which is 2.65 times of the surface area of HAC-2 (1,209.06 m^2 g^{-1}). In addition, HAC-1 achieved a mesopore ratio of 75.84%, while the mesopore ratio of HAC-2 is only about 26.96%. As we know, activated carbons are the most popular materials applied for electrodes for supercapacitors as well as adsorbents for water purification. However, usually the higher surface area is correlated with a more tortuous porosity, which leads to long diffusion distances and high ionic diffusion resistance. A high mesopore ratio benefits the diffusion of ions. Figure 4.6 shows the DFT pore size distributions of these two samples, we observe that mesopore volume is predominant for HAC-1 sample. There are obvious increases of the surface area and pore volume in the mesopore region of HAC-1 compared with HAC-2, while the micropores contribute similarly to the surface area and pore volume for both samples.

SEM images of HAC-1 and HAC-2 are illustrated in Figures 4.7. According to Figure 4.7 (a, c), the particle size of HAC-1 is obviously larger than that of HAC-2, as the HAC-2 were produced after two-steps and ball milling was conducted twice, after both carbonization and activation. HAC-1 was only ball milled once after one-step activation. In Figure 4.7 (b, d), more porosity is present with HAC-1 than HAC-2 under high magnification.

Raman spectroscopy was performed to characterize the physical structure of the one- and two-step activation produced ACs. As displayed in Figure 4.8, both samples exhibit strong

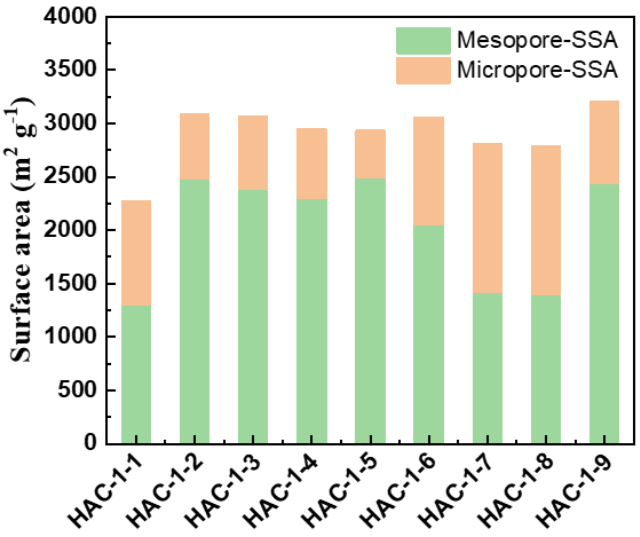

Figure 4.5 Surface area, mesopore and micropore distribution of replicates of HAC-1 samples.

Table 4.3 Pore structures of one-step and two-step produced activated carbons prepared from KSW lignin.

Carbon type	Specific surface area			Pore volume		
	S_{BET} (m^2 g^{-1})	Surface Area from micropores (%)	Surface Area from mesopores (%)	V_t (cm^3 g^{-1})	V_{micro} (%)	V_{meso} (%)
HAC-1	3206.51	24.16	75.84	2.20	25.90	74.10
HAC-2	1209.06	73.04	26.96	0.76	61.70	38.30

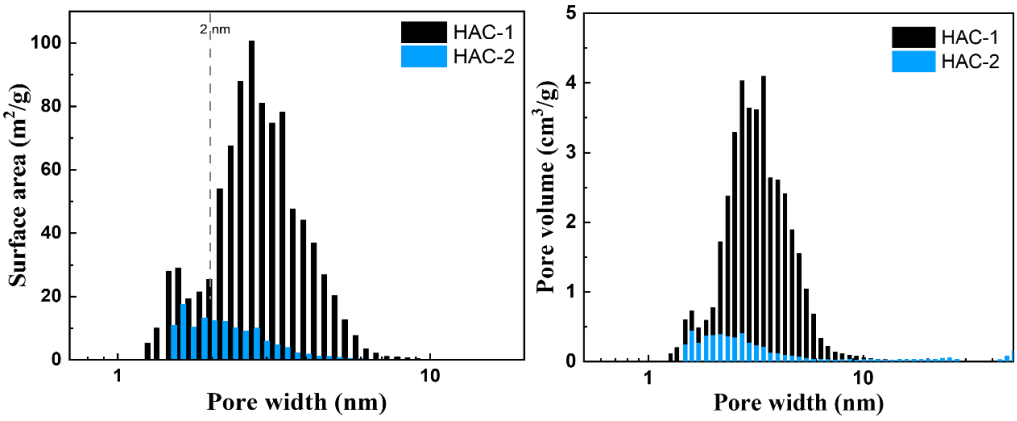

Figure 4.6 (a, b) DFT pore size distributions of HAC-1 and HAC-2 samples.

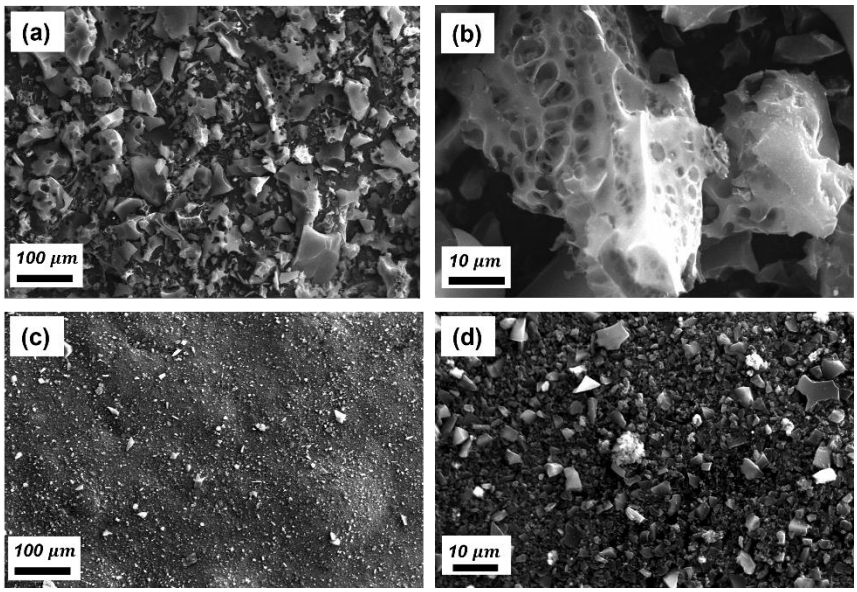

Figure 4.7 SEM images of (a, b) HAC-1 and (c, d) HAC-2 samples.

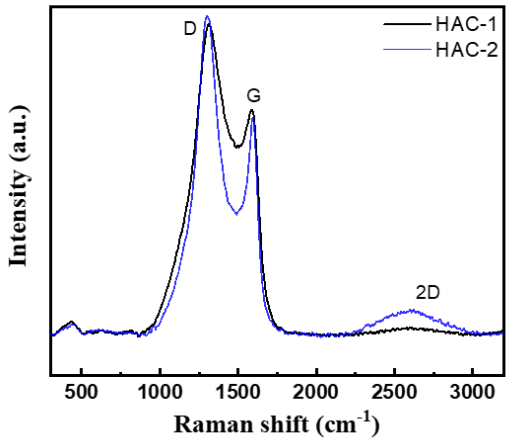

Figure 4.8 Raman spectra of HAC-1 and HAC-2 samples.

D bands (around 1310 cm^{-1}) and G bands (around 1590 cm^{-1}). Generally, the D band represents the sp3 carbons, referring to the disordered and defects carbon structures, and G band originates from sp2 carbons, which is associated with the ordered graphitic structure. It is generally recognized the I_D/I_G ratio is indicative of the graphitization level of the carbon materials.[149] The I_D/I_G of HAC-1 is 1.47 for HAC-1, and 1.38 for HAC-2. The higher I_D/I_G ratio of HAC-1 indicates the more amorphous structure and defects, which results from the higher porosity of HAC-1 sample compared with HAC-2. In addition, it is apparent that the peaks of the HAC-2 are much narrower than that of HAC-1, indicating the greater graphitization of HAC-2 sample. The broad peaks in HAC-1 are correlated to the distribution of clusters with different orders and dimensions.[149] It should also be noted that there is a slight shift of the D and G peak positions between the two samples, which is related to the structural changes at atomic level.[150] The D band position down shifts from 1311 to 1302 cm^{-1} from HAC-1 to HAC-2, indicating the formation of the aromatic clusters with larger size under two-step activation.[151] The G band position shifts from 1586 to 1596 cm^{-1} from HAC-1 to HAC-2, which is correlated with an increase in functional groups bonded to the surfaces of the HAC-2 samples.[149]

To further examine the surface functionalities of both HAC-1 and HAC-2 samples, XPS measurements were conducted. XPS surface elemental analysis (Table 4.4) shows that HAC-1 and HAC-2 contain O/C ratio of 18.1 and 7.3, respectively. As shown in Figure 4.9 (a, b), the C 1s peak were deconvoluted by a multiple Gaussian function into three peaks centered at 284.8 eV (C=C or C-C), 286.0 eV (C-O) and 288.5 eV (O-C=O or C=O).[136] It is apparent that the adsorption intensity of O-C=O or C=O peak in HAC-2 sample is enhanced, which takes 26.0% of the total integration area. For HAC-1 sample, it contains more C-O groups which takes 25.0% of the total integration area. To further clarify the distribution of oxygen functional groups on the surface of two samples, the O 1s peak were decomposed into two peaks and represent C=O (~531.5 eV) and C-O (~533.0), which refers to the carboxyl/carbonyl and hydroxyl groups, respectively. As shown in Figure 4.9 (c, d), the C-O is predominant in HAC-1 sample since it takes 61.2 % of the total integration

Table 4.4 Elemental analysis by XPS and CHN measurements of HAC-1 and HAC-2 samples.

	HAC-1	HAC-2
XPS surface elemental analysis		
O/C	7.3	18.1
CHN elemental analysis		
O/C	8.6	29.2

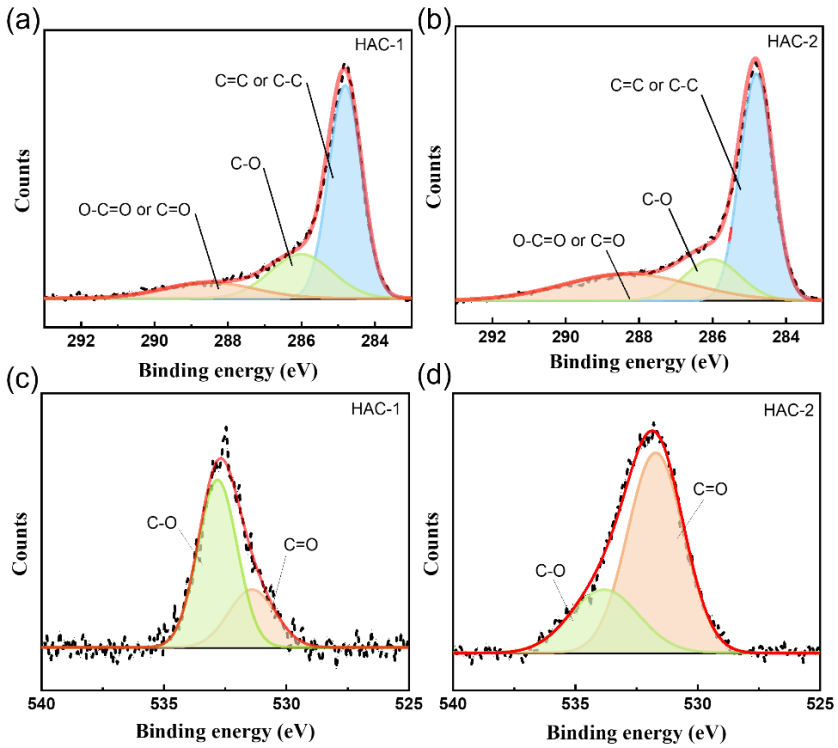

Figure 4.9 High resolution XPS spectra of C 1s peak of (a) HAC-1 and (b) HAC-2; O1s peak of (c) HAC-1 and (d) HAC-2.

area, while HAC-2 primarily contains C=O, which takes 72.2% of the total integration area. The C=O bonds, which refers to the carboxyl and carbonyl groups, have higher polarity compared with C-O (hydroxyl groups), thus leading to the high hydrophilicity of HAC-2 sample. Accordingly, HAC-2 contains more surface functionalities with higher O/C ratio, which is in consistent with Raman results.

As XPS is a surface characterization technique, we also conducted the CHN measurements for clarifying the O/C ratio for the bulk materials. As shown in Table 4.4, O/C ratio of HAC-2 increases from 18.1 to 29.2, indicating the oxygen not only existed on the surface of carbons, but also doped into the porous structure, which would be beneficial to the electrical conductivity of HAC-2 sample.

Electrochemical performance

To test the performance of one- and two-step activation produced ACs, the capacitances were measured by galvanostatic charge discharge (GCD) measurements within a potential window of 0 - 1.0 V and at a current density of 0.2 A g^{-1}. As shown in Figure 4.10 (a, b), the charging and discharging times of HAC-1 electrode are much higher than that of the HAC-2, confirming the higher capacitance of HAC-1 electrode at low current density due to its much higher surface area. The HAC-2 electrode shows more obvious shoulders at 0.4 - 0.5 V, which are attributed to the pseudocapacitance from the redox reactions of the oxygen functional groups. Current-Voltage (CV) curves of HAC-1 and HAC-2 are shown in Figure 4.10 (c, d). The HAC-2 electrode shows both pseudo capacitor behavior and EDL capacitor behavior, while HAC-1 electrode demonstrates more clearly the rectangular shape of the CV curve, characteristic of the EDL capacitor. The more obvious current leakage with increasing sweep speed in HAC-1 sample indicates that HAC-1 should have a relatively larger equivalent series resistance.

To further evaluate the ion diffusion and electronic transport within the electrodes, electrochemical impedance spectroscopy (EIS) was performed. Figure 4.11 (a) shows the

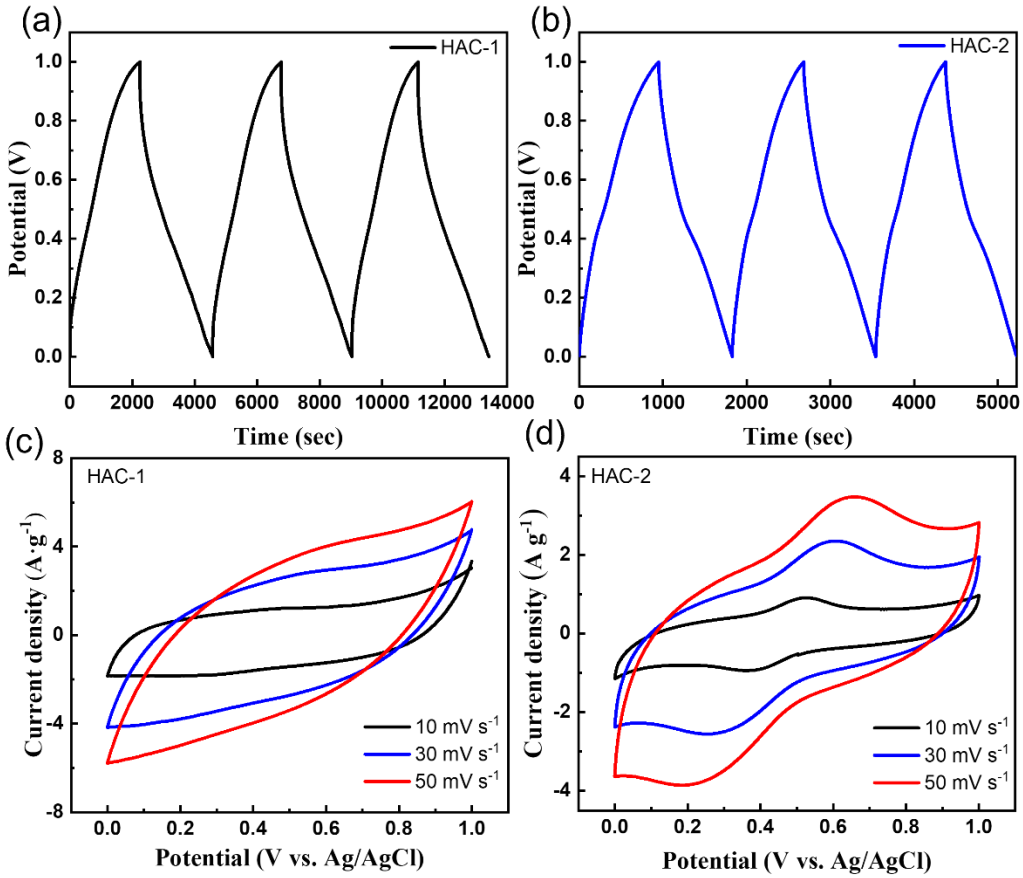

Figure 4.10 GCD curves of (a) HAC-1, (b) HAC-2 electrodes charged and discharged at 0.2 A g^{-1}, CV curves of (c) HAC-1, (d) HAC-2 electrodes at different scan rates.

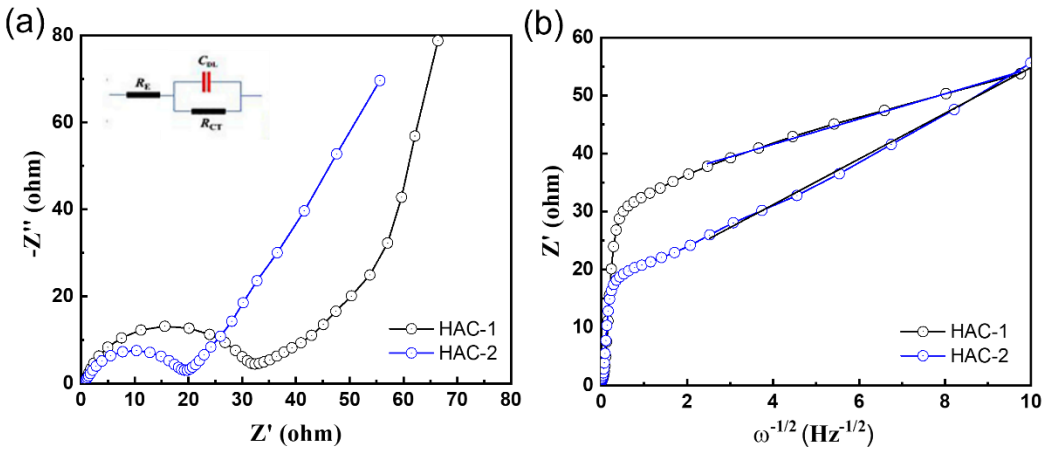

Figure 4.11 (a) Nyquist plots of different capacitors at OCV, where an equivalent circuit was proposed for describing the impedance behavior within the frequency range between 100 kHz and 1 Hz. (B) Randles plots of different capacitors at open circuit voltage.

Nyquist plot of the fabricated electrodes. Usually, in the high frequency region (100 kHz - 1 Hz), the intersection of the semicircle with the x-axis is attributed to the internal resistance, which including the electrolyte resistance (R_e) and charge transfer resistance (R_{ct}) at the interface between the electrode and electrolyte. The resistance was calculated based on the equivalent circuit model (shown in the insert of Figure 4.11 (a)) and analyzed with the Z-view software.[144] The difference in the electrolyte resistance is negligible as we used the same electrolyte for both HAC-1 and HAC-2. However, the R_{ct} are calculated to be 33.8 and 20.6 Ω for HAC-1 and HAC-2, respectively. The much higher charge transfer resistance of HAC-1 should be attributed to its much higher surface area, more complex porosity and more hydrophobic structure, resulting in the higher charge transfer resistance within the pore structure. However, in the low frequency region (1 Hz - 1 mHz), the inclined line is assigned to the Warburg impedance (Z_D), which corresponds to the ion diffusion process within the porous structure. Usually, the more vertical line suggests a lower diffusion resistance. We can observe the trend for the HAC-1 electrode that the diffusion resistance gradually decreases with decreasing frequency, because the pore structure becomes more significant for the diffusion process at low frequency. The diffusion resistance of HAC-1 is greatly reduced due to its high mesopore ratio. Figure 4.11 (b) presents the "Randles plot" for both electrodes to detail the diffusion process of protons within the porous structures at low frequencies. Here, k_W represents the Warburg coefficient and is obtained from the slope of the Randles plots. The diffusion coefficient (D) is calculated based on the follow equation:

$$k_W = \frac{RT}{n^2F^2A\sqrt{2}}\left(\frac{1}{D^{1/2}C^*}\right)$$

where n is the charge-transfer number, A is the electrode surface area, and C^* is the ionic concentration, and all those parameters are already known. The calculated diffusion coefficients are 4.66×10^{-10} and 1.43×10^{-10} $cm^2\ s^{-1}$ for HAC-1 and HAC-2, respectively. The diffusion coefficient of HAC-1 is three times higher than that of HAC-2, revealing the ionic diffusion resistance is significantly alleviated for the HAC-1 electrode. The mesopore ratio of HAC-1 significantly facilitates ion diffusion under low charge and discharge speed.

Accordingly, the highly mesoporous structure of HAC-1 electrode facilitates the ions diffusion and results in a high-performance EDL capacitor due to its ultrahigh surface area, which leads to high capacitance under low current density. The more hydrophilic surface of HAC-2 sample improves the affinity of electrode towards aqueous electrolyte, thus leading to the lower internal resistance.

As shown in Figure 4.12(a), the capacitance of HAC-1 electrode reaches 812.3 F g^{-1} at 0.1 A g^{-1}, which is more than doubled of HAC-2 one (i.e., 405.2 F g^{-1}). For comparison, the electrochemical performance of ACs produced by various biomass precursors from other publications are listed in Table 2.1. We could observe the excellent electrochemical performance of our produced HACs. It should also be noticed that, as the internal resistance starts to play a more important role of affecting the capacitance under high current density, the capacitance of HAC-1 decreases faster with the increased current densities, while HAC-2 achieves the plateau. The energy density and power density were calculated based on the following equations:

$$E = \frac{C(\Delta V)^2}{2} \quad \text{(R6)}$$

$$P = \frac{E}{\Delta t} \quad \text{(R7)}$$

where C is the specific capacitance (F g^{-1}), ΔV (V) is the potential window, and Δt (s) is the discharge time. The calculated results are shown in Ragone plots (Figure 4.12(b)). The HAC-1 based SCs achieved an ultrahigh energy density of 112.8 Wh kg^{-1} at a power density of 62.5 W kg^{-1}, while HAC-2 based SCs obtained better power density performance with the power density of 5882.4 W kg^{-1} at the energy density of 7.5 Wh kg^{-1}. As shown in Figure 4.13, compared to the energy density and power density of SCs with various electrodes from other publications, HAC-1 based SCs achieved superior performance with ultra-high energy density.

MB adsorption performance

To investigate the potential utilization of activated carbons in dye removal, the cation dye methylene blue (MB) (Figure 4.14) was involved in the dye adsorption study. The

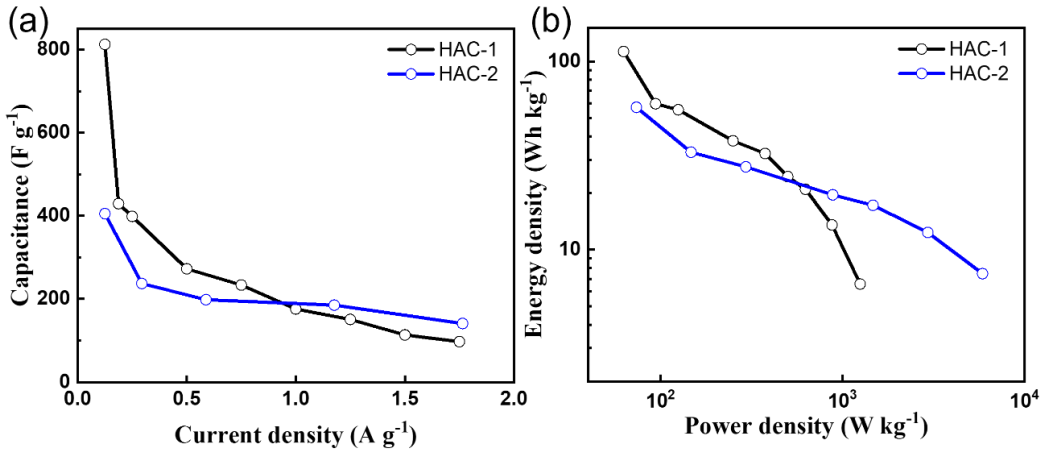

Figure 4.12 (a) Variation of specific capacitance of electrodes with current densities, and (b) ragone plot of the HAC-1 and HAC-2 SCs.

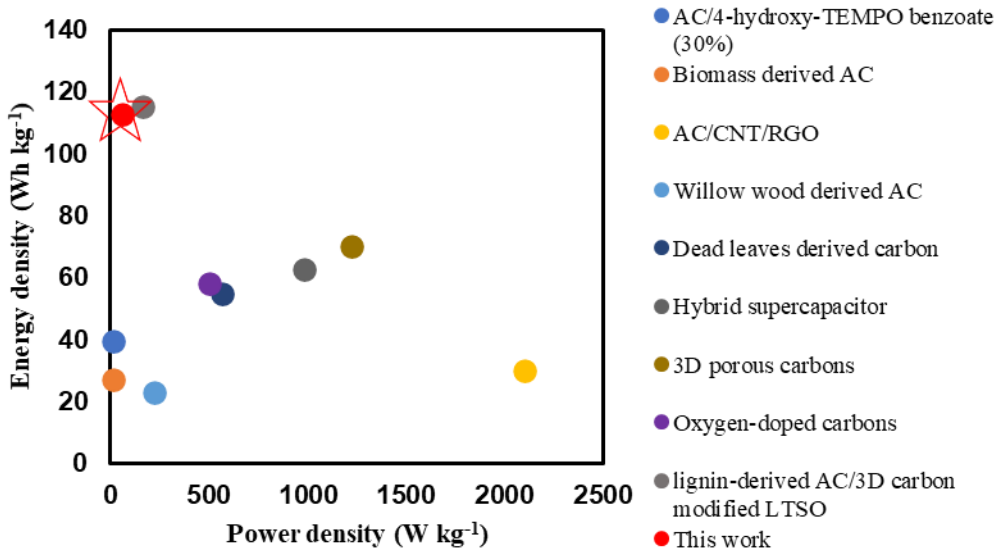

Figure 4.13 Comparison of energy density of SCs with various electrodes from publications.[152-160]

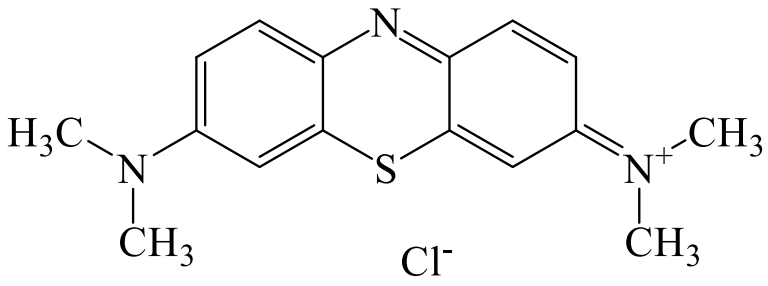

Figure 4.14 Methylene blue structure.

adsorption isotherm is used to study the relationship between adsorbate molecules and adsorbent surface. As shown in Figure 4.15, the linear Langmuir model was fitted with the equilibrium data (Eq. 2) and the fitting results were all presented with high statistical indicators R^2（Table. 4.5).

$$\frac{C_e}{Q_e} = \frac{1}{Q_m K_L} + \frac{C_e}{Q_m} \quad (2)$$

where K_L is Langmuir isotherm constant (L/mg), C_e, Q_e, and Q_m are the MB concentration at equilibrium (mg/L), adsorption capacity at equilibrium (mg/L), and maximum adsorption capacity (mg/g), respectively. Therefore, the high R^2 values (> 0.99) indicated that Langmuir model was suitable to describe MB adsorption on activated carbons and the adsorption process could be considered as a monolayer adsorption type with finite adsorption sites and uniform adsorption energies.[161] The theoretical Q_m can be calculated from Eq. 2 and the results are listed in Table. 4.5. Through the results of sample surface area and maximum adsorption capacity, both HAC-1 and HAC-2 samples showed the similar trend that higher surface area resulted in higher maximum adsorption capacity, which indicated that the higher surface area provided more available sites for attracting MB dye molecules to the activated carbon surface through electrostatic attraction. In particular, the theoretical Q_m of HAC-$1_{1:4\text{-}800\text{-}2}$ reached to 1250 mg g^{-1} implied the excellent dye removal ability. Although HAC-2 samples had relatively lower surface area compared to HAC-1 samples, the dye adsorption capacities were still impressive due to the abundance of functional groups and higher ratio of carboxyl/carbonyl groups on the HAC-2 surface. The maximum MB adsorption capacity of HAC-2 samples could achieve up to 476.19 mg g^{-1}, which is also comparable to the current literature.

Conclusions

This work investigated the effect of one- and two-step KOH activation on the surface properties of lignin-based activated carbons. One-step activation produced ACs achieved ultrahigh surface area as well as high mesopore ratio, leading to the ultrahigh energy density of the fabricated SCs as well as the ultrahigh MB adsorption capacity. The ionic

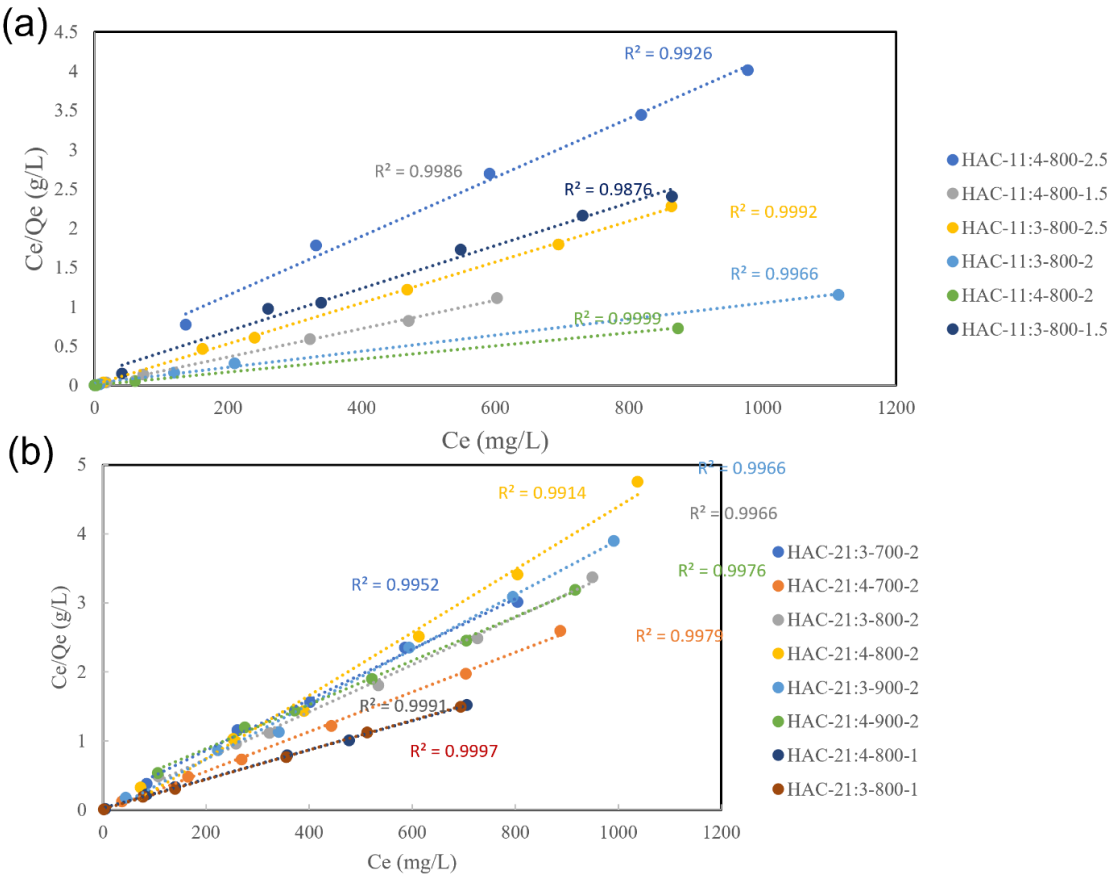

Figure 4.15 Linear Langmuir model fitted with the equilibrium data of one- and two-step activation produced ACs for MB adsorption.

Table 4.5 Sample surface area, maximum adsorption capacity, and Langmuir adsorption statistical indicators.

Samples	Surface area ($m^2\ g^{-1}$)	Q_m ($mg\ g^{-1}$)	R^2
$HAC\text{-}1_{1:3\text{-}800\text{-}1.5}$	1260	370.37	0.9876
$HAC\text{-}1_{1:3\text{-}800\text{-}2.5}$	1272	384.62	0.9992
$HAC\text{-}1_{1:4\text{-}800\text{-}2.5}$	1419	263.16	0.9926
$HAC\text{-}1_{1:4\text{-}800\text{-}1.5}$	1493	555.56	0.9959
$HAC\text{-}1_{1:3\text{-}800\text{-}2}$	2256	1000	0.9966
$HAC\text{-}1_{1:4\text{-}800\text{-}2}$	3207	1250	0.999
$HAC\text{-}2_{1:4\text{-}800\text{-}2}$	716	217.39	0.9914
$HAC\text{-}2_{1:3\text{-}900\text{-}2}$	786	250	0.9966
$HAC\text{-}2_{1:3\text{-}700\text{-}2}$	797	270.27	0.9952
$HAC\text{-}2_{1:3\text{-}800\text{-}2}$	1036	294.12	0.9966
$HAC\text{-}2_{1:4\text{-}900\text{-}2}$	1000	312.5	0.9976
$HAC\text{-}2_{1:4\text{-}700\text{-}2}$	1035	344.83	0.9979
$HAC\text{-}2_{1:3\text{-}800\text{-}1}$	1195	476.19	0.9997
$HAC\text{-}2_{1:4\text{-}800\text{-}1}$	1227	476.19	0.9991

diffusion resistance is greatly alleviated within the porous structure due to its high mesopore ratio. However, the relative hydrophobic surface limited its application for high power density SCs. In comparison, the two-step activation produced ACs has limited surface area but high oxygen contents, the oxygen not only existed on the surface but also doped inside porous structure, leading to the hydrophilic surface. The hydrophilicity of ACs greatly decreases the internal resistance and benefits the capacitance even at high current density, thus achieving high power density of the fabricated SCs. The dye adsorption capacities are also impressive due to the abundance of functional groups and higher ratio of carboxyl/carbonyl groups on the carbon surface. In summary, tailored pore structures of ACs with surface area from 50 to 3500 m^2 g^{-1} and mesopore ratio from 10 to 80% can be produced through controlling process conditions according to our methodology. The produced ACs have promising potential to be applied for high performance supercapacitors as well as in environmental applications.

Chapter 5 Lignin-derived Magnetic Activated Carbons for Effective Cation Dye Removal

A version of this chapter is prepared for publication by Yu L, Keffer D.J., Hsieh C.T., Chen H., Dai S., Harper D.P.:

Yu L, Keffer D.J., Hsieh C.T., Chen H., Dai S., Harper D.P., Lignin-derived magnetic activated carbons for effective cation dye removal.

Credit authorship contribution statement:
Conceptualization, LY, DH; methodology, LY, CT-H, DK, SD, DH; validation, LY, HC; formal analysis, LY, DK; resources, DK, SD, DH; writing—original draft preparation, LY; writing—review and editing, DK, HC, SD, DH; visualization, LY; supervision, DH, DK, SD; project administration, DH; funding acquisition, DH, SD.

Abstract

Large-scale environmental remediation of polluted water requires an effective and recyclable adsorbent produced from an abundant, low-cost, and renewable feedstock via a simple processing procedure. In this work, we demonstrate that lignin-derived magnetic activated carbons (mACs) satisfy these four criteria for (i) high-performance adsorption, (ii) high regeneration efficiency, (iii) feedstock economic and environmental viability, and (iv) single-step processing. The mACs are synthesized via an efficient co-carbonization and activation with simultaneous impregnation of ferric sulfate. The Langmuir model closely fits the adsorption of methylene blue (MB) by mACs within the temperature range of 298–323 K, where the adsorption capacity increases as temperature increases. This capacity increased from 55.0 mg g^{-1} to 220.2 mg g^{-1} with the presence of magnetic nanoparticles. In addition, the magnetite nanoparticles on the ACs surface significantly improve its recycling ability with the removal percentage above 95% after four cycles for 5:1 mAC.

Introduction

Dyes produced via industrial activities have become one of the most severe water pollutants

and cause environmental concerns. With the increasing need for ecologic protection and sustainable development, water purification has been a critical technique to address this pollution problem. Various ways, including membrane separation,[162] photocatalysis,[163, 164] biodegradation[165], and adsorption[166], have been applied in this field. Among these, adsorption offers a practical and low-cost approach.[166, 167] Activated carbon materials (ACs) are widely used as adsorbents for many organic and inorganic environmental pollutants industrially as they possess high surface area, low cost, and high surface reactivity.[168, 169] After use, the carbon adsorbents are hard to collect and recycle. However, magnetic activated carbon composites offer a potential efficient solution. Compared with conventional carbon adsorbents, magnetizing the adsorbents allows for easy separation from the solutions via an external magnetic field to collect and recycle multiple times. Decorating absorbent surfaces with magnetic nanoparticles significantly improve the adsorption performance by enhancing the electrostatic interaction between metal oxides and organic pollutants.[170, 171]

Magnetic carbon composites have been synthesized from various precursors, such as coconut,[172] graphene oxide,[173] and carbon nanotubes.[174] In addition to the choice of feedstock, the synthesis method is also a significant factor in the cost and efficiency of producing mAC for large-scale applications. Co-precipitation and hydrothermal synthesis are the most used methods to decorate magnetite onto carbon composites.[175-178] However, for most of the previous work, additional steps are involved, which increases the complexity and cost. Wang *et al.*[173] used a mixture of $FeCl_3$ and graphene oxide as precursors and heated in an autoclave for 6 hrs, achieving a maximum adsorption capacity of 65.79 mg g^{-1} for methylene blue (MB). Yu *et al.*[174] performed one-pot oxidation of multi-walled carbon nanotubes (MWCNTs) and Fe catalyst particles, yielding magnetic MWCNTs with maximum adsorption capacities of 227.05, 138.04, 63.34, 249.44, and 105.59 mg g^{-1} for ethylbenzene, *m*-xylene, *o*-xylene, *p*-xylene, and toluene, respectively. Liu *et al.* produced Fe_3O_4/AC composites via diol thermal decomposition for rhodamine B (RhB) and methyl orange (MO) adsorption. They doped AC by reacting

Fe(acetylacetonate)$_3$ in benzyl alcohol at N_2 atmosphere to yield Fe_3O_4/AC. The maximum adsorption capacities of 182.48 and 150.35 mg g^{-1} for RhB and MO, respectively, for the composite.[168]

Lignin is produced at a scale of 50-70 million tons annually as a byproduct of pulp and paper production.[2, 3] Lignin is an attractive feedstock for ACs because it is low-cost, renewable, and available in abundant quantities. Work has demonstrated converting lignin into high-value carbon materials with varying functional linkages controlled by feedstock and processing.[103, 106]

Within the above scope, we employ Kraft lignin (KL) as the carbon source and ferric sulfate as the precursor for mACs applied co-carbonization and activation. This concurrent synthetic route allows the synthesis of magnetic nanoparticles on carbon to occur simultaneously with activation. The iron serves both as a catalyst for AC formation and a precursor for active magnetic sites. Based on previous work,[144] lignin-based ACs primarily contain a complex microporous structure that limits accessibility to ions.[105-107] With the impregnation of iron into lignin, surface area and mesopore fraction are greatly improved, thus increasing the porous accessibility toward molecular adsorption in the liquid phase. The adsorption performance of mACs is evaluated by MB dye. The introduction of magnetite nanoparticles on the mACs leads to improved adsorption capacity and benefits the ease of recovery. We demonstrate that lignin-derived mACs are high-performance adsorbents synthesized from an economically and environmentally viable feedstock synthesized via a single-step manufacturing process.

Experimental section

Preparation of mACs adsorbent

The mAC was produced from commercial Kraft lignin (Indulin AT, Ingevity; Charleston, SC) (KL). The ferric sulfate was purchased from MP Biomedicals (Solon, OH). The mACs were synthesized by impregnating KL with ferric sulfate at different mass ratios (5:1, 10:1,

and 20:1 KL:ferric sulfate) in the ceramic boat. The precursor was carbonized at 800°C with nitrogen flow for 1 hour in the tube furnace. Without removal from the furnace, the carbonized magnetic carbons were exposed to steam activation (with the absolute humidity ~ 19 g m^{-3}) at 800°C for 0.5 h, as shown in Figure 5.1. The produced samples were ball-milled (PM100 RETSCH) at 400 revolutions per minute for 30 min to obtain powder mAC samples.

Materials characterization

X-ray diffraction (XRD) spectra were collected on an Empyrean diffractometer (Panalytical) with $\mathrm{Cu}-\mathrm{K}\alpha$ radiation. The morphology and elemental mapping images were obtained by scanning electron microscopy (SEM) (Zeiss, EVO MA15) and energy dispersive x-ray spectroscopy (EDS) (Bruker xFlash 6130) at a magnification of 2,000 respectively. X-ray photoelectron spectroscopy (XPS) was conducted using a Kratos AXIS Ultra DLD XPS system, equipped with a hemispherical energy analyzer and a monochromatic Al Kα source, operated at 15 keV and 150 W. The pass energy was fixed at 40 eV for the high-resolution scans and 160 eV for survey scans. Carbon C1s peak at 248.8 eV was used as a reference for charge correction. The porous structures of samples were evaluated via N_2 adsorption isotherms measured by a TriStar 3000 volumetric adsorption analyzer (Micromeritics Instrument Corp.). Specific surface areas (S_{BET}) were calculated based on Brunauer-Emmett-Teller (BET) equation, and pore volumes were derived by the Barrett-Joyner-Halenda (BJH) equation. Sample pore size distribution was determined by density function theory (DFT) calculations.

Liquid-phase adsorption evaluation

MB (Sigma) solutions were prepared with different concentrations (from 100 – 1200 mg L^{-1}) by mixing in an ultrasonic bath for 24 hrs at room temperature. The concentration of MB solutions was measured by ultraviolet-visible (UV-vis) spectroscopy (Thermo Scientific) at 665 nm. First, a calibration curve was obtained from a series of dye solutions of known dye concentration, as shown below:

$$y = 0.157 * x + 0.001$$

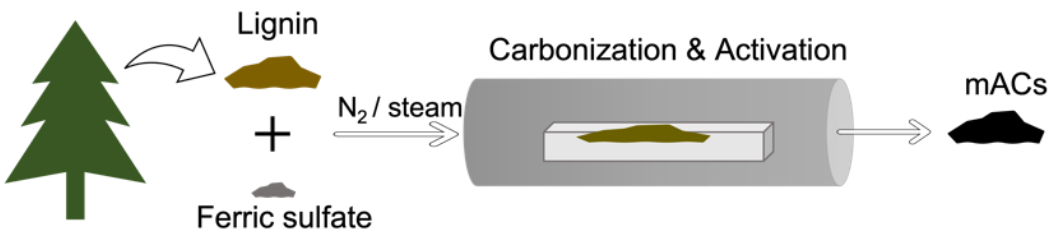

Figure 5.1 Schematic of mACs preparation via carbonization and activation of kraft lignin and ferric sulfate.

where x (mg L^{-1}) is concentration, and y is the adsorption intensity. Next, mACs and AC were immersed in MB solutions of different concentrations (from 100 – 1200 mg L^{-1}) for 48 h. The top solution was collected in a 1.5 ml centrifuge tube, and all the samples were centrifugated at 10000 rpm for 5 min before measuring UV-vis. Then the residual concentrations were calculated based on the calibration curve.

The reusability was tested by placing 0.10 g samples into 50.00 mL MB solution (100 mg L^{-1}) and kept for 24 h at room temperature with continuous stirring at 200 rpm. The AC and mAC materials were placed on a stirring plate with and without a magnetic stir bar, respectively. All mACs were effectively mixed on a magnetic stirring plate. The adsorbed samples were washed with 25.00 mL sulfuric acid (0.1 M) and stirred at 200 rpm for 8 h. For mACs and AC, the carbons were collected at the bottom of the vials with and without an external magnetic bar after settling. The top solution was removed. The vials were filled with deionized water (DI water) and stirred at 200 rpm for 0.5 h for washing. The step was repeated until a pH 7 was reached. The neutralized samples were dried in an oven at 105 °C for 0.5 h. The adsorption-desorption procedure was repeated for four cycles.

Results and discussions

Characterization of mACs

The mAC samples produced increased XRD intensities at lower mass ratios of AC to ferric sulfate (Figure 5.2(a)). The broad peak appearing around 24° is assigned to the (002) diffraction peak of amorphous AC. The interlayer distance (d_{002}) is calculated to be ~ 0.37 nm by the Scherrer equation, larger than that of graphite (0.335 nm). Diffraction peaks characteristic of Fe_3O_4 are present at 2θ = 30°, 35.3°, 43.5°, 53.1°, 57°, and 62.5°, representing the characteristics of (220), (311), (400), (422), (511), and (440) planes, respectively (as shown in Figure 5.2(b)), and agrees with the inorganic crystal structure database (ICSC) Card No. 35001ICSD. The peak located at around 33.3° corresponds to (104) plane of hematite (α-Fe_2O_3).[172] Peaks of the mACs sharpen with increasing iron sulfate content, confirming that more ferric sulfate in the precursors produces more

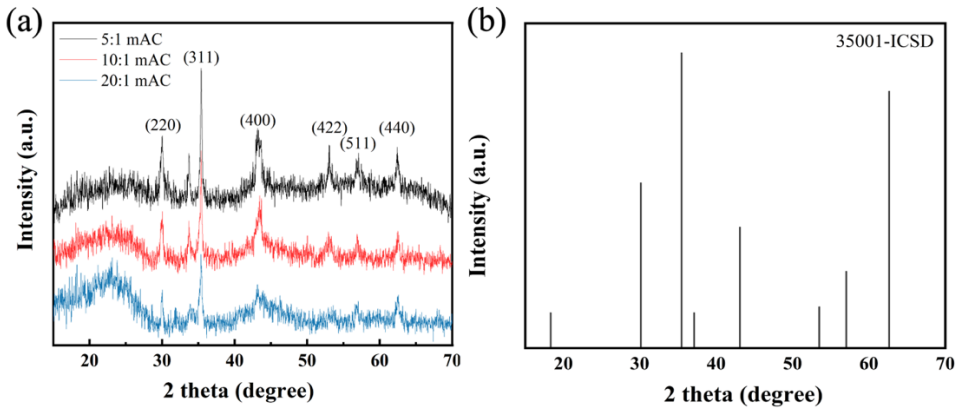

Figure 5.2 (a) XRD patterns of 5:1 mAC, 10:1 mAC and 20:1 mAC and (b) standard XRD pattern of Fe_3O_4 from 35001 ICSD card.

crystalline magnetite in the mAC.

For further clarification and confirmation, XPS spectroscopy was conducted on the mACs (Figure 5.3), which proved the presence of iron oxide in the resulting mAC products. Figure 5.4 The deconvoluted XPS spectra for Fe 2p possess peaks at *ca.* 712.0 eV and 724.0 eV attributed to Fe $2p_{3/2}$ and Fe $2p_{1/2}$, respectively. Deconvoluted peaks at 710.9 eV and 713.1 eV (Fe $2p_{3/2}$) correspond to Fe^{3+} and Fe^{2+} mixed oxide, respectively, and conf the presence of Fe_3O_4. The other two deconvoluted peaks at 724.1 and 725.9 eV are characteristics of α-Fe_2O_3.[172] Their atomic concentrations of Fe are 2.06%, 1.67%, and 0.64% for 5:1, 10:1, and 20:1 mACs, respectively (see Table 5.1). The deconvoluted O1s peaks of mAC samples are displayed in Figure 5.5. The fractions of Fe-O group are 18.6%, 13.9% and 10.9% for 5:1, 10:1 and 20:1 mACs, respectively. Accordingly, the 5:1 mAC shows the highest amount of iron oxide, consistent with the highest loading amount of $Fe_2(SO_4)_3$ in the precursor. Furthermore, the peaks at 532.0 eV and 533.0 eV correspond to C=O and C-O bonds, respectively. Three O1s peaks prove the existence of metal oxides (O^-), carbonyl, carboxyl, and hydroxyl functional groups.

Iron oxides (magnetite, hematite, and maghemite) are generated during the pyrolysis and activation processes. The reaction of ferric sulfate in a nitrogen environment is described in Eq 1a. The maghemite undergoes structural rearrangement and converts to hematite as the temperature goes up to around 400 °C.[169, 172] As the temperature increases above 600°C, some of the hematite reduces to magnetite (Eq 1b). The mACs are synthesized in the CO_2 environment after activation and partial oxidation of magnetite. The complex process leads to a mixture of Fe_3O_4 and Fe_2O_3 on the surface of mACs.

$$Fe_2(SO_4)_{3(s)} \xrightarrow{\Delta} Fe_2O_{3(s)} + 3SO_{3(g)} \quad (1a)$$

$$3Fe_2O_{3(s)} + C_{(s)} \xrightarrow{\Delta} 2Fe_3O_{4(s)} + CO_{(g)} \quad (1b)$$

$$2Fe_3O_{4(s)} + CO_{2(g)} \xrightarrow{\Delta} 3Fe_2O_{3(s)} + CO_{(g)} \quad (1c)$$

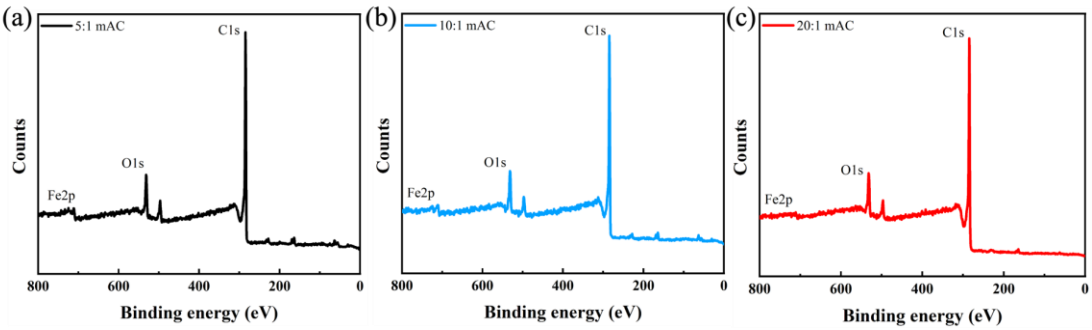

Figure 5.3 XPS survey spectra for (a) 5:1 mAC, (b) 10:1 mAC and (c) 20:1 mAC.

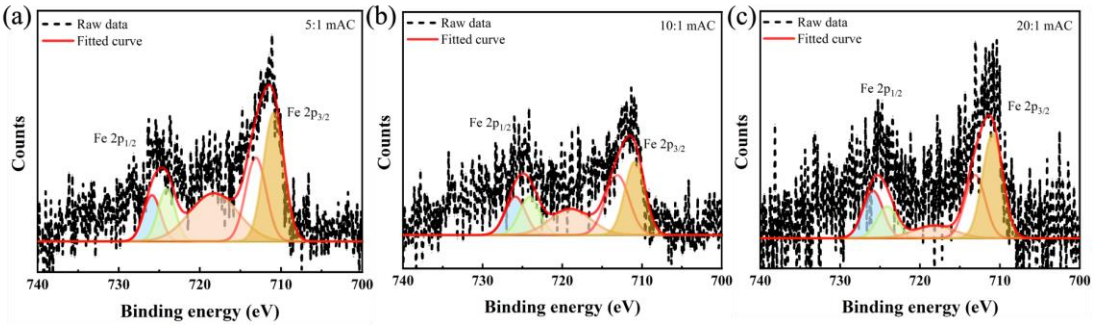

Figure 5.4 Deconvoluted XPS spectra of Fe 2p peak for (a) 5:1 mAC, (b) 10:1 mAC and (c) 20:1 mAC.

Table 5.1 Composition and elemental analysis of mACs obtained from deconvolution and integration of XPS peaks.

Chemical state	Atomic concentration (%)		
	5:1 mAC	10:1 mAC	20:1 mAC
C 1s	88.08	87.55	87.64
O 1s	6.95	7.30	9.52
Fe 2p	2.06	1.67	0.64
N 1s	0.73	1.17	0.90
Na 1s	2.17	2.31	1.3

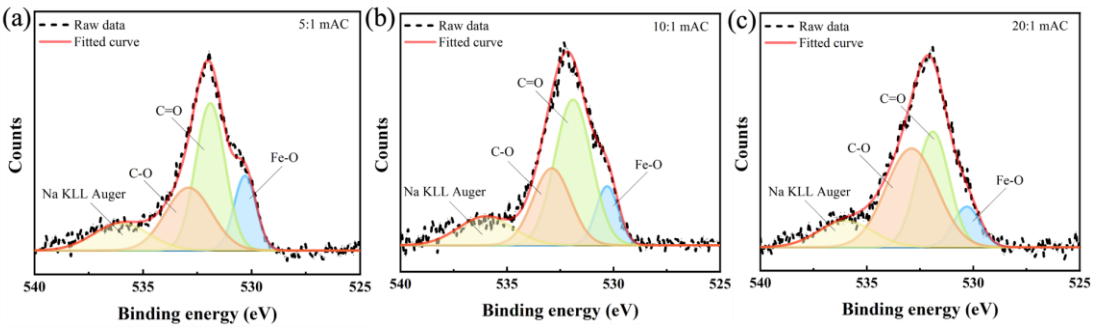

Figure 5.5 Deconvoluted XPS spectra of O 1s peak for (a) 5:1 mAC, (b) 10:1 mAC and (c) 20:1 mAC.

The mACs'XPS C 1s spectra of mACs were decomposed into three peaks centered at 284.8 eV (C=C or C-C), 286.0 eV (C-O), and 288.5 eV (C=O), respectively, confirming the presence of oxide functional groups on the surface of porous carbon structures (Figure 5.6). The C=O accounts for 8%, 8% and 4.3%, while C-O accounts for 23.7%, 28.5% and 27% of the total integration area for the 5:1, 10:1 and 20:1 mACs, respectively.

The morphological features of the mAC samples were characterized via SEM and EDS maps of Fe. As shown in Figure 5.7, the average particle size of AC on the 10:1 mAC sample is in the range of 10~20 μm, which is slightly larger than that of the 5:1 mAC (10~15 μm) and 20:1 mAC (5~10 μm). The generated EDS maps of elemental Fe confirm the homogeneous distribution of the iron oxide nanoparticles on the surface of mACs.

The pore size distributions of the samples are depicted in Figure 5.8. The mAC samples possess sharp peaks at pore size ~1 nm and broad peaks distributed ~ 2 – 6 nm, whereas the pure AC only exhibits a sharp peak at pore size ~1.8 nm, demonstrating the microporosity of pure ACs. From the large, broad peak in the range of 2 – 10 nm, we observe the mesopore fraction decreased in the sequence of 5:1 > 20:1 > 10:1 > AC. Table 5.2 summarizes S_{BET}, micro/mesopores ratio, $PV_{micro,}$ and PV_{meso}. The 5:1, 10:1, and 20:1 mACs have BET surface areas of 528.1, 515.8, and 512.8 $m^2 g^{-1}$, with a mesopore ratio of 17.0, 10.3, and 14.7%, respectively. In comparison, AC has a BET surface area of just 318.8 $m^2 g^{-1}$ and a mesopore ratio of only 1.6%. The surface area and mesopore volume are significantly increased with the impregnation of $Fe_2(SO_4)_3$ in the precursors, demonstrating the role of iron as a catalyst in the process of pyrolysis and activation.[169, 172] In addition, the iron is oxidized into iron oxide and grown on the surface of ACs during the pyrolysis and activation process, leading to the more porous structures of mACs.[168]

Adsorption performance of mACs

Adsorption isotherm

MB adsorption isotherms on the carbon samples were fit to the Langmuir model:

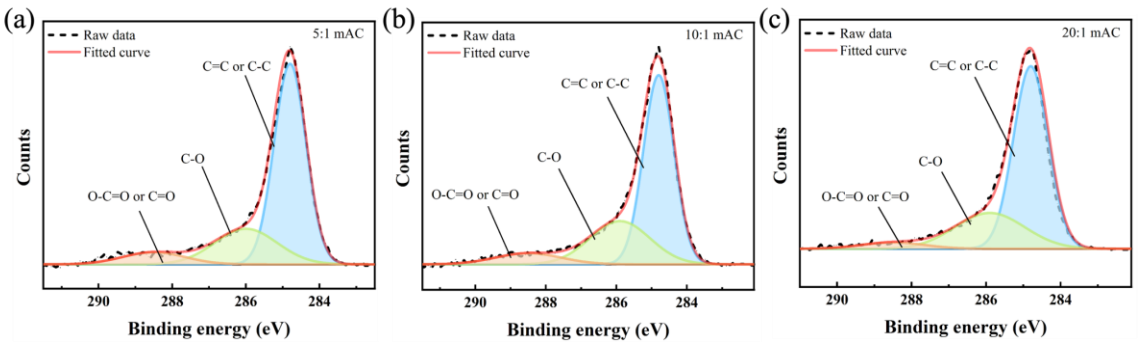

Figure 5.6 Deconvoluted XPS spectra of C 1s peak for (a) 5:1, (b) 10:1 and (c) 20:1 mACs.

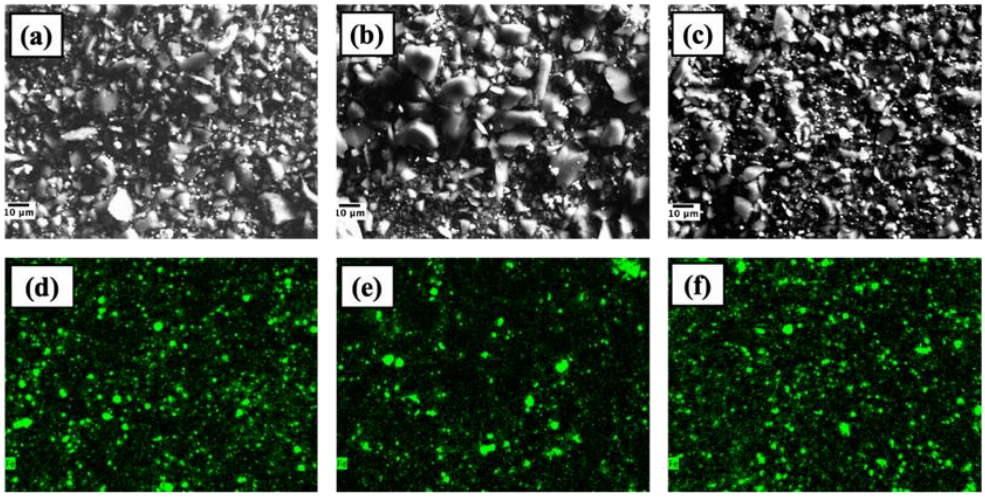

Figure 5.7 SEM images and EDS maps of Fe element of (a, d) 5:1, (b, e) 10:1 and (c, f) 20:1 mACs.

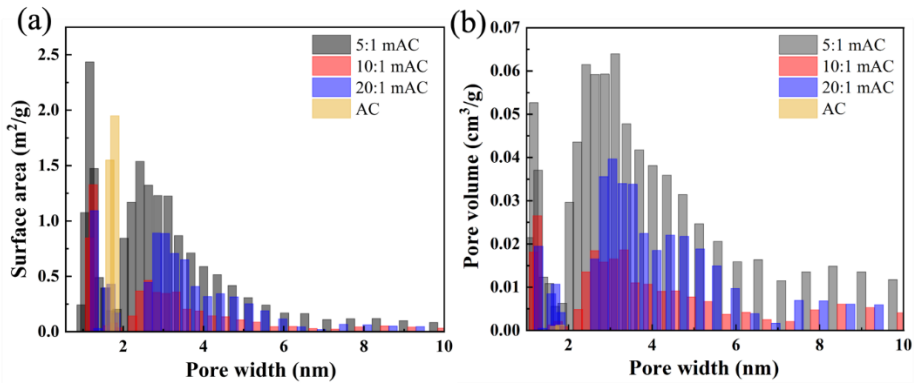

Figure 5.8 (a, b) DFT pore size distributions of mACs and AC.

Table 5.2 Characterization parameters (Fe %, S_{BET}, micropore/mesopore ratio, $PV_{micro,}$ and PV_{meso}) of mACs and AC determined from BET measurement.

Samples	Iron content (atomic conc %)	S_{BET} (m^2 g^{-1})	micropore ratio (%)	mesopore ratio (%)	PV_{micro} (cm^3 g^{-1})	PV_{meso} (cm^3 g^{-1})
5 : 1 mAC	2.06	528.1	83.0	17.0	0.21	0.09
10 : 1 mAC	1.67	515.8	89.7	10.3	0.22	0.05
20 : 1 mAC	0.64	512.8	85.3	14.7	0.21	0.08
AC	0	318.8	98.4	1.6	0.15	0.01

$$q_e = \frac{q_m K_L C_e}{1 + K_L C_e} \quad (2)$$

Where q_e (mg g^{-1}) is the amount of MB adsorbed per unit mass of carbon, C_e (mg L^{-1}) is the concentration of MB when the solution reaches the maximum adsorption amount of the carbon, q_m (mg g^{-1}), K_L (L mg^{-1}) is the Langmuir equilibrium constant. As shown in Figure 5.9, the Langmuir model fits the experimental data ($R^2 > 0.999$), indicating the assumption of monolayer adsorption is valid. The maximum adsorption capacities of mACs and AC are presented in Table 5.3. The theoretical maximum adsorption is greatly increased from 55.0 mg g^{-1} of AC to 220.2 mg g^{-1} for the 5:1 mAC. We assume that the higher surface area and pore volume allows for more accessible adsorption sites available for MB. Introducing iron in the precursors leads to higher surface area and greater mesopore ratio for the mACs over AC, thus MB adsorption. In addition, the maximum adsorption capacities for 5:1, 10:1, 20:1 mAC are 220.2, 151.1, 99.8 and 55.0 mg g^{-1}, respectively. Given that there is little difference in surface area and benefit from the pore structure (Table 5.2), iron oxide's presence on the surface greatly improves the adsorption performance of activated carbons.

Adsorption kinetics

The adsorption rate performance is the critical process metric for commercial applications.[179] Adsorption rates were measured by immersing 0.10 g samples into 50.00 mL MB solution (500 mg L^{-1}) at room temperature. We observed that the MB adsorption in 5:1 mAC occurs much more quickly than in the pristine AC (Figure 5.10(a)). The AC takes roughly 8 hrs to reach adsorption of 55 mg g^{-1}, whereas the same loading is obtained within 0.08 hr in the 5:1 mAC. Two mathematical models, which are pseudo-first order (eq 3a) and pseudo-second order (eq 3b) models, were adopted to describe the adsorption kinetics of MB.

$$\ln(q_e - q_t) = \ln(q_e) - k_1 t \quad (3a)$$

$$\frac{t}{q_t} = \frac{1}{k_2 {q_e}^2} + \frac{t}{q_e} \quad (3b)$$

Where q_e (mg g^{-1}) is the equilibrium adsorption amount of the adsorbent, q_t (mg g^{-1}) is the adsorption amount at t time, k_1 is the pseudo first order rate constant (h^{-1}), k_2 is the pseudo

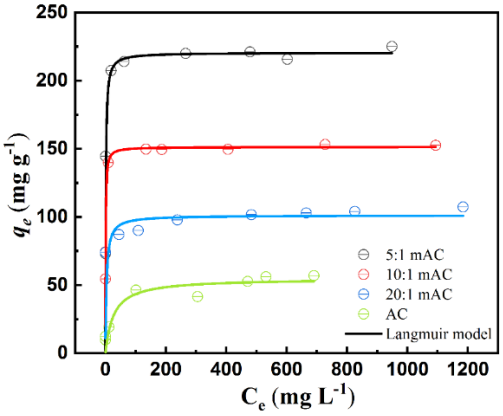

Figure 5.9 Adsorption isotherm curves fitted by Langmuir model of mACs and ACs.

Table 5.3 Parameters derived from the fits of the Langmuir model to the experimental data for mACs and ACs.

Samples	q_m (mg g^{-1})	K_L (L mg^{-1})	R^2
5:1 mAC	220.2	0.80	0.9999
10:1 mAC	151.1	1.28	0.9999
20:1 mAC	99.8	0.28	0.9998
AC	55.0	0.04	0.9996

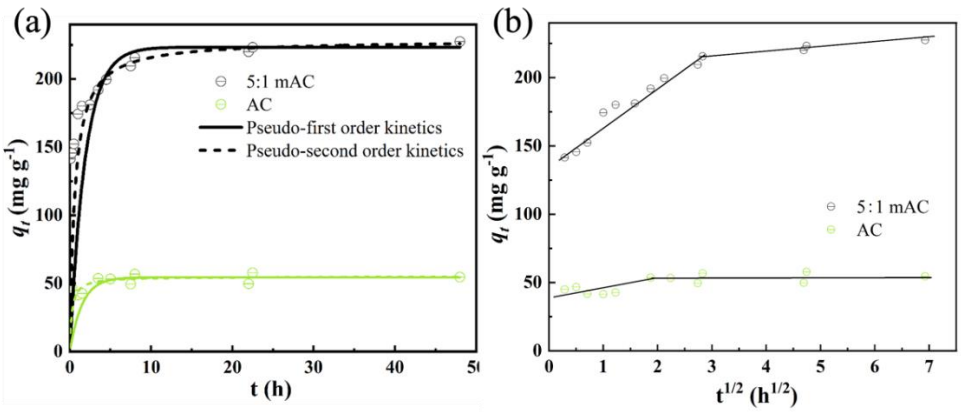

Figure 5.10 (a) Adsorbed amounts of MB as a function of time for 5:1 mAC and AC, and (b) kinetics of MB adsorption according to the intra-particle diffusion model.

second order rate constant (g/(mg·h)), and t is the contact time (h). To identify the sorption mechanism, both models were fit to the data (Table 5.4). The pseudo-first order model assumes the adsorption process is dominated by diffusion, whereas the pseudo-second order model describes chemical adsorption.[179-181] Both models fit the experimental data. The adsorption process can be further divided into membrane diffusion, intra-particle diffusion, and the actual adsorption steps.[179, 182] To confirm that the process is not strictly intra-particle diffusion controlled, the intra-particle diffusion model was fit to the experimental data (Figure 5.10(b)). If the plot of q_t versus $t^{1/2}$ exhibits only one linear section, the adsorption is controlled only by intra-particle diffusion. Conversely, multiple linear sections in the plots represent more than one process.[182] As shown in Figure 5.10(b), the plots consist of two straight lines, confirming that multiple mechanisms control the adsorption layer process. Further, the large intercepts indicate an additional mechanism controlling rate besides intra-particle diffusion.

Temperature effect on the adsorption

The adsorption properties were evaluated at different temperatures (from 298 to 323 K). Figure 5.11 shows the adsorption amount versus equilibrium concentration for the 5:1 mAC sample fitted by the Langmuir model at different temperatures (Table 5.5). The maximum adsorption capacities reach 329.6, 272.9, and 220.2 at 323, 313, and 298 K, respectively. The adsorption capacity of 5:1 mAC increases with increasing temperature and indicates an endothermic process promoting the adsorption of MB through a physical process.

Regeneration and recyclability of mACs

Absorbent stability and reusability are crucial for cost effective industrial removal of toxins from water. Owing to the magnetic properties, mACs can be easily collected by an external magnet (Figure 5.12(b)), which is convenient for recovery and reuse. To assess the regeneration efficiency of the mACs, an external magnet separated MB absorbed carbons. After separation, they were first washed with a sulfuric acid (1M) solution. Afterward, the

Table 5.4 Kinetic parameters of pseudo-first order, pseudo-second order model fits.

Adsorbents	Pseudo-first order			Pseudo-second order		
	q_e (mg g^{-1})	k_1 (h^{-1})	R^2	q_e (mg g^{-1})	k_2 (g/(mg·h))	R^2
5:1 mAC	223.4	0.53	0.9961	228.8	0.0073	0.9988
AC	54.5	0.66	0.9687	55.1	0.0728	0.9715

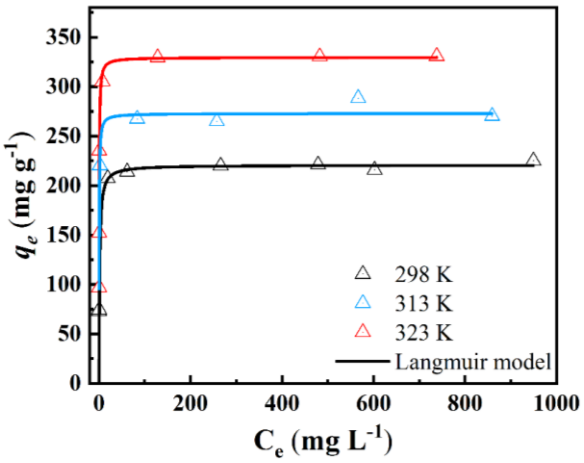

Figure 5.11 Adsorption isotherm curves fitted by Langmuir model of 5:1 mAC under 298, 313, and 323K.

Table 5.5 Adsorption isotherm parameters for MB onto 5:1 mAC at 298, 313, and 323 K.

5:1 mAC	q_m (mg g^{-1})	K_L (L mg^{-1})	R^2
298K	220.2	0.80	0.9999
313K	272.9	2.60	0.9868
323K	329.6	2.70	0.9699

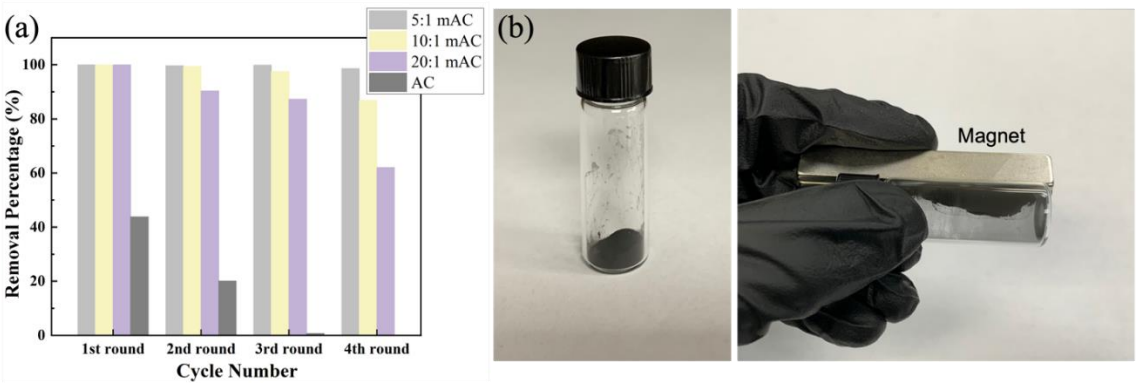

Figure 5.12 (a) Reusability test of mACs for MB adsorption and (b) images of mACs without and with the external magnet.

carbons were washed with DI water until neutralized. The adsorption and desorption cycles were repeated for four cycles, and the reusability of samples was determined by removal percentage (%):

$$Removal\ percentage\ (\%) = \frac{C_0 - C_t}{C_0} * 100 \quad (4)$$

where the C_0 (mg L^{-1}) is the initial concentration and C_t (mg L^{-1}) is the concentration at time t.

As shown in Figure 5.12(a), the 5:1 mAC sample shows excellent adsorption efficiency with the removal percentage above 98% for four cycles. For the 10:1 mAC, the removal percentage is slightly reduced on the 4th cycle but remains at 86.8%, possibly due to the incomplete dye desorption. The 20:1 mAC exhibits a decrease in adsorption efficiency (down to 90.3%) on the 2nd round, and the removal percentages are 87.3%, 62.0% for the 2nd and 3rd cycles, respectively. The reusability performance of mACs shows a trend as follows: 5:1 mAC > 10:1 mAC > 20:1 mAC > AC, demonstrating that the 5:1 mAC possesses the best reusability and remains as an efficient adsorbent even after four cycles. For comparison, the removal percentage of AC drops down from 43.8% for the 1st cycle to 20.1% for the 2nd cycle and loses efficiency at 3rd round recycle. This result supports the observation that the presence of magnetite nanoparticles facilitates the adsorption/desorption process of MB on the samples, and the magnetic nanoparticle loading positively correlates with the reusability of adsorbents.

Adsorption mechanisms

The atomic scale process behind the adsorption mechanism can arise from multiple factors, including the surface characteristics and heterogeneity, porosity and functional groups of adsorbents, and the molecular structure of adsorbates. For carbon materials, the adsorption between adsorbents and adsorbates occurs primarily through hydrogen bonding, π–π interactions, and electrostatic interactions. As shown in Figure 5.13, we proposed an adsorption mechanism for MB on mACs. The proposed mechanisms involved are illustrated. The surface functional groups were determined by XPS spectra, and the

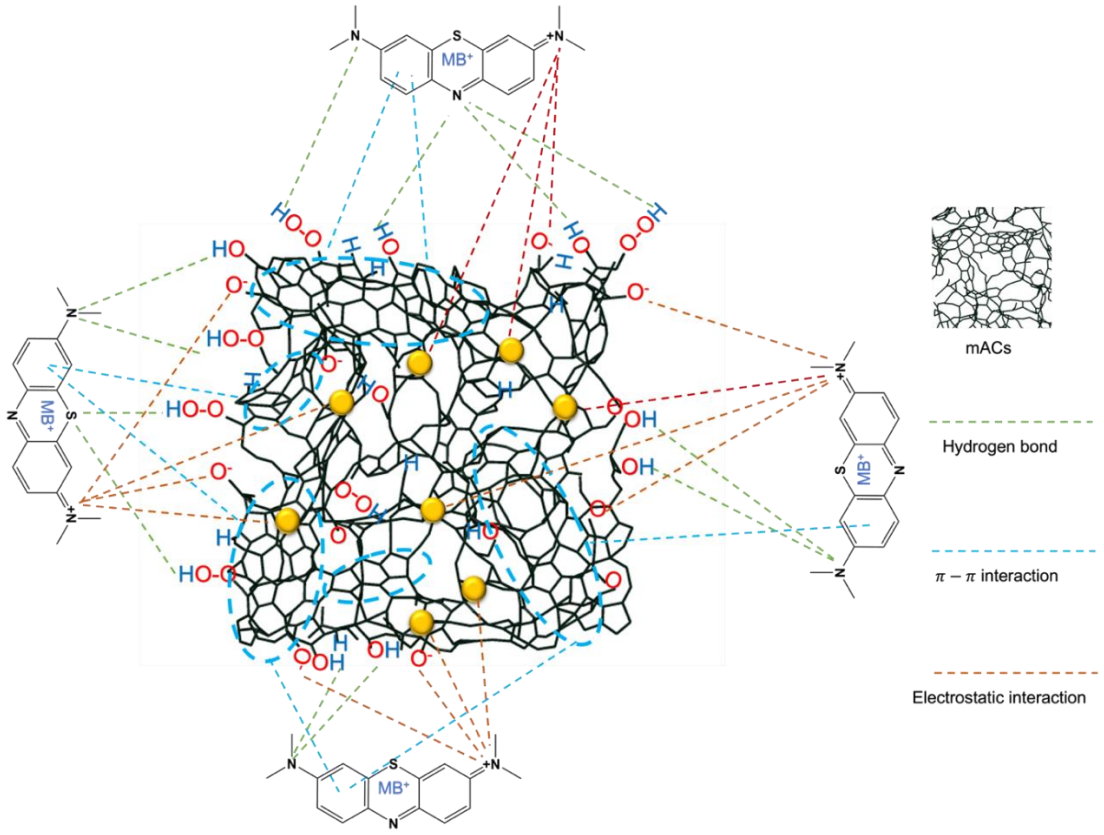

Figure 5.13 Adsorption mechanisms for MB onto mACs where the yellow dots represent a mixture of iron oxides.

adsorption mechanism for MB on mACs. The proposed mechanisms involved are illustrated. The surface functional groups were determined by XPS spectra, and the disordered graphite structure was confirmed by XRD measurement as well as previous work.[144, 183] The principal interaction should be the π−π interaction between the π−electron system on ACs and aromatic structure of MB, and the hydrogen bonding interactions between the carboxyl/hydroxyl functional groups and MB molecules.[184-186] In addition, the electrostatic interactions with cationic MB were introduced as the mAC's surface is negatively charged (O^-).[168, 169, 172] Additionally, the introduction of iron oxides on the surface of mAC leads to the vastly improved MB adsorption as well, which should be attributed to the enhanced electrostatic interaction between iron oxides and MB molecules.[170, 171]

Conclusions

We developed a simple route to synthesize mACs in a one-step process. A mixture of lignin and ferric sulfate were applied as precursors for co-carbonization and activation. Incorporating ferric sulfate into the lignin matrix improved the surface area of mACs with magnetic iron oxides nanoparticles uniformly distributed on the surface. These magnetite nanoparticles on ACs enhance the adsorption capacity and significantly improved the regeneration efficiency. The maximum adsorption capacity for MB was greatly increased from 55.0 mg g^{-1} on non-magnetic AC to 220.2 mg g^{-1} for the 5:1 mAC. The reusability test demonstrated that mACs could be easily separated magnetically and exhibited excellent reusability with high removal efficiency (> 98%) even after four use cycles. In conclusion, this work demonstrates that lignin-derived magnetic activated carbons are high performance adsorbents, synthesized from a lignin feedstock that is both economically and environmentally viable via a simple, single-step process.

Chapter 6 Synthesis of Lignin-based CQDs with Multicolor Emissions

A version of this chapter is still in preparation for lateral publication by Yu L., Ivanov, I.N., Hsieh C.T., Keffer D.J., Harper D.P.:

Yu L., Ivanov, I.N., Hsieh C.T., Keffer D.J., Harper D.P., Synthesis of Lignin-based CQDs with Multicolor Emissions

Credit authorship contribution statement:
Conceptualization, LY, CT-H, II; methodology, LY, CT-H, II, DK, DH; validation, LY; formal analysis, LY, II; resources, II, DK, DH; writing—original draft preparation, LY; writing—review and editing, II, CT-H, DK, DH; visualization, LY; supervision, DH, DK; project administration, DH; funding acquisition, DH.

Abstract

Carbon quantum dots (CQDs) were produced from lignin precursors by two-step hydrothermal methods. By controlling the experimental conditions, the produced CQDs, after separation via flash chromatography, emitted bright and stable luminescence from red to blue wavelengths (415 – 640 nm). In particular, the produced CQDs achieved deep blue color with the emission peak located at 415 nm with the full-width- at half-maximum (FWHM) about 71 nm. Additionally, we observed the redshift of the photoluminescence emission peak as increasing the CQD concentrations. The interaction between CQDs & CQDs and CQDs & solvent molecules affect the aggregation of CQDs. The formation of CD clusters with larger sizes as increasing the CQD concentrations resulted in a redshift of the photoluminescence emission peak.

Introduction

Due to their low-cost as well as nontoxic and tunable properties, carbon nanomaterials have attracted enormous attentions for application in various applications for addressing the environmental and energy challenges.[187] Among these, carbon quantum dots (CQDs) have been extensively explored and applied for bioimaging, biosensors, light-emitting devices,

which take advantage of their excellent photostability, biocompatibility and tunable fluorescence.[22, 23, 188] Various raw materials, including natural biomass and synthetic chemicals are widely used as carbon sources for synthesizing CQDs.[25, 189] Hundreds of approaches have been conducted for preparing the CQDs, and generally, these approaches are classified as top-down and bottom-up methods.[25, 188] In bottom-up synthesis methods, the CQDs are built up from the molecular chemicals. In top-down methods, the carbon precursors are broken down into smaller structures for synthesizing CQDs. In many optical applications of CQDs, a narrow emission spectrum is desirable. The breadth of the photoluminescence (PL) spectra (>80 nm) remains as a longstanding problem that limits the application of CQDs for light-emitting devices.[24] It is generally recognized that the broad PL spectra of CQDs are ascribed to structure-associated phenomenon as well as the broad size distribution,[24] as the CQDs are produced in complex mixtures after high pressure and high temperature process.[25] Several separation and purification methods, including dialysis, silica chromatography, high-performance liquid chromatography (HPLC), have been adopted for isolation of CQDs.[25] These purification methods drive the cost higher and limits production capacity. Although the exact origin of fluorescence of CQDs is debated, there are two general mechanisms: tunable surface states and quantum size effects.[24] For the surface states, it is well documented that the energy bands are dependent on the surface groups.[190, 191] Especially, the surface oxidation, which refers to the presence of oxygen functional groups on the CQDs, would contribute to a reduction in the bandgaps, thus leading to the redshift of the emission spectra.[25] It is also believed and confirmed by density functional theory (DFT) simulations that the band gap is theoretically size-dependent.[192, 193] The larger size of CQDs leads to the redshift of emission spectra. Lignin-based CQDs offer the opportunity to adjust optical properties related to the dot size.

In this work, we adopted the hydrothermal method and improved the effectiveness of hydrothermal methods for synthesis of CQDs from the lignin. The produced CQDs achieved multi-color emissions from red to blue. In particular, the CQDs with deep blue color were synthesized for better applications in the field of light-emitting devices. To

separate and purify the produced CQDs, ultracentrifugation as well as flash chromatography were conducted. We also quantify the phenomenon that emission and excitation peak shift resulting from aggregation of CQDs in solution.

Experimental section

Synthesis of CQDs from lignin

KSW lignin was pyrolyzed in a crucible in a tube furnace at 1000℃ for 30 mins. The heating rate was set as 10℃/min and the nitrogen gas flow rate was 3L/min. After the pyrolyzed lignin was collected, physical activation was first carried out in furnace with humidity control under 800 ℃ for 0.5 hr. After that, the samples were exposed to CO_2 flow at 800 ℃ for 0.5 hr. The produced ACs were placed in high concentration nitric acid (8 M HNO_3) and stirred at hot plate for 4-6 hrs. Produced samples were washed by DI water to obtain the neutralized carbons, which are named as H-ACs.

H-ACs in the amount of 0.1 g were mixed with 1 ml H_2O_2 and 2 ml DMF solvents. After fully stirring, the mixtures were transferred into the stainless-steel Teflon-lined autoclave. The heating process was carried at 110 ℃ for 1.5/2/3/4/8/16 hrs, the produced samples were named as H-AC-xh, where x is the time, e.g., H-AC-1.5h to H-AC-16h.

Separation and purification of CQDs

The produced CQDs were first separated via ultra-centrifugation at 20k g for 0.5 hr. To further purify the obtained CQDs, flash chromatography was conducted using the mixture of ethanol and milli Q water as eluent with varying volume ratio (from 10:1 to 1:10).

Results and discussions

In this section, we provide a description of the optical properties of the CQDs produced from this process. Our goal is to develop a predictive processing-structure-property-performance (PSPP) relationship for lignin-based carbon quantum dots. In this work, we tie the observed optical properties to the processing conditions. A thorough

characterization of the structure of the CQD remains to be determined. This structural characterization is important to decouple the distinct impacts of surface functionality and size on the optical properties.

Figure 6.1 shows the fluorescence mapping spectra of produced CQDs. For processing times from 1.5 h to 8 h, there is a monotonic relationship between processing time and the peak emission wavelength. The short processing times correspond to longer wavelengths, (640 nm (red light) at 1.5 h), which gradually changes to shorter wavelengths (415 nm (blue light) at 8 h). The exception to this rule is the 16 h processing time, which yields an intermediate yellow light at 513 nm. The PL emission spectra of samples are shown in Figure 6.2. With The emission peaks are located at 415 nm (H-AC-8h), 456 nm (H-AC-4h), 473 nm (H-AC-3h), 513 nm (H-AC-16h), 594 nm (H-AC-2h) and 640 nm (H-AC-1.5h), respectively.

Ignoring the 16 h exception, we observed that reaction duration plays an important role determining the optical property of synthesized CQDs. The longer processing time leads to a redshift of the emission spectra. As the larger CQDs are associated with longer wavelengths, we suggest that the CQDs emitting red light are larger than those emitting blue light. Thus, we conclude that the longer processing time up to 8 hours results in smaller size of CQDs. This is a sensible observation because the process of activation is one in which the starting material is decomposed by the activating agent. The behavior at 16 h to the contrary has yet to be explained.

Of particular interest, as shown in Figure 6.1 (e), the H-AC-8h CQDs displayed a narrow distribution of emission and excitation spectra, the single round shape in excitation-emission mapping spectra confirms the high purity of this sample. The corresponded PL spectra is shown in Figure 6.3. The emission peak of H-AC-8h centered at ~415 nm with a narrow FWHM ~ 71 nm, much smaller than the FWHM of conventional blue CQDs.[194-196] The deep blue emission achieved the lowest wavelength compared with the current

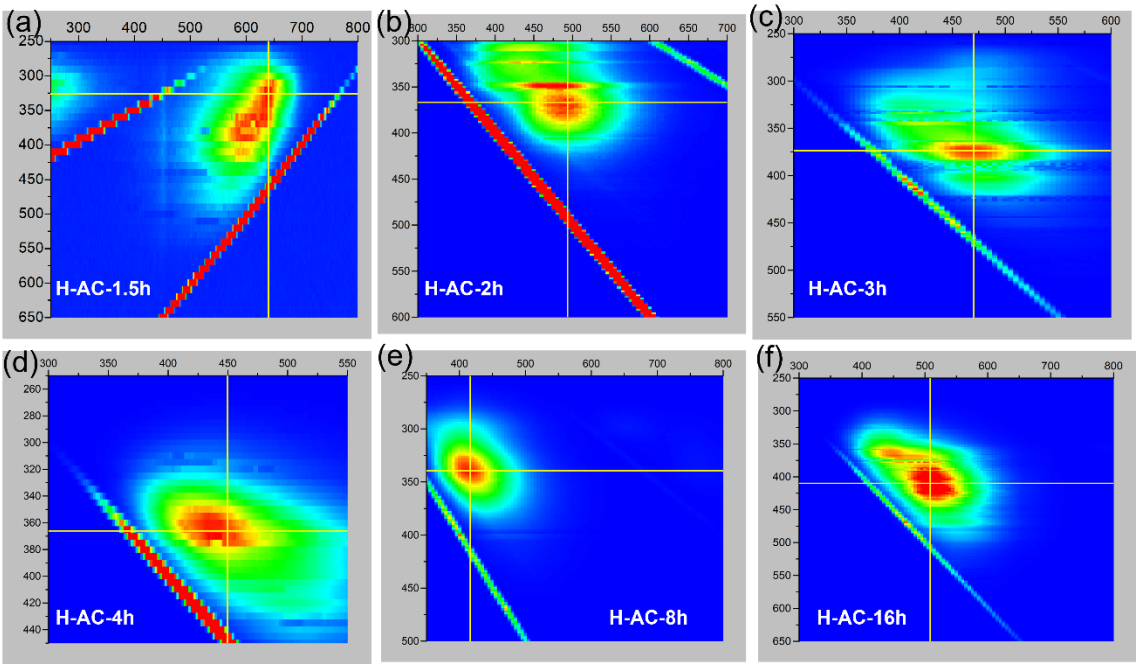

Figure 6.1 Fluorescence excitation-emission mapping spectra of (a) H-AC-1.5h, (b) H-AC-2h, (c) H-AC-3h, (d) H-AC-4h, (e) H-AC-8h, and (f) H-AC-16h CQDs.

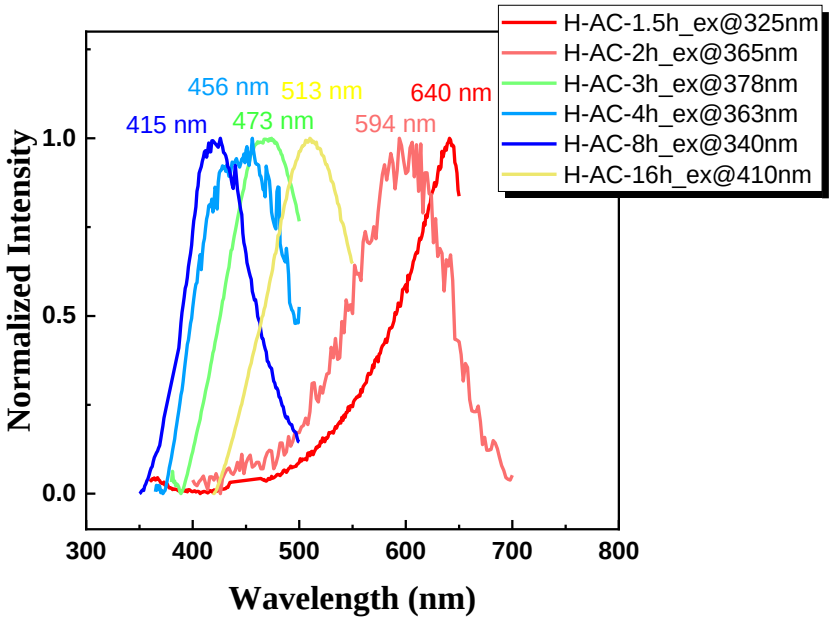

Figure 6.2 Excitation spectra of CD samples.

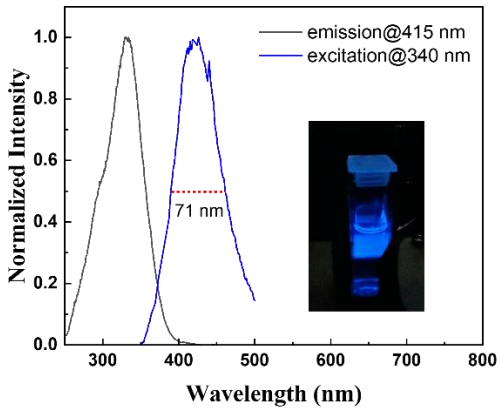

Figure 6.3 PL spectra of H-AC-8h with the photo image as the inserted picture.

publications of CQDs and it is even lower than that of conventional inorganic (perovskite and Cd^{2+}/Pb^{2+}-) quantum dots.[197] The H-AC-8h sample achieved excellent fluorescence performance, not only the deeper blue color, but also the narrow emission peak.

We also observe a change in the fluorescence spectra as a function of the concentration of the materials in solution. For example, the fluorescence spectra of H-AC-1.5h were shifted as the concentration of samples changed (shown in Figure 6.4). At low concentration, we observe a single emission peak at about 440 nm (excitation wavelength of ~320 nm) and, at medium concentration, a single emission peak at about 480 nm (excitation wavelength of 380 nm). At the high concentration, a broader peak emits at wavelengths from 600 to 640 nm (excitation wavelengths from 300 to 380 nm). We speculate that this phenomenon is due to the aggregation of CQDs. With increasing concentration, the attraction between CQD molecules and the interaction between CQD and water molecules promote the aggregation of CQDs leads to the increasing size of CD agglomerates, thus resulting in the red shift of fluorescence spectra.

While this work establishes a clear processing-property relationship and allows us to infer some structural information, an unambiguous structural characterization still needs to be performed. Current work involves conducting dynamic light scattering of all samples under different concentrations to determine the zeta potentials, particle sizes, particle charges, and the stability of the suspensions. TEM is also necessary to clarifying the structure, size distributions, and the presence of agglomerates of CQDs. FTIR and XPS will also be carried out to clarify the functionalities of produced CQDs and analyze the interactions between CQDs and solvent molecules.

Conclusions

In this work, we proposed a synthesis method that effectively produced lignin based CQDs with multi-color emissions from red to deep blue. Of special note, we produced deep blue color CQDs achieved emission peak centered at 415 nm and FWHM of 71 nm. The deep

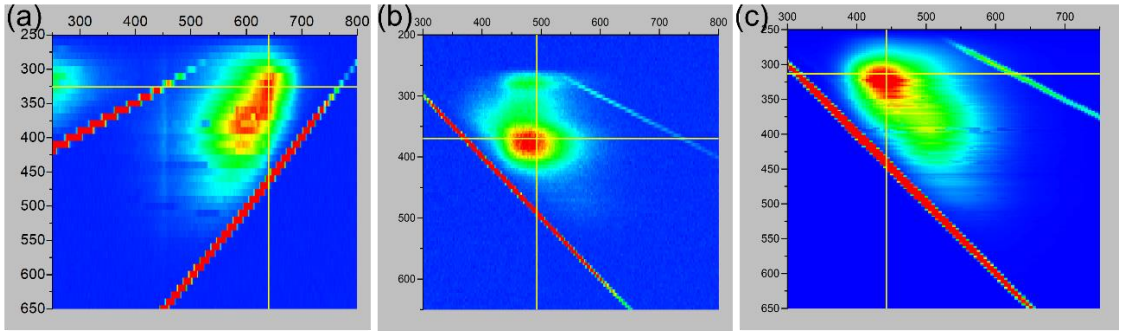

Figure 6.4 3D excitation-emission spectra of H-AC-1.5h at (a) high, (b) medium and (c) low concentration.

blue emission even comparable with that of conventional inorganic (perovskite and Cd^{2+}/Pb^{2+}-) quantum dots, thus expanded the applications of CQDs for the optoelectronic devices. We also observed a fluorescence spectra redshift introduced by the aggregation of CQD molecules under increased concentrations. This work establishes the processing and optical property components of the PSPP relationship. Structural characterization remains to be completed to determine morphology and size, molecular weight, surface charge, and chemical composition.

Chapter 7 Conclusion

Summary

Lignin has long been considered a low-value coproduct of pulp production. It presents a significant barrier to the extraction of plant sugars for conversion into biofuels and chemicals because of its recalcitrant nature and its high volume and low value. This dissertation presented methods to valorize lignin that herbaceous, hardwood, and softwood feedstocks that come from kraft and organosolv pulping. Thus, I explored a wide variety of lignin chemistries to determine the appropriate feedstock for the target material. From these investigations, I discovered enabling technologies that allowed an increase in lignin value and demonstrated the use of lignin as the basis for new sorbents, electrochemical devices, and functional nanomaterials. The new materials discussed in this dissertation can have lasting societal benefits for years to come. The following chapter summaries provide brief overviews of the materials, methods of synthesis, and significant results from each study.

Summary of Chapter Conclusions

Performance and economic analysis of organosolv aoftwood and herbaceous lignins to activated carbons as electrode materials in supercapacitors

This research employed two types of lignin (YP and SG) as the precursors for synthesizing porous activated carbon electrodes for supercapacitors. The pyrolysis and activation of lignin feedstocks result in porous activated carbons, with surface area and pore size distributions that can be tailored by feedstock choice and processing conditions. The structure of the ACs dictates adsorptive capacity and the diffusion rates of penetrating ions, which are reflected in the electrochemical performance of these materials as supercapacitors. 2D ^{1}H–^{13}C NMR were used to characterize the S/G/H alcohol units of lignin- based electrodes, which are important indices in evaluating biochar structures and pore characteristics of the activated carbons. The different O/C ratios, carbon aggregations, and inorganic impurities between the YP and SG chars were determined to be critical

factors inducing differing porosities and pore size distributions through a two-step activation process. Higher O/C ratios, less extent of carbon aggregations, and presence of inorganic impurities were easier to achieve for highly porous activated carbon structures. Based on the electrochemical performance of as-prepared electrodes, the specific capacitances of YP and SG capacitors reached 367 and 221 F g^{-1}, respectively. The YP capacitor displayed stable capacitance (the capacitance retention: > 90%) and excellent Coulombic efficiency (>99%) over 10,000 cycles. Analyzing the Randles plots, the apparent D value were determined to be 4.77×10^{-10} and 2.16×10^{-10} cm^2 s^{-1} for the YP and SG capacitors, respectively. This remarkable performance improvement of the YP carbon electrodes was likely the result of a shorter diffusion path and higher available active surface area for energy storage. Techno-economic analysis indicates that YP and SG capacitors can be produced at a minimum selling price of $8,493 and $6,670 per ton, respectively, which is competitive with the price of commercially produced supercapacitors. The novel lignin-based activated porous carbon electrodes developed in this work will pave the way for engineering inexpensive and high-performance electrode materials for various electrochemical energy devices.

Hierarchical lignin-based carbon matrix and carbon dot composite electrodes for high-performance supercapacitors

In this work, we achieved superior performance of SCs with the well-distributed CQDs decorating the surface of AC matrix. The introduction of hydrophilic CQDs not only improved the wettability of electrodes, but also created electroactive sites. The capacitance was greatly improved from 125.8 F g^{-1} to 301.7 F g^{-1} due to the enlarged effective surface area and enhanced electrochemical activity without sacrificing the high cyclability. With the existence of abundant polar sites, ions are attracted to and accumulate around the CQDs, therefore shortening ionic diffusion paths and decreasing the inner resistance. Our work indicates that the CQDs could be well dispersed on the carbon matrix and the effective surface area could be significantly improved *via* creating numberless functionalized CD sites, resulting in the enhanced electric double layer capacitance as well

as pseudo capacitance. The unique carbon composite can be utilized for engineering desired pore structure and micropore/mesopore fraction within the AC electrodes. This design of a decorated carbon framework possesses great potential for developing promising energy storage devices in the near future.

Tailored mesoporous structures of lignin-derived nano-carbons for multiple applications

This work investigated the effect of one- and two-step KOH activation on the surface properties of lignin-based activated carbons. One-step activation produced ACs achieved ultrahigh surface area as well as high mesopore ratio, leading to the ultrahigh energy density of the fabricated SCs as well as the ultrahigh MB adsorption capacity. The ionic diffusion resistance is greatly alleviated within the porous structure due to its high mesopore ratio. However, the relative hydrophobic surface limited its application for high power density SCs. In comparison, the two-step activation produced ACs has limited surface area but high oxygen contents, the oxygen not only existed on the surface but also doped inside porous structure, leading to the hydrophilic surface. The hydrophilicity of ACs greatly decreases the internal resistance and benefits the capacitance even at high current density, thus achieving high power density of the fabricated SCs. The dye adsorption capacities are also impressive due to the abundance of functional groups and higher ratio of carboxyl/carbonyl groups on the carbon surface. In summary, tailored pore structures of ACs with surface area from 50 to 3500 m^2 g^{-1} and mesopore ratio from 10 to 80% can be produced through controlling process conditions according to our methodology. The produced ACs have promising potentials to be applied for high performance supercapacitors as well as in environmental applications.

Lignin-derived magnetic activated carbons for effective cation dye removal

In this work, we developed a simple route to synthesize mACs in a one-step process. A mixture of lignin and ferric sulfate were applied as precursors for co-carbonization and activation. Incorporating ferric sulfate into the lignin matrix improved the surface area of mACs with magnetic iron oxides nanoparticles uniformly distributed on the surface. These

magnetite nanoparticles on ACs enhance the adsorption capacity and significantly improved the regeneration efficiency. The maximum adsorption capacity for MB was greatly increased from 55.0 mg g^{-1} on non-magnetic AC to 220.2 mg g^{-1} for the 5:1 mAC. The reusability test demonstrated that mACs could be easily separated magnetically and exhibited excellent reusability with high removal efficiency (> 98%) even after four use cycles. In conclusion, this work demonstrates that lignin-derived magnetic activated carbons are high performance adsorbents, synthesized from a lignin feedstock that is both economically and environmentally viable via a simple, single-step process.

Synthesis of lignin based CQDs with multicolor emissions

In this work, we proposed a synthesis method that effectively produced lignin based CQDs with multi-color emissions from red to deep blue. Of special note, we produced deep blue color CQDs achieved emission peak centered at 415 nm and FWHM of 71 nm. The deep blue emission even comparable with that of conventional inorganic (perovskite and Cd^{2+}/Pb^{2+}-) quantum dots, thus expanded the applications of CQDs for the optoelectronic devices. We also observed a fluorescence spectra redshift introduced by the aggregation of CQD molecules under increased concentrations. This work establishes the processing and optical property components of the PSPP relationship. Structural characterization remains to be completed to determine morphology and size, molecular weight, surface charge, and chemical composition.

Impact and Significance

The impacts of this work are significant for developing lignin-based high value carbon materials for various applications. In the face of the global climate/energy crisis, lignin, as a waste stream of the pulp and paper industry, has great potential as an abundant, inexpensive and renewable feedstock for developing high value carbon materials. In this work, we elucidated the processing-structure-property-performance (PSPP) relationship between various lignin precursors and produced activated carbons (ACs). We selected the softwood lignin as the best candidate for producing ACs via two-step physical activation. We also collaboratively conducted economic analysis for evaluating the feasibility of this

approach as well as the possibility of commercialization of lignin-derived ACs. To further improve the electrochemical performance of lignin-based ACs as electrodes in supercapacitors, carbon quantum dots (CQDs) were introduced into the electrode and significantly improved the electrochemical performance. For optimizing the porous structures and increasing the surface areas of lignin based ACs, traditional two-step chemical activation was conducted, and the updated one-step method was also proposed for producing ACs with much higher surface area and mesopore ratio. The corresponding electrochemical performance demonstrated improved capacitance and energy density compared with traditional, non-renewable materials.[198] As a whole, this work furthers the PSPP relationship, moving toward the goal of predictive processing of lignin for targeted product properties. Moreover, this work demonstrates practical potential of lignin-based electrodes in energy storage applications.

In addition to applying the lignin based ACs for supercapacitors, the ACs were also applied for environmental applications. The adsorption capacity of methylene blue dye of our chemical-activated carbons is excellent. To improve the adsorption capacity and regeneration efficiency of physical activated carbons, simple and facile method was proposed to synthesize lignin based magnetic ACs. As was the case with electrodes, we furthered the PSPP relationship and identified a simpler production path leading to the materials with properties competitive to existing adsorbents manufactured from non-renewable feedstocks.[199]

In addition to activated carbons, we also demonstrated that lignin could be used as precursor to develop carbon quantum dots (CQDs). The optimized synthesis method was proposed to produce lignin-derived CQDs with multiple color emissions from deep blue to red. Especially, the produced CQDs achieved deep blue color with narrow fluorescence spectra. The achieved deep blue emission is much lower than the that of CQDs in current publications, and it is comparable to conventional inorganic quantum dots.[197]

Based on the results of above work, the lignin can be used as precursor to produce high value carbon materials and apply for high performance energy storage devices, environmental applications as well as potential optical applications.

Taken together, this work has demonstrated that the time is now for an industrial shift to lignin-based carbon composites to replace materials manufactured from non-renewable feedstocks. The feedstock is abundant from domestic sources, inexpensive and renewable. No loss in performance is observed when comparing carbon materials manufactured from lignin relative to current materials from non-renewable sources. Activated carbons are a natural place to start and carbon quantum dots should not be far behind. Initial adoption should occur in energy storage devices and environmental remediation adsorbents.

Future Work

This work conducted physical activation as well as chemical activation to elucidate the process-structure-property-performance relationships between lignin and activated carbons and evaluated the electrochemical performance by applying the produced activated carbons as electrodes for supercapacitors. The results proved the potential of using lignin as precursor for developing high surface area ACs with tailored structure for electrochemical energy storage. Based on the results, it would be useful to investigate the effects of mesopore ratio on the electrochemical performance and continue optimizing the porous structures of lignin based ACs, produced via one-step chemical activation, for high performance supercapacitors.

The adsorption performance of lignin based ACs as adsorbent for cationic dye adsorption was verified. The one-step chemical activation produced ACs achieved excellent maximum adsorption capacity, and we also proposed efficient simple synthesis method for developing magnetic ACs with improved regeneration efficiency. Based on these results, an updated synthesis method combined with chemical activation to develop magnetic ACs with improved surface areas should be developed for improved adsorption performance as

well as recycling efficiency. Continued work should be conducted for using lignin-derived ACs as adsorbents for other organic contaminants adsorption and clarify the adsorption mechanism behind them.

Besides developing activated carbons for supercapacitors and water purification, lignin could also be used as precursor for producing nongraphitizable carbons as electrodes for batteries. Continued work should be done to elucidate the PSPP relationship between lignin and produced hard carbons. The produced carbons should be applied as electrodes for Na-ion batteries. As the mechanism behind Na-ion batteries is more akin to adsorption than intercalation, the lignin-derived hard carbons would be promising for applying as electrodes for Na-ion batteries.

Additionally, an effective synthesis method has been proposed for producing carbon quantum dots with multi-color emissions from lignin. The produced CQDs achieved deep blue emission, which is comparable with the conventional inorganic quantum dots. This is very promising for expanding the application of CQDs for LED devices. Continued work to fabricate the LED devices with the lignin based CQDs to test their optoelectronic performance would be useful.

References

1. Heitner, C.; Dimmel, D.; Schmidt, J., *Lignin and Lignans: Advances in Chemistry*. CRC Press: **2016**.
2. Bajwa, D. S.; Pourhashem, G.; Ullah, A. H.; Bajwa, S. G., A concise review of current lignin production, applications, products and their environmental impact. *Industrial Crops and Products* **2019,** *139*.
3. Suhas; Carrott, P. J.; Ribeiro Carrott, M. M., Lignin--from natural adsorbent to activated carbon: a review. *Bioresour Technol* **2007,** *98* (12), 2301-12.
4. Pandey, M. P.; Kim, C. S., Lignin Depolymerization and Conversion: A Review of Thermochemical Methods. *Chemical Engineering & Technology* **2011,** *34* (1), 29-41.
5. Gosselink, R. J. A.; de Jong, E.; Guran, B.; Abächerli, A., Co-ordination network for lignin—standardisation, production and applications adapted to market requirements (EUROLIGNIN). *Industrial Crops and Products* **2004,** *20* (2), 121-129.
6. Han, J.; Jeong, S.-Y.; Lee, J. H.; Choi, J. W.; Lee, J.-W.; Roh, K. C., Structural and Electrochemical Characteristics of Activated Carbon Derived from Lignin-Rich Residue. *ACS Sustainable Chemistry & Engineering* **2018,** *7* (2), 2471-2482.
7. Rowlandson, J. L.; Edler, K. J.; Tian, M.; Ting, V. P., Toward Process-Resilient Lignin-Derived Activated Carbons for Hydrogen Storage Applications. *ACS Sustainable Chemistry & Engineering* **2020,** *8* (5), 2186-2195.
8. Roberts, J. C., The chemistry of lignin and its removal. In *The Chemistry of Paper*, **1996**; pp 26-51.
9. Lignin chemistry-Past, present and future. *Wood Sci. Technol. 11*, 169-218.
10. Alonso David, M.; Hakim Sikander, H.; Zhou, S.; Won, W.; Hosseinaei, O.; Tao, J.; Garcia-Negron, V.; Motagamwala Ali, H.; Mellmer Max, A.; Huang, K.; Houtman Carl, J.; Labbé, N.; Harper David, P.; Maravelias Christos, T.; Runge, T.; Dumesic James, A., Increasing the revenue from lignocellulosic biomass: Maximizing feedstock utilization. *Science Advances* **2017,** *3* (5), e1603301.
11. Marsh, H.; Rodríguez-Reinoso, F., CHAPTER 1 - Introduction to the Scope of the Text. In *Activated Carbon*, Marsh, H.; Rodríguez-Reinoso, F., Eds. Elsevier Science Ltd: Oxford, **2006**; pp 1-12.
12. Marsh, H.; Rodríguez-Reinoso, F., CHAPTER 2 - Activated Carbon (Origins). In *Activated Carbon*, Marsh, H.; Rodríguez-Reinoso, F., Eds. Elsevier Science Ltd: Oxford, **2006**; pp 13-86.
13. Teng, H.; Ho, J.-A.; Hsu, Y.-F.; Hsieh, C.-T., Preparation of Activated Carbons from Bituminous Coals with CO2 Activation. 1. Effects of Oxygen Content in Raw Coals. *Industrial & Engineering Chemistry Research* **1996,** *35* (11), 4043-4049.
14. Meng, L.-Y.; Ma, M.-G.; Ji, X.-X., Preparation of Lignin-Based Carbon Materials and Its Application as a Sorbent. *Materials* **2019,** *12* (7), 1111.
15. Hsieh, C.-T.; Lin, Y.-T., Synthesis of mesoporous carbon composite and its electric double-layer formation behavior. *Microporous and Mesoporous Materials* **2006,** *93* (1-3), 232-239.
16. D. Qu, H. S., Studies of activated carbons used in double-layer capacitors. *Journal of Power Sources* **1998,** *74*, 99–107.

17. Chien-To Hsieh, H. T., Influence of Oxygen Treatment on Electric Double-Layer Capacitance of Activated Carbon Fabrics *Carbon* **2002,** *40*, 667–674.
18. Huang, J. B.; Patra, J.; Lin, M. H.; Ger, M. D.; Liu, Y. M.; Pu, N. W.; Hsieh, C. T.; Youh, M. J.; Dong, Q. F.; Chang, J. K., A Holey Graphene Additive for Boosting Performance of Electric Double-Layer Supercapacitors. *Polymers (Basel)* **2020,** *12* (4).
19. Yao, B.; Huang, H.; Liu, Y.; Kang, Z., Carbon Dots: A Small Conundrum. *Trends in Chemistry* **2019,** *1* (2), 235-246.
20. Yuan, F.; Li, S.; Fan, Z.; Meng, X.; Fan, L.; Yang, S., Shining carbon dots: Synthesis and biomedical and optoelectronic applications. *Nano Today* **2016,** *11* (5), 565-586.
21. Hu, C.; Li, M.; Qiu, J.; Sun, Y. P., Design and fabrication of carbon dots for energy conversion and storage. *Chemical Society Reviews* **2019,** *48* (8), 2315-2337.
22. Lim, S. Y.; Shen, W.; Gao, Z., Carbon quantum dots and their applications. *Chem Soc Rev* **2015,** *44* (1), 362-81.
23. Hola, K.; Zhang, Y.; Wang, Y.; Giannelis, E. P.; Zboril, R.; Rogach, A. L., Carbon dots—Emerging light emitters for bioimaging, cancer therapy and optoelectronics. *Nano Today* **2014,** *9* (5), 590-603.
24. Yuan, F.; Yuan, T.; Sui, L.; Wang, Z.; Xi, Z.; Li, Y.; Li, X.; Fan, L.; Tan, Z.; Chen, A.; Jin, M.; Yang, S., Engineering triangular carbon quantum dots with unprecedented narrow bandwidth emission for multicolored LEDs. *Nat Commun* **2018,** *9* (1), 2249.
25. Ding, H.; Yu, S. B.; Wei, J. S.; Xiong, H. M., Full-Color Light-Emitting Carbon Dots with a Surface-State-Controlled Luminescence Mechanism. *ACS Nano* **2016,** *10* (1), 484-91.
26. Wu, M.; Zhan, J.; Geng, B.; He, P.; Wu, K.; Wang, L.; Xu, G.; Li, Z.; Yin, L.; Pan, D., Scalable synthesis of organic-soluble carbon quantum dots: superior optical properties in solvents, solids, and LEDs. *Nanoscale* **2017,** *9* (35), 13195-13202.
27. Fabrication of Boron-Doped Diamond Nanorod Forest Electrodes and Their Application in Nonenzymatic Amperometric Glucose Biosensing.
28. Liu, H.; He, Z.; Jiang, L. P.; Zhu, J. J., Microwave-assisted synthesis of wavelength-tunable photoluminescent carbon nanodots and their potential applications. *ACS Appl Mater Interfaces* **2015,** *7* (8), 4913-20.
29. Zhu, S.; Song, Y.; Zhao, X.; Shao, J.; Zhang, J.; Yang, B., The photoluminescence mechanism in carbon dots (graphene quantum dots, carbon nanodots, and polymer dots): current state and future perspective. *Nano Research* **2015,** *8* (2), 355-381.
30. Liu, J.; Li, D.; Zhang, K.; Yang, M.; Sun, H.; Yang, B., One-Step Hydrothermal Synthesis of Nitrogen-Doped Conjugated Carbonized Polymer Dots with 31% Efficient Red Emission for In Vivo Imaging. *Small* **2018,** *14* (15), e1703919.
31. Azadi, P.; Inderwildi, O. R.; Farnood, R.; King, D. A., Liquid fuels, hydrogen and chemicals from lignin: A critical review. *Renewable and Sustainable Energy Reviews* **2013,** *21*, 506-523.
32. Rodríguez Correa, C.; Stollovsky, M.; Hehr, T.; Rauscher, Y.; Rolli, B.; Kruse, A., Influence of the Carbonization Process on Activated Carbon Properties from Lignin

and Lignin-Rich Biomasses. *ACS Sustainable Chemistry & Engineering* **2017,** *5* (9), 8222-8233.
33. Liu, W.-J.; Jiang, H.; Yu, H.-Q., Thermochemical conversion of lignin to functional materials: a review and future directions. *Green Chemistry* **2015,** *17* (11), 4888-4907.
34. Teng, H.; Hsieh, C.-T., Influence of Surface Characteristics on Liquid-Phase Adsorption of Phenol by Activated Carbons Prepared from Bituminous Coal. *Industrial & Engineering Chemistry Research* **1998,** *37* (9), 3618-3624.
35. Valente Nabais, J. M.; Teixeira, J. G.; Almeida, I., Development of easy made low cost bindless monolithic electrodes from biomass with controlled properties to be used as electrochemical capacitors. *Bioresource Technology* **2011,** *102* (3), 2781-2787.
36. Surya, K.; Michael, M. S., Novel interconnected hierarchical porous carbon electrodes derived from bio-waste of corn husk for supercapacitor applications. *Journal of Electroanalytical Chemistry* **2020,** *878*, 114674.
37. Cao, W.; Yang, F., Supercapacitors from high fructose corn syrup-derived activated carbons. *Materials Today Energy* **2018,** *9*, 406-415.
38. He, X.; Ling, P.; Qiu, J.; Yu, M.; Zhang, X.; Yu, C.; Zheng, M., Efficient preparation of biomass-based mesoporous carbons for supercapacitors with both high energy density and high power density. *Journal of Power Sources* **2013,** *240*, 109-113.
39. Guo, N.; Li, M.; Sun, X.; Wang, F.; Yang, R., Enzymatic hydrolysis lignin derived hierarchical porous carbon for supercapacitors in ionic liquids with high power and energy densities. *Green Chemistry* **2017,** *19* (11), 2595-2602.
40. Yu, L.; Hsieh, C.-T.; Keffer, D. J.; Chen, H.; Goenaga, G. A.; Dai, S.; Zawodzinski, T. A.; Harper, D. P., Hierarchical Lignin-Based Carbon Matrix and Carbon Dot Composite Electrodes for High-Performance Supercapacitors. *ACS Omega* **2021,** *6* (11), 7851-7861.
41. Sarkar, S.; Arya, A.; Gaur, U. K.; Gaur, A., Investigations on porous carbon derived from sugarcane bagasse as an electrode material for supercapacitors. *Biomass and Bioenergy* **2020,** *142*, 105730.
42. Souto, F.; Calado, V.; Pereira, N., Lignin-based carbon fiber: a current overview. *Materials Research Express* **2018,** *5* (7).
43. McKendry, P., Energy production from biomass (part 2)- conversion technologies. copy. *Bioresource Technology* **2002,** *83*, 47–54.
44. Calvo-Flores, F. G.; Dobado, J. A., Lignin as renewable raw material. *ChemSusChem* **2010,** *3* (11), 1227-35.
45. Kubo, S.; Kadla, J. F., Hydrogen Bonding in Lignin: A Fourier Transform Infrared Model Compound Study. *Biomacromolecules* **2005,** *6* (5), 2815-2821.
46. Chien-To Hsieh, H. T., Influence of mesopore volume and adsorbate size on adsorption capacities of activated carbons in aqueous solutions. *carbon* **2000,** *38*, 863–869.
47. Osaka, X. L. a. T., Properties of Electric Double‐Layer Capacitors with Various Polymer Gel Electrolytes. *J. Electrochem. Soc.* **1997,** *144*, 3077-3071.
48. Deyang Qu, H. S., Studies of activated carbons used in double-layer capacitors. *Journal of Power Sources* **1998,** *74*, 99-107.

49. Guerra, A.; Lucia, L. A.; Argyropoulos, D. S., Isolation and characterization of lignins from Eucalyptus grandis Hill ex Maiden and Eucalyptus globulus Labill. by enzymatic mild acidolysis (EMAL). *Holzforschung* **2008,** *62* (1), 24-30.
50. Das, L.; Li, M.; Stevens, J.; Li, W.; Pu, Y.; Ragauskas, A. J.; Shi, J., Characterization and catalytic transfer hydrogenolysis of deep eutectic solvent extracted sorghum lignin to phenolic compounds. *ACS Sustainable Chem Eng* **2018,** *6* (8), 10408-10420.
51. Kilpelaeinen, I.; Sipilae, J.; Brunow, G.; Lundquist, K.; Ede, R. M., Application of Two-Dimensional NMR Spectroscopy to Wood Lignin Structure Determination and Identification of Some Minor Structural Units of Hard- and Softwood Lignins. *Journal of Agricultural and Food Chemistry* **1994,** *42* (12), 2790-2794.
52. Hosseinaei, O.; Harper, D. P.; Bozell, J. J.; Rials, T. G., Improving Processing and Performance of Pure Lignin Carbon Fibers through Hardwood and Herbaceous Lignin Blends. *Int J Mol Sci* **2017,** *18* (7).
53. Hosseinaei, O.; Harper, D. P.; Bozell, J. J.; Rials, T. G., Role of Physicochemical Structure of Organosolv Hardwood and Herbaceous Lignins on Carbon Fiber Performance. *ACS Sustainable Chemistry & Engineering* **2016,** *4* (10), 5785-5798.
54. Yoshida, T.; Oshima, Y.; Matsumura, Y., Gasification of biomass model compounds and real biomass in supercritical water. *Biomass and Bioenergy* **2004,** *26* (1), 71-78.
55. Phillip F. Britt, A. C. B., III, Kimberly B. Thomas, Suk-Kyu Lee, Pyrolysis mechanisms of lignin- surface-immobilized model compound investigation of acid-catalyzed and free-radical reaction pathways. *Journal of Analytical and Applied Pyrolysis* **1995,** *33*, 1-9.
56. Kinoshita, K., *Carbon: Electrochemical and Physicochemical Properties*. Wiley: **1988**.
57. Rodriguez-Mirasol, J.; Cordero, T.; Rodriguez, J. J., Activated carbons from carbon dioxide partial gasification of eucalyptus kraft lignin. *Energy & Fuels* **1993,** *7* (1), 133-138.
58. Tang, L.; Ji, R.; Cao, X.; Lin, J.; Jiang, H.; Li, X.; Teng, K. S.; Luk, C. M.; Zeng, S.; Hao, J.; Lau, S. P., Deep Ultraviolet Photoluminescence of Water-Soluble Self-Passivated Graphene Quantum Dots. *ACS Nano* **2012,** *6* (6), 5102-5110.
59. Yang, Z.; Yao, Z.; Li, G.; Fang, G.; Nie, H.; Liu, Z.; Zhou, X.; Chen, X. A.; Huang, S., Sulfur-Doped Graphene as an Efficient Metal-free Cathode Catalyst for Oxygen Reduction. *ACS Nano* **2012,** *6* (1), 205-211.
60. Vinayan, B. P.; Zhao-Karger, Z.; Diemant, T.; Chakravadhanula, V. S. K.; Schwarzburger, N. I.; Cambaz, M. A.; Behm, R. J.; Kübel, C.; Fichtner, M., Performance study of magnesium–sulfur battery using a graphene based sulfur composite cathode electrode and a non-nucleophilic Mg electrolyte. *Nanoscale* **2016,** *8* (6), 3296-3306.
61. Russo, P.; Hu, A.; Compagnini, G.; Duley, W. W.; Zhou, N. Y., Femtosecond laser ablation of highly oriented pyrolytic graphite: a green route for large-scale production of porous graphene and graphene quantum dots. *Nanoscale* **2014,** *6* (4), 2381-9.

62. Periasamy, A.; Muruganand, S.; Palaniswamy, M., Vibrational studies of Na2SO4,K2SO4, NaHSO4 and KHSO4 crystals. *Rasāyan J. Chem.* **2009,** *2*, 981-986.
63. Kharangarh, P. R.; Umapathy, S.; Singh, G., Thermal Effect of Sulfur Doping for Luminescent Graphene Quantum Dots. *ECS Journal of Solid State Science and Technology* **2018,** *7* (3), M29-M34.
64. Zheng, J. P. H., J.; Jow, T. R., The Limitations of Energy Density for Electrochemical Capacitors. *J. Electrochem. Soc.* **1997,** *144*, , 2026-2031.
65. Hsieh C.-T., T. H., Influence of Oxygen Treatment on Electric Double-Layer Capacitance of Activated Carbon Fabrics. *Carbon* **2001,** *40*, 667-674.
66. Conway, B. E., *Electrochemical Supercapacitors: Scientific Fundamentals and Technological Applications*. Springer US: **2013**.
67. Hsieh, C.-T.; Chen, W.-Y.; Cheng, Y.-S., Influence of oxidation level on capacitance of electrochemical capacitors fabricated with carbon nanotube/carbon paper composites. *Electrochimica Acta* **2010,** *55* (19), 5294-5300.
68. R.L. McCreery, K. K. C., C.A. McDermott, M.T. McDermott, Control of reactivity at carbon eletrode surfaces. *Colloids Surf. A* **1994,** *93*.
69. Zeitsch, K. J., *The Chemistry and Technology of Furfural and its Many By-Products* 1st ed.; 9th February **2000**; Vol. 13.
70. Alonso, D. M.; Hakim, S. H.; Zhou, S.; Won, W.; Hosseinaei, O.; Tao, J.; Garcia-Negron, V.; Motagamwala, A. H.; Mellmer, M. A.; Huang, K.; Houtman, C. J.; Labbé, N.; Harper, D. P.; Maravelias, C.; Runge, T.; Dumesic, J. A., Increasing the revenue from lignocellulosic biomass: Maximizing feedstock utilization. *Science Advances* **2017,** *3* (5), e1603301.
71. The international cellulose market. https://www.paperindustryworld.com/the-international-cellulose-market/.
72. CCM: Furfural: export price falls to record low in May 2016. http://www.cnchemicals.com/Press/87387-CCM:%20Furfural:%20export%20price%20falls%20to%20record%20low%20in%20May%202016.html.
73. Hamelinck, C. N.; Faaij, A. P. C., Future prospects for production of methanol and hydrogen from biomass. *Journal of Power Sources* **2002,** *111* (1), 1-22.
74. Swanson, R. M.; Platon, A.; Satrio, J. A.; Brown, R. C.; Hsu, D. D. *Techno-Economic Analysis of Biofuels Production Based on Gasification*; Office of Scientific and Technical Information (OSTI): **2010**.
75. Seider, W. D., *Product and process design principles : synthesis, analysis, and evaluation*. Second edition. New York : Wiley, [2004] ©2004: **2004**.
76. Gonzalez, R.; Daystar, J.; Jett, M.; Treasure, T.; Jameel, H.; Venditti, R.; Phillips, R., Economics of cellulosic ethanol production in a thermochemical pathway for softwood, hardwood, corn stover and switchgrass. *Fuel Processing Technology* **2012,** *94* (1), 113-122.
77. Davis, R. E.; Grundl, N. J.; Tao, L.; Biddy, M. J.; Tan, E. C.; Beckham, G. T.; Humbird, D.; Thompson, D. N.; Roni, M. S. *Process Design and Economics for the Conversion of Lignocellulosic Biomass to Hydrocarbon Fuels and Coproducts: 2018*

Biochemical Design Case Update; Biochemical Deconstruction and Conversion of Biomass to Fuels and Products via Integrated Biorefinery Path; Office of Scientific and Technical Information (OSTI): **2018**.
78. Alonso David, M.; Hakim Sikander, H.; Zhou, S.; Won, W.; Hosseinaei, O.; Tao, J.; Garcia-Negron, V.; Motagamwala Ali, H.; Mellmer Max, A.; Huang, K.; Houtman Carl, J.; Labbé, N.; Harper David, P.; Maravelias Christos, T.; Runge, T.; Dumesic James, A., Increasing the revenue from lignocellulosic biomass: Maximizing feedstock utilization. *Science Advances 3* (5), e1603301.
79. Jouny, M.; Luc, W.; Jiao, F., General Techno-Economic Analysis of CO2 Electrolysis Systems. *Industrial & Engineering Chemistry Research* **2018,** *57* (6), 2165-2177.
80. Biddy, M. J.; Davis, R.; Humbird, D.; Tao, L.; Dowe, N.; Guarnieri, M. T.; Linger, J. G.; Karp, E. M.; Salvachúa, D.; Vardon, D. R.; Beckham, G. T., The Techno-Economic Basis for Coproduct Manufacturing To Enable Hydrocarbon Fuel Production from Lignocellulosic Biomass. *ACS Sustainable Chemistry & Engineering* **2016,** *4* (6), 3196-3211.
81. Weinstein, L.; Dash, R., Supercapacitor carbons. *Materials Today* **2013,** *16* (10), 356-357.
82. Zhu, Y.; Murali, S.; Stoller, M. D.; Ganesh, K. J.; Cai, W.; Ferreira, P. J.; Pirkle, A.; Wallace, R. M.; Cychosz, K. A.; Thommes, M.; Su, D.; Stach, E. A.; Ruoff, R. S., Carbon-based supercapacitors produced by activation of graphene. *Science* **2011,** *332* (6037), 1537-41.
83. Vlad, A.; Balducci, A., Supercapacitors: Porous materials get energized. *Nature Materials* **2017,** *16* (2), 161-162.
84. Forse, A. C.; Merlet, C.; Griffin, J. M.; Grey, C. P., New Perspectives on the Charging Mechanisms of Supercapacitors. *Journal of the American Chemical Society* **2016,** *138* (18), 5731-44.
85. Guan, B. Y.; Yu, L.; Wang, X.; Song, S.; Lou, X. W., Formation of Onion-Like NiCo2 S4 Particles via Sequential Ion-Exchange for Hybrid Supercapacitors. *Advanced Materials* **2017,** *29* (6).
86. Qing, Y.; Jiang, Y.; Lin, H.; Wang, L.; Liu, A.; Cao, Y.; Sheng, R.; Guo, Y.; Fan, C.; Zhang, S.; Jia, D.; Fan, Z., Boosting the supercapacitor performance of activated carbon by constructing overall conductive networks using graphene quantum dots. *Journal of Materials Chemistry A* **2019,** *7* (11), 6021-6027.
87. Wang, G.; Zhang, L.; Zhang, J., A review of electrode materials for electrochemical supercapacitors. *Chemical Society Reviews* **2012,** *41* (2), 797-828.
88. Najib, S.; Erdem, E., Current progress achieved in novel materials for supercapacitor electrodes: mini review. *Nanoscale Advances* **2019,** *1* (8), 2817-2827.
89. Salanne, M.; Rotenberg, B.; Naoi, K.; Kaneko, K.; Taberna, P. L.; Grey, C. P.; Dunn, B.; Simon, P., Efficient storage mechanisms for building better supercapacitors. *Nature Energy* **2016,** *1* (6).
90. Simon, P.; Gogotsi, Y., Materials for electrochemical capacitors. *Nature Materials* **2008,** *7* (11), 845-54.

91. Lyu, L.; Seong, K.-d.; Ko, D.; Choi, J.; Lee, C.; Hwang, T.; Cho, Y.; Jin, X.; Zhang, W.; Pang, H.; Piao, Y., Recent development of biomass-derived carbons and composites as electrode materials for supercapacitors. *Materials Chemistry Frontiers* **2019,** *3* (12), 2543-2570.
92. Beguin, F.; Presser, V.; Balducci, A.; Frackowiak, E., Carbons and electrolytes for advanced supercapacitors. *Advanced Materials* **2014,** *26* (14), 2219-51, 2283.
93. Denisa, H.-J.; Alexander, M. P.; Olga, I. P.; Fabian, S. r.-G. a.; Juan, M. D. T. n.; Gao, Q. L., Highly Stable Performance of Supercapacitors from Phosphorus-Enriched Carbons. *Journal of the American Chemical Society* **2009,** *131*, 5026–5027.
94. Pandolfo, A. G.; Hollenkamp, A. F., Carbon properties and their role in supercapacitors. *Journal of Power Sources* **2006,** *157* (1), 11-27.
95. Deng, Y.; Xie, Y.; Zou, K.; Ji, X., Review on recent advances in nitrogen-doped carbons: preparations and applications in supercapacitors. *Journal of Materials Chemistry A* **2016,** *4* (4), 1144-1173.
96. Chen, X.; Zhang, J.; Zhang, B.; Dong, S.; Guo, X.; Mu, X.; Fei, B., A novel hierarchical porous nitrogen-doped carbon derived from bamboo shoot for high performance supercapacitor. *Scientific Reports* **2017,** *7* (1), 7362.
97. Zhou, X.; Wang, P.; Zhang, Y.; Wang, L.; Zhang, L.; Zhang, L.; Xu, L.; Liu, L., Biomass based nitrogen-doped structure-tunable versatile porous carbon materials. *Journal of Materials Chemistry A* **2017,** *5* (25), 12958-12968.
98. Liu, M.; Niu, J.; Zhang, Z.; Dou, M.; Wang, F., Potassium compound-assistant synthesis of multi-heteroatom doped ultrathin porous carbon nanosheets for high performance supercapacitors. *Nano Energy* **2018,** *51*, 366-372.
99. Zhang, Y.; Liu, S.; Zheng, X.; Wang, X.; Xu, Y.; Tang, H.; Kang, F.; Yang, Q.-H.; Luo, J., Biomass Organs Control the Porosity of Their Pyrolyzed Carbon. *Advanced Functional Materials* **2017,** *27* (3).
100. Hsieh, C.-T.; Hsu, S.-M.; Lin, J.-Y.; Teng, H., Electrochemical Capacitors Based on Graphene Oxide Sheets Using Different Aqueous Electrolytes. *The Journal of Physical Chemistry C* **2011,** *115* (25), 12367-12374.
101. Fan, Z.; Yan, J.; Wei, T.; Zhi, L.; Ning, G.; Li, T.; Wei, F., Asymmetric Supercapacitors Based on Graphene/MnO2 and Activated Carbon Nanofiber Electrodes with High Power and Energy Density. *Advanced Functional Materials* **2011,** *21* (12), 2366-2375.
102. Wei, J. S.; Ding, H.; Zhang, P.; Song, Y. F.; Chen, J.; Wang, Y. G.; Xiong, H. M., Carbon Dots/NiCo2 O4 Nanocomposites with Various Morphologies for High Performance Supercapacitors. *Small* **2016,** *12* (43), 5927-5934.
103. García-Negrón, V.; Phillip, N. D.; Li, J.; Daniel, C.; Wood, D.; Keffer, D. J.; Rios, O.; Harper, D. P., Processing – Structure – Property Relationships for Lignin - Based Carbonaceous Materials Used in Energy - Storage Applications. *Energy Technology* **2017,** *5* (8), 1311-1321.
104. Fu, K.; Yue, Q.; Gao, B.; Sun, Y.; Zhu, L., Preparation, characterization and application of lignin-based activated carbon from black liquor lignin by steam activation. *Chemical Engineering Journal* **2013,** *228*, 1074-1082.

105. Gonzalez-Serrano, E.; Cordero, T.; Rodrı´guez-Mirasol, J.; Rodrı´guez, J. J., Development of Porosity upon Chemical Activation of Kraft Lignin with ZnCl2. *Industrial & Engineering Chemistry Research* **1997,** *36*, 4832-4838.
106. Maldhure, A. V.; Ekhe, J. D., Preparation and characterizations of microwave assisted activated carbons from industrial waste lignin for Cu(II) sorption. *Chemical Engineering Journal* **2011,** *168* (3), 1103-1111.
107. Hayashi, J. i.; Kazehaya, A.; Muroyama, K.; Watkinson, A. P., Preparation of activated carbon from lignin by chemical activation. *Carbon* **2000,** *38*, 1873–1878.
108. Gu, S.; Hsieh, C.-T.; Ashraf Gandomi, Y.; Chang, J.-K.; Li, J.; Li, J.; Zhang, H.; Guo, Q.; Lau, K. C.; Pandey, R., Microwave growth and tunable photoluminescence of nitrogen-doped graphene and carbon nitride quantum dots. *Journal of Materials Chemistry C* **2019,** *7* (18), 5468-5476.
109. Gu, S.; Hsieh, C. T.; Ashraf Gandomi, Y.; Li, J.; Yue, X. X.; Chang, J. K., Tailoring fluorescence emissions, quantum yields, and white light emitting from nitrogen-doped graphene and carbon nitride quantum dots. *Nanoscale* **2019,** *11* (35), 16553-16561.
110. Liu, W.-W.; Feng, Y.-Q.; Yan, X.-B.; Chen, J.-T.; Xue, Q.-J., Superior Micro-Supercapacitors Based on Graphene Quantum Dots. *Advanced Functional Materials* **2013,** *23* (33), 4111-4122.
111. Zhang, Z.; Zhang, J.; Chen, N.; Qu, L., Graphene quantum dots: an emerging material for energy-related applications and beyond. *Energy & Environmental Science* **2012,** *5* (10).
112. Yang, X.; Hu, D.; Zhang, P.; Ding, H.; Ji, Y.; Zou, H.; Li, B.; Wei, J.; Wei, X., Integrated Carbon Dots-Matrix Structures: An Efficient Strategy for High-Performance Electric Double Layer Capacitors. *ACS Applied Energy Materials* **2020,** *3* (5), 4958-4964.
113. Wei, J.-S.; Song, T.-B.; Zhang, P.; Zhu, Z.-Y.; Dong, X.-Y.; Niu, X.-Q.; Xiong, H.-M., Integrating Carbon Dots with Porous Hydrogels to Produce Full Carbon Electrodes for Electric Double-Layer Capacitors. *ACS Applied Energy Materials* **2020,** *3* (7), 6907-6914.
114. Hou, H.; Banks, C. E.; Jing, M.; Zhang, Y.; Ji, X., Carbon Quantum Dots and Their Derivative 3D Porous Carbon Frameworks for Sodium-Ion Batteries with Ultralong Cycle Life. *Adv Mater* **2015,** *27* (47), 7861-6.
115. Xiong, T.; Cen, W.; Zhang, Y.; Dong, F., Bridging the g-C3N4 Interlayers for Enhanced Photocatalysis. *ACS Catalysis* **2016,** *6* (4), 2462-2472.
116. Niu, S.; McFeron, R.; Godínez-Salomón, F.; Chapman, B. S.; Damin, C. A.; Tracy, J. B.; Augustyn, V.; Rhodes, C. P., Enhanced Electrochemical Lithium-Ion Charge Storage of Iron Oxide Nanosheets. *Chemistry of Materials* **2017,** *29* (18), 7794-7807.
117. Rafał Pelka, A. P.-J., and Walerian Arabczyk, Studies of the Oxidation of Nanocrystalline Iron with Oxygen by means of TG, MS, and XRD Methods. *The Journal of Physical Chemistry C* **2008,** *112*, 13992–13996.
118. Zhang, S.; Zhu, J.; Qing, Y.; Wang, L.; Zhao, J.; Li, J.; Tian, W.; Jia, D.; Fan, Z., Ultramicroporous Carbons Puzzled by Graphene Quantum Dots: Integrated High Gravimetric, Volumetric, and Areal Capacitances for Supercapacitors. *Advanced Functional Materials* **2018,** *28* (52).

119. Jian, X.; Li, J.-g.; Yang, H.-m.; Cao, L.-l.; Zhang, E.-h.; Liang, Z.-h., Carbon quantum dots reinforced polypyrrole nanowire via electrostatic self-assembly strategy for high-performance supercapacitors. *Carbon* **2017,** *114*, 533-543.
120. Hoang, V. C.; Nguyen, L. H.; Gomes, V. G., High efficiency supercapacitor derived from biomass based carbon dots and reduced graphene oxide composite. *Journal of Electroanalytical Chemistry* **2019,** *832*, 87-96.
121. Li, B.; Dai, F.; Xiao, Q.; Yang, L.; Shen, J.; Zhang, C.; Cai, M., Nitrogen-doped activated carbon for a high energy hybrid supercapacitor. *Energy & Environmental Science* **2016,** *9* (1), 102-106.
122. Hsieh, C.-T.; Teng, H., Influence of oxygen treatment on electric double-layer capacitance of activated carbon fabrics. *Carbon* **2002,** *40*, 667–674.
123. Zheng, J. P.; Huang, J.; Jow, T. R., The Limitations of Energy Density for Electrochemical Capacitors. *Journal of the Electrochemical Society* **1997,** *144* 2026-2031.
124. Lota, G.; Grzyb, B.; Machnikowska, H.; Machnikowski, J.; Frackowiak, E., Effect of nitrogen in carbon electrode on the supercapacitor performance. *Chemical Physics Letters* **2005,** *404* (1-3), 53-58.
125. Lota, G.; Lota, K.; Frackowiak, E., Nanotubes based composites rich in nitrogen for supercapacitor application. *Electrochemistry Communications* **2007,** *9* (7), 1828-1832.
126. Khattak, A. M.; Ghazi, Z. A.; Liang, B.; Khan, N. A.; Iqbal, A.; Li, L.; Tang, Z., A redox-active 2D covalent organic framework with pyridine moieties capable of faradaic energy storage. *Journal of Materials Chemistry A* **2016,** *4* (42), 16312-16317.
127. Zhou, L.; Cao, H.; Zhu, S.; Hou, L.; Yuan, C., Hierarchical micro-/mesoporous N- and O-enriched carbon derived from disposable cashmere: a competitive cost-effective material for high-performance electrochemical capacitors. *Green Chemistry* **2015,** *17* (4), 2373-2382.
128. Zhang, J.; Chen, Z.; Wang, G.; Hou, L.; Yuan, C., Eco-friendly and scalable synthesis of micro-/mesoporous carbon sub-microspheres as competitive electrodes for supercapacitors and sodium-ion batteries. *Applied Surface Science* **2020,** *533*, 147511.
129. Liang, H.; Lin, J.; Jia, H.; Chen, S.; Qi, J.; Cao, J.; Lin, T.; Fei, W.; Feng, J., Hierarchical NiCo-LDH/NiCoP@NiMn-LDH hybrid electrodes on carbon cloth for excellent supercapacitors. *Journal of Materials Chemistry A* **2018,** *6* (31), 15040-15046.
130. Shi, M. S.; Chen, Z.; Sun, J., Determination of chloride diffusivity in concrete by AC impedance spectroscopy. *Cement and Concrete Research* **1999,** *29*.
131. Alekhina, M.; Ershova, O.; Ebert, A.; Heikkinen, S.; Sixta, H., Softwood kraft lignin for value-added applications: Fractionation and structural characterization. *Industrial Crops and Products* **2015,** *66*, 220-228.
132. Sahoo, S.; Seydibeyoğlu, M. Ö.; Mohanty, A. K.; Misra, M., Characterization of industrial lignins for their utilization in future value added applications. *Biomass and Bioenergy* **2011,** *35* (10), 4230-4237.
133. Dehkhoda, A. M.; Gyenge, E.; Ellis, N., A novel method to tailor the porous structure of KOH-activated biochar and its application in capacitive deionization and energy storage. *Biomass and Bioenergy* **2016,** *87*, 107-121.

134. Oginni, O.; Singh, K.; Oporto, G.; Dawson-Andoh, B.; McDonald, L.; Sabolsky, E., Influence of one-step and two-step KOH activation on activated carbon characteristics. *Bioresource Technology Reports* **2019,** *7*.
135. Yin, J.; Zhang, W.; Alhebshi, N. A.; Salah, N.; Alshareef, H. N., Synthesis Strategies of Porous Carbon for Supercapacitor Applications. *Small Methods* **2020,** *4* (3).
136. Yu, L.; Seabright, K.; Bajaj, I.; Keffer, D. J.; Alonso, D. M.; Hsieh, C.-T.; Li, M.; Chen, H.; Dai, S.; Gandomi, Y. A.; Maravelias, C. T.; Harper, D. P., Performance and Economic Analysis of Organosolv Softwood and Herbaceous Lignins to Activated Carbons as Electrode Materials in Supercapacitors. *Frontiers in Energy Research* **2022,** *10*.
137. Lin, G.; Ma, R.; Zhou, Y.; Liu, Q.; Dong, X.; Wang, J., KOH activation of biomass-derived nitrogen-doped carbons for supercapacitor and electrocatalytic oxygen reduction. *Electrochimica Acta* **2018,** *261*, 49-57.
138. Lozano-Castelló, D.; Lillo-Ródenas, M. A.; Cazorla-Amorós, D.; Linares-Solano, A., Preparation of activated carbons from Spanish anthracite. *Carbon* **2001,** *39* (5), 741-749.
139. Hui, T. S.; Zaini, M. A. A., Potassium hydroxide activation of activated carbon: a commentary. *Carbon letters* **2015,** *16* (4), 275-280.
140. Islam, M. A.; Ahmed, M. J.; Khanday, W. A.; Asif, M.; Hameed, B. H., Mesoporous activated coconut shell-derived hydrochar prepared via hydrothermal carbonization-NaOH activation for methylene blue adsorption. *J Environ Manage* **2017,** *203* (Pt 1), 237-244.
141. Sayğılı, H.; Güzel, F., High surface area mesoporous activated carbon from tomato processing solid waste by zinc chloride activation: process optimization, characterization and dyes adsorption. *Journal of Cleaner Production* **2016,** *113*, 995-1004.
142. Prahas, D.; Kartika, Y.; Indraswati, N.; Ismadji, S., Activated carbon from jackfruit peel waste by H3PO4 chemical activation: Pore structure and surface chemistry characterization. *Chemical Engineering Journal* **2008,** *140* (1-3), 32-42.
143. Yin, H.; Lu, B.; Xu, Y.; Tang, D.; Mao, X.; Xiao, W.; Wang, D.; Alshawabkeh, A. N., Harvesting capacitive carbon by carbonization of waste biomass in molten salts. *Environ Sci Technol* **2014,** *48* (14), 8101-8.
144. Yu, L.; Hsieh, C. T.; Keffer, D. J.; Chen, H.; Goenaga, G. A.; Dai, S.; Zawodzinski, T. A.; Harper, D. P., Hierarchical Lignin-Based Carbon Matrix and Carbon Dot Composite Electrodes for High-Performance Supercapacitors. *ACS Omega* **2021,** *6* (11), 7851-7861.
145. Li, W.; Zhang, Y.; Das, L.; Wang, Y.; Li, M.; Wanninayake, N.; Pu, Y.; Kim, D. Y.; Cheng, Y.-T.; Ragauskas, A. J.; Shi, J., Linking lignin source with structural and electrochemical properties of lignin-derived carbon materials. *RSC Advances* **2018,** *8* (68), 38721-38732.
146. García-Negrón, V.; Chmely, S. C.; Ilavsky, J.; Keffer, D. J.; Harper, D. P., Development of Nanocrystalline Graphite from Lignin Sources. *ACS Sustainable Chemistry & Engineering* **2022,** *10* (5), 1786-1794.

147. Md Salim, R.; Asik, J.; Sarjadi, M. S., Chemical functional groups of extractives, cellulose and lignin extracted from native Leucaena leucocephala bark. *Wood Science and Technology* **2021,** *55* (2), 295-313.
148. Lopes, J. d. O.; Garcia, R. A.; Souza, N. D. d., Infrared spectroscopy of the surface of thermally-modified teak juvenile wood. *Maderas. Ciencia y tecnología* **2018,** (ahead), 0-0.
149. Robertson, A. C. F. a. J., Interpretation of Raman spectra of disordered and amorphous carbon. *PHYSICAL REVIEW B* **2000,** *61*.
150. C. Mapelli, C. C., and G. Zerbi, Common force field for graphite and polycyclic aromatic hydrocarbons. *PHYSICAL REVIEW B* **1999**.
151. Li, M.; Tsai, W.-Y.; Thapaliya, B. P.; Meyer, H. M.; Armstrong, B. L.; Luo, H.; Dai, S.; Nanda, J.; Belharouak, I., Modified coal char materials with high rate performance for battery applications. *Carbon* **2021,** *172*, 414-421.
152. Jin, L.; Gong, R.; Zhang, W.; Xiang, Y.; Zheng, J.; Xiang, Z.; Zhang, C.; Xia, Y.; Zheng, J. P., Toward high energy-density and long cycling-lifespan lithium ion capacitors: a 3D carbon modified low-potential Li2TiSiO5 anode coupled with a lignin-derived activated carbon cathode. *Journal of Materials Chemistry A* **2019,** *7* (14), 8234-8244.
153. Itoi, H.; Hasegawa, H.; Iwata, H.; Ohzawa, Y., Non-polymeric hybridization of a TEMPO derivative with activated carbon for high-energy-density aqueous electrochemical capacitor electrodes. *Sustainable Energy & Fuels* **2018,** *2* (3), 558-565.
154. Vinayagam, M.; Suresh Babu, R.; Sivasamy, A.; Ferreira de Barros, A. L., Biomass-derived porous activated carbon from Syzygium cumini fruit shells and Chrysopogon zizanioides roots for high-energy density symmetric supercapacitors. *Biomass and Bioenergy* **2020,** *143*.
155. Li, X.; Tang, Y.; Song, J.; Yang, W.; Wang, M.; Zhu, C.; Zhao, W.; Zheng, J.; Lin, Y., Self-supporting activated carbon/carbon nanotube/reduced graphene oxide flexible electrode for high performance supercapacitor. *Carbon* **2018,** *129*, 236-244.
156. Phiri, J.; Dou, J.; Vuorinen, T.; Gane, P. A. C.; Maloney, T. C., Highly Porous Willow Wood-Derived Activated Carbon for High-Performance Supercapacitor Electrodes. *ACS Omega* **2019,** *4* (19), 18108-18117.
157. Biswal, M.; Banerjee, A.; Deo, M.; Ogale, S., From dead leaves to high energy density supercapacitors. *Energy & Environmental Science* **2013,** *6* (4), 1249.
158. Hou, J.; Cao, C.; Ma, X.; Idrees, F.; Xu, B.; Hao, X.; Lin, W., From Rice Bran to High Energy Density Supercapacitors: A New Route to Control Porous Structure of 3D Carbon. *Scientific Reports* **2015,** *4* (1), 7260.
159. Xia, L.; Huang, H.; Fan, Z.; Hu, D.; Zhang, D.; Khan, A. S.; Usman, M.; Pan, L., Hierarchical macro-/meso-/microporous oxygen-doped carbon derived from sodium alginate: A cost-effective biomass material for binder-free supercapacitors. *Materials & Design* **2019,** *182*.
160. Han, X.; Jiang, H.; Zhou, Y.; Hong, W.; Zhou, Y.; Gao, P.; Ding, R.; Liu, E., A high performance nitrogen-doped porous activated carbon for supercapacitor derived from pueraria. *Journal of Alloys and Compounds* **2018,** *744*, 544-551.

161. Li, Y.; Du, Q.; Liu, T.; Peng, X.; Wang, J.; Sun, J.; Wang, Y.; Wu, S.; Wang, Z.; Xia, Y. J. C. E. R.; Design, Comparative study of methylene blue dye adsorption onto activated carbon, graphene oxide, and carbon nanotubes. **2013,** *91* (2), 361-368.
162. van Voorthuizen, E.; Zwijnenburg, A.; van der Meer, W.; Temmink, H., Biological black water treatment combined with membrane separation. *Water Res* **2008,** *42* (16), 4334-40.
163. Fazal, T.; Razzaq, A.; Javed, F.; Hafeez, A.; Rashid, N.; Amjad, U. S.; Ur Rehman, M. S.; Faisal, A.; Rehman, F., Integrating adsorption and photocatalysis: A cost effective strategy for textile wastewater treatment using hybrid biochar-TiO2 composite. *J Hazard Mater* **2020,** *390*, 121623.
164. Talukdar, K.; Jun, B. M.; Yoon, Y.; Kim, Y.; Fayyaz, A.; Park, C. M., Novel Z-scheme Ag3PO4/Fe3O4-activated biochar photocatalyst with enhanced visible-light catalytic performance toward degradation of bisphenol A. *J Hazard Mater* **2020,** *398*, 123025.
165. Ghoreishi, S. M.; Haghighi, R., Chemical catalytic reaction and biological oxidation for treatment of non-biodegradable textile effluent. *Chemical Engineering Journal* **2003,** *95* (1-3), 163-169.
166. Liang, L.; Zhang, S.; Goenaga, G. A.; Meng, X.; Zawodzinski, T. A.; Ragauskas, A. J., Chemically Cross-Linked Cellulose Nanocrystal Aerogels for Effective Removal of Cation Dye. *Front Chem* **2020,** *8*, 570.
167. Chang, J.; Ma, J.; Ma, Q.; Zhang, D.; Qiao, N.; Hu, M.; Ma, H., Adsorption of methylene blue onto Fe3O4/activated montmorillonite nanocomposite. *Applied Clay Science* **2016,** *119*, 132-140.
168. Liu, X.; Tian, J.; Li, Y.; Sun, N.; Mi, S.; Xie, Y.; Chen, Z., Enhanced dyes adsorption from wastewater via Fe3O4 nanoparticles functionalized activated carbon. *J Hazard Mater* **2019,** *373*, 397-407.
169. Feiqiang, G.; Xiaolei, L.; Xiaochen, J.; Xingmin, Z.; Chenglong, G.; Zhonghao, R., Characteristics and toxic dye adsorption of magnetic activated carbon prepared from biomass waste by modified one-step synthesis. *Colloids and Surfaces A: Physicochemical and Engineering Aspects* **2018,** *555*, 43-54.
170. Han, T.; Lu, X.; Sun, Y.; Jiang, J.; Yang, W.; Jonsson, P. G., Magnetic bio-activated carbon production from lignin via a streamlined process and its use in phosphate removal from aqueous solutions. *Sci Total Environ* **2020,** *708*, 135069.
171. Vikrant, K.; Kim, K. H.; Ok, Y. S.; Tsang, D. C. W.; Tsang, Y. F.; Giri, B. S.; Singh, R. S., Engineered/designer biochar for the removal of phosphate in water and wastewater. *Sci Total Environ* **2018,** *616-617*, 1242-1260.
172. Cazetta, A. L.; Pezoti, O.; Bedin, K. C.; Silva, T. L.; Paesano Junior, A.; Asefa, T.; Almeida, V. C., Magnetic Activated Carbon Derived from Biomass Waste by Concurrent Synthesis: Efficient Adsorbent for Toxic Dyes. *ACS Sustainable Chemistry & Engineering* **2016,** *4* (3), 1058-1068.
173. Wang, P.; Cao, M.; Wang, C.; Ao, Y.; Hou, J.; Qian, J., Kinetics and thermodynamics of adsorption of methylene blue by a magnetic graphene-carbon nanotube composite. *Applied Surface Science* **2014,** *290*, 116-124.

174. Yu, F.; Ma, J.; Wang, J.; Zhang, M.; Zheng, J., Magnetic iron oxide nanoparticles functionalized multi-walled carbon nanotubes for toluene, ethylbenzene and xylene removal from aqueous solution. *Chemosphere* **2016,** *146*, 162-72.
175. Nethaji, S.; Sivasamy, A.; Mandal, A. B., Preparation and characterization of corn cob activated carbon coated with nano-sized magnetite particles for the removal of Cr(VI). *Bioresour Technol* **2013,** *134*, 94-100.
176. Yang, Z.-F.; Li, L.-Y.; Hsieh, C.-T.; Juang, R.-S., Co-precipitation of magnetic Fe3O4 nanoparticles onto carbon nanotubes for removal of copper ions from aqueous solution. *Journal of the Taiwan Institute of Chemical Engineers* **2018,** *82*, 56-63.
177. Zhu, X.; Liu, Y.; Qian, F.; Zhou, C.; Zhang, S.; Chen, J., Preparation of magnetic porous carbon from waste hydrochar by simultaneous activation and magnetization for tetracycline removal. *Bioresour Technol* **2014,** *154*, 209-14.
178. Wu, R.; Liu, J.-H.; Zhao, L.; Zhang, X.; Xie, J.; Yu, B.; Ma, X.; Yang, S.-T.; Wang, H.; Liu, Y., Hydrothermal preparation of magnetic Fe3O4@C nanoparticles for dye adsorption. *Journal of Environmental Chemical Engineering* **2014,** *2* (2), 907-913.
179. Meng, X.; Scheidemantle, B.; Li, M.; Wang, Y. Y.; Zhao, X.; Toro-Gonzalez, M.; Singh, P.; Pu, Y.; Wyman, C. E.; Ozcan, S.; Cai, C. M.; Ragauskas, A. J., Synthesis, Characterization, and Utilization of a Lignin-Based Adsorbent for Effective Removal of Azo Dye from Aqueous Solution. *ACS Omega* **2020,** *5* (6), 2865-2877.
180. Yao, Y.; Gao, B.; Inyang, M.; Zimmerman, A. R.; Cao, X.; Pullammanappallil, P.; Yang, L., Removal of phosphate from aqueous solution by biochar derived from anaerobically digested sugar beet tailings. *J Hazard Mater* **2011,** *190* (1-3), 501-7.
181. Li, Y.; Zimmerman, A. R.; He, F.; Chen, J.; Han, L.; Chen, H.; Hu, X.; Gao, B., Solvent-free synthesis of magnetic biochar and activated carbon through ball-mill extrusion with Fe3O4 nanoparticles for enhancing adsorption of methylene blue. *Sci Total Environ* **2020,** *722*, 137972.
182. Fierro, V.; Torné-Fernández, V.; Montané, D.; Celzard, A., Adsorption of phenol onto activated carbons having different textural and surface properties. *Microporous and Mesoporous Materials* **2008,** *111* (1-3), 276-284.
183. García-Negrón, V.; Kizzire, D. G.; Rios, O.; Keffer, D. J.; Harper, D. P., Elucidating nano and meso-structures of lignin carbon composites: A comprehensive study of feedstock and temperature dependence. *Carbon* **2020,** *161*, 856-869.
184. Wang, X.; Cheng, H.; Ye, G.; Fan, J.; Yao, F.; Wang, Y.; Jiao, Y.; Zhu, W.; Huang, H.; Ye, D., Key factors and primary modification methods of activated carbon and their application in adsorption of carbon-based gases: A review. *Chemosphere* **2021,** *287* (Pt 2), 131995.
185. Wan, Z.; Li, K., Effect of pre-pyrolysis mode on simultaneous introduction of nitrogen/oxygen-containing functional groups into the structure of bagasse-based mesoporous carbon and its influence on Cu(II) adsorption. *Chemosphere* **2018,** *194*, 370-380.
186. Wang, G.; Li, G.; Huan, Y.; Hao, C.; Chen, W., Acrylic acid functionalized graphene oxide: High-efficient removal of cationic dyes from wastewater and exploration on adsorption mechanism. *Chemosphere* **2020,** *261*, 127736.

187. Si, M.; Zhang, J.; He, Y.; Yang, Z.; Yan, X.; Liu, M.; Zhuo, S.; Wang, S.; Min, X.; Gao, C.; Chai, L.; Shi, Y., Synchronous and rapid preparation of lignin nanoparticles and carbon quantum dots from natural lignocellulose. *Green Chemistry* **2018,** *20* (15), 3414-3419.
188. Meng, W.; Bai, X.; Wang, B.; Liu, Z.; Lu, S.; Yang, B., Biomass‐Derived Carbon Dots and Their Applications. *Energy & Environmental Materials* **2019,** *2* (3), 172-192.
189. Wang, J.; Wang, J.; Xiao, W.; Geng, Z.; Tan, D.; Wei, L.; Li, J.; Xue, L.; Wang, X.; Zhu, J., Lignin-derived red-emitting carbon dots for colorimetric and sensitive fluorometric detection of water in organic solvents. *Anal Methods* **2020,** *12* (25), 3218-3224.
190. Beyler, A. P.; Marshall, L. F.; Cui, J.; Brokmann, X.; Bawendi, M. G., Direct observation of rapid discrete spectral dynamics in single colloidal CdSe-CdS core-shell quantum dots. *Phys Rev Lett* **2013,** *111* (17), 177401.
191. Voznyy, O.; Mokkath, J. H.; Jain, A.; Sargent, E. H.; Schwingenschlögl, U., Computational Study of Magic-Size CdSe Clusters with Complementary Passivation by Carboxylic and Amine Ligands. *The Journal of Physical Chemistry C* **2016,** *120* (18), 10015-10019.
192. Hu, C.; Li, M.; Qiu, J.; Sun, Y. P., Design and fabrication of carbon dots for energy conversion and storage. *Chem Soc Rev* **2019,** *48* (8), 2315-2337.
193. Sk, M. A.; Ananthanarayanan, A.; Huang, L.; Lim, K. H.; Chen, P., Revealing the tunable photoluminescence properties of graphene quantum dots. *J. Mater. Chem. C* **2014,** *2* (34), 6954-6960.
194. Jiang, K.; Sun, S.; Zhang, L.; Lu, Y.; Wu, A.; Cai, C.; Lin, H., Red, green, and blue luminescence by carbon dots: full-color emission tuning and multicolor cellular imaging. *Angew Chem Int Ed Engl* **2015,** *54* (18), 5360-3.
195. Yuan, F.; Wang, Z.; Li, X.; Li, Y.; Tan, Z.; Fan, L.; Yang, S., Bright Multicolor Bandgap Fluorescent Carbon Quantum Dots for Electroluminescent Light-Emitting Diodes. *Adv Mater* **2017,** *29* (3).
196. Wang, L.; Wang, Y.; Xu, T.; Liao, H.; Yao, C.; Liu, Y.; Li, Z.; Chen, Z.; Pan, D.; Sun, L.; Wu, M., Gram-scale synthesis of single-crystalline graphene quantum dots with superior optical properties. *Nat Commun* **2014,** *5*, 5357.
197. Yuan, F.; Wang, Y.-K.; Sharma, G.; Dong, Y.; Zheng, X.; Li, P.; Johnston, A.; Bappi, G.; Fan, J. Z.; Kung, H.; Chen, B.; Saidaminov, M. I.; Singh, K.; Voznyy, O.; Bakr, O. M.; Lu, Z.-H.; Sargent, E. H., Bright high-colour-purity deep-blue carbon dot light-emitting diodes via efficient edge amination. *Nature Photonics* **2019,** *14* (3), 171-176.
198. Zhang, L. L.; Zhao, X. S., Carbon-based materials as supercapacitor electrodes. *Chem Soc Rev* **2009,** *38* (9), 2520-31.
199. Rafatullah, M.; Sulaiman, O.; Hashim, R.; Ahmad, A., Adsorption of methylene blue on low-cost adsorbents: a review. *J Hazard Mater* **2010,** *177* (1-3), 70-80.

VITA

Lu Yu was born in Shandong, China. She enrolled in North China Electric Power University where she obtained her bachelor's degree in thermal energy and power engineering in 2013. Lu received her Master of Science degree from North China Electric Power University, where she studied polymer solar cells with the research focused on solution–processed metal complexes as cathode interfacial layer and optimization of active layer with PVDF as nonvolatile additive. For her doctoral study, Lu Yu traveled to Tennessee and worked as the graduate research assistant in the Department of Materials Science and Engineering at the University of Tennessee, Knoxville. Her Ph.D. research focuses on biomass-derived carbon nanomaterials for electrochemical energy storage and carbon quantum dots. She also obtained an Interdisciplinary Graduate Minor in Computational Science during her time at Tennessee.